EXPERIMENTAL AND ANALYTICAL INVESTIGATIONS OF GRANULAR MATERIALS: SHEAR FLOW AND CONVECTIVE HEAT TRANSFER

Thesis by
Hojin Ahn

In Partial Fulfillment of the Requirements
for the Degree of
Doctor of Philosophy

California Institute of Technology
Pasadena, California

1989
(Submitted May 3, 1989)

ACKNOWLEDGEMENTS

I would like to thank my advisor, Professor C.E. Brennen, whose insight, patience, and encouragement were invaluable in the course of this work. Special thanks to Professor R.H. Sabersky who had been my advisor until his retirement.

I am grateful to Professor J.S. Patton of the Georgia Institute of Technology, my immediate predecessor on this research, who helped me during the first stage of this work. I also appreciate Professor M. Hunt who was always available when I needed to discuss. The assistance and friendship of Elmer Szombathy during my work in the machine shop and in the laboratory are still in my memory. I feel indebted to John Lee for his great help in developing experimental instruments. Thanks to Cecilia Lin for her help in preparing some figures. Thanks also to Billy Chi Fung Ip and Dana Pillsbury for their involvement in data collection.

I appreciate the years of financial support provided by the Shell Doctoral Graduate Fellowship. I also gratefully acknowledge the financial support granted by the National Science Foundation and Union Carbide Co. whose contributions were essential to the completion of this work.

I would also like to give thanks to the friends in my church who have been of great encouragement in sharpening my motivation for completing the Ph.D. degree. Finally, deepest thanks go to my family for their love and prayers during the years of my formal education. I dedicate this thesis with love to my parents who, through faith in Jesus Christ, have made me what I am.

ABSTRACT

Granular materials flowing down an inclined chute were studied experimentally and analytically. Characteristics of convective heat transfer to granular flows were also investigated experimentally and numerically.

Experiments on continuous, steady flows of granular materials in an inclined chute were conducted with the objectives of understanding the characteristics of chute flows and of acquiring information on the rheological behavior of granular material flow. Two neighboring fibre optic displacement probes were employed to measure mean velocity, one component of velocity fluctuations, and linear concentration at the wall and free surface boundaries. A shear gauge was also developed to make direct measurement of shear stress at the chute base. Measurements of solid fraction, velocity, shear rate, and velocity fluctuations were analyzed to understand the chute flow characteristics, and the rheological behavior of granular materials was studied with the present experimental data. The vertical profiles of mean velocity, velocity fluctuation, and solid fraction were also obtained at the sidewalls.

Existing constitutive equations and governing equations were used to solve for fully developed chute flows of granular materials, and thus the boundary value problem was formulated with two parameters (the coefficient of restitution between particles, and the chute inclination) and three boundary values at the chute base wall (the values of solid fraction, granular temperature, and mean velocity at the wall). The boundary value problem was numerically solved by the "shooting method." The boundary conditions at the free surface were satisfied by the proper choice of a gradient of granular temperature at the wall. The results show a significant role played by granular conduction in determining the profiles of granular temperature, solid fraction, and mean velocity in chute flows. These analytical results were also compared with the present experimental measurements and with the computer simulations by other investigators in the

literature.

Experiments on heat transfer to granular flows over a flat heating plate were conducted with three sizes of glass beads, polystyrene beads, and mustard seeds. A modification on the existing model for the convective heat transfer was made using the effective Nusselt number and the effective Peclet number, which include the effects of solid fraction variations. The slightly modified model could describe the heat transfer characteristics of both fast and slow flows (supercritical and subcritical flows).

A numerical analysis of the convective heat transfer to granular flows was also performed. The results were compared with the present experimental data, and reasonable agreement was found in the comparison.

TABLE OF CONTENTS

NOMENCLATURE

b	chute width
b	body force per unit mass
Ba	Bagnold number
c	specific heat capacity
c_p	specific heat capacity of the particle
d	particle diameter
e_p	coefficient of restitution between particles
e_w	coefficient of restitution between the wall and a particle
f	friction coefficient defined as τ_S/τ_N
$f_{ij}(\nu)$	tensor functions of the solid fraction
Fr	Froude number defined as $U/\sqrt{gh\cos\theta}$
g	gravitational acceleration
g_i	functions of ν and e_p, $(i = 1, 2, 3, 4, 5)$
g_o	radial distribution function
h	depth of flow
h	heat transfer coefficient
h_o	entrance gate height
h_{wp}	wall-particle heat transfer coefficient
h^{ν}_{wp}	wall-particle heat transfer coefficient at the solid fraction ν
k	thermal conductivity
k^*	nondimensional thermal conductivity, k/k_g
k_c	thermal conductivity at the critical solid fraction
k_e	effective thermal conductivity at the solid fraction ν
k_g	thermal conductivity of the interstitial gas
k_s	thermal conductivity of the solid phase
l	modified mean free path
L	length of the heating plate

L	length between two plates of the density gauge
$\dot{m}$	mass flow rate
M	mass of the material captured in the density gauge
Nu^*	modified Nusselt number defined as hd/k_g
$\mathrm{Nu}^*_{\mathrm{eff}}$	effective Nusselt number defined as $(hd/k_g)(k_c/k_e)$
$\mathbf{P}$	stress tensor
P_{xx}, P_{yy}	normal stresses
P_{xy}, P_{yx}	shear stresses
Pe^*	modified Peclet number defined as $(UL/\alpha_c)(d/L)^2(k_c/k_g)^2$
Pe^{**}	Peclet number defined as $(UL/\alpha_c)(d/L)^2(k_c/k_g)(1/\nu_c)$
$\mathrm{Pe}^*_{\mathrm{eff}}$	effective Peclet number defined as $(UL/\alpha_e)(d/L)^2(k_e/k_g)^2$
q	thermodynamic heat flux
$\mathbf{q}$	flux vector of fluctuation energy
q^*	nondimensional fluctuation energy flux, $q_y/\rho_p(gd\cos\theta)^{3/2}$
Q	rate of fluctuation energy added to the system per unit volume through granular conduction
Q^*	nondimensional granular conduction term, $Qd/\rho_p(gd\cos\theta)^{3/2}$
q_y	y-component of fluctuation energy flux
r	particle radius
s	characteristic particle spacing
s^*	nondimensional characteristic particle spacing, s/d
S	nondimensional parameter defined as $d(du/dy)/T^{1/2}$
t	time
T	granular temperature defined as $T = \frac{1}{3}(\langle u'^2\rangle + \langle v'^2\rangle + \langle w'^2\rangle)$
T^*	nondimensional granular temperature, $T/gd\cos\theta$
T^*_w	nondimensional granular temperature at the chute base wall
Δt	time interval
U	average mean velocity over the depth of flow
U	constant uniform velocity of the solid phase

u	mean velocity in the x-direction
$\mathbf{u}$	velocity vector
u^*	nondimensional velocity, $u/\sqrt{gd\cos\theta}$
u_m	average mean velocity over the depth of flow
u_s	mean velocity at the free surface
u_w	mean velocity at the chute base wall
u_w^*	nondimensional velocity at the chute base wall
u_1	single particle velocity in the x-direction before impact
u'	x-component of velocity fluctuations
u_w'	x-component of velocity fluctuations at the chute base wall
Δu	velocity difference, $u_s - u_w$
V	thermocouple voltage
v_1	single particle velocity in the y-direction before impact
v'	y-component of velocity fluctuations
W	rate of the work done to the system by stresses per unit volume
W^*	nondimensional work term, $Wd/\rho_p(gd\cos\theta)^{3/2}$
w'	z-component of velocity fluctuations
x	coordinate in the flow direction
x^*	nondimensional x-coordinate, x/L
y	coordinate in the direction normal to the chute base
y^*	nondimensional y-coordinate, y/d
z	coordinate in the direction lateral to the chute
α	thermal conductivity
α_c	thermal conductivity at the critical solid fraction
α_e	effective thermal conductivity at the solid fraction ν
α_1	impact angle defined as $\tan^{-1}(u_1/v_1)$
γ	dissipation rate of fluctuation energy per unit volume
γ^*	nondimensional dissipation term, $\gamma d/\rho_p(gd\cos\theta)^{3/2}$
δ	roughness of the surface

η	parameter defined as $(1 + e_p)/2$
θ	angle of chute inclination
Θ	thermodynamic temperature
Θ^*	nondimensional thermodynamic temperature, Θ/Θ_w
Θ_w	thermodynamic temperature at the heating surface
λ	parameter related to the solid fraction
μ	dynamic viscosity of the interstitial fluid
μ_c	Coulombic friction coefficient
ν	solid fraction
ν^*	maximum shearable solid fraction
ν_c	critical solid fraction
ν_m	mean solid fraction over the depth of flow
ν_w	wall solid fraction near the chute base wall
ν_{1D}	linear concentration
ν_{2D}	two-dimensional solid fraction
ν_{3D}	three-dimensional solid fraction
ρ	bulk density
ρ_p	particle density
τ	diffusion time
τ	time delay measured by two neighboring fibre optic probes
τ_{ij}	stress tensor
τ_N	normal stress
τ_S	shear stress
ϕ_A	surface coverage factor
χ	empirical constant related to the thermal conductance at the wall
ω	rotational rate of a particle
ω_1	rotational rate of a particle before impact

LIST OF FIGURES

CHAPTER 1
INTRODUCTION

A granular material is an assembly of discrete solid particles dispersed in a fluid or vacuum. The solid particles are in contact or near contact with other particles. Thus the granular material should be distinguished from other solid-fluid systems such as dilute suspensions. The role of the interstitial fluid in determining the dynamics of granular materials varies in its importance. Bagnold [1954] distinguished three different regimes of flow behavior, namely, macroviscous, transitional, and grain inertia regimes. Classification of a particular shear flow was made using the so-called "Bagnold number,"

$$\mathrm{Ba} = \lambda^{\frac{1}{2}} \rho_p d^2 \left(\frac{du}{dy}\right) / \mu,$$

where λ is a parameter related to the solid fraction, ρ_p the particle density, d the particle diameter, du/dy the shear rate, and μ the dynamic viscosity of the interstitial fluid. In the macroviscous regime, corresponding to small Bagnold number, the viscosity of an interstitial fluid plays a significant role in mechanics of momentum transport. On the other hand, the interstitial fluid in the grain inertia regime, corresponding to large Bagnold number, plays a minor role, and the behavior of a granular flow is governed largely by direct interactions between particles. In the present work, air was always the interstitial fluid, and particle diameters were larger than about 0.5 mm and the density of particles was much larger than that of air. Therefore, most granular flows fall into the grain inertia regime, and the interstitial fluid effect in the momentum transfer mechanism is considered negligible.

However, the interstitial fluid always plays a major role in the convective heat transfer mechanism. For example, Wunschmann and Schlünder [1980] made heat transfer measurements from heated surfaces to granular materials in various interstitial gas pressures. The results show that the heat transfer rate is much less under vacuum, indicating the importance of the interstitial fluid as the heat

transfer mechanism.

Information on the mechanics of granular materials is important in many technological and scientific contexts. For example, mineral and powder processing, transports of plastics and dry chemicals, handling of grain, coal, and shale, flows in pebble bed nuclear reactors, snow avalanches, and even dynamics of planetary rings demand a better understanding of flow characteristics and fundamental rheological behaviors of the materials. The understanding of the characteristics of convective heat transfer in granular materials is also important in process industry, chemical industry, and nuclear or solar energy industry. For example, many applications in chemical processing require precise temperature control, and heating or cooling of the granular products is often necessary before packaging and storage.

1.1 SHEAR FLOW OF GRANULAR MATERIALS

The rapid flow of granular materials is characterized by high deformation rates, and this rapid shearing motion of the flow causes collisions between particles, generating random motions of those particles. The random motions constitute a so-called granular temperature, which is a measure of the fluctuation energy in the granular material. Just like the normal thermodynamic temperature, granular temperature is conducted if there is any temperature gradient. That is, fluctuation energy flows from a region of high fluctuation energy to a region of low fluctuation energy by the process of granular conduction.

Though many studies on granular materials draw the analogy with the kinetic theory of gases, there are differences between granular materials and gas molecules. One of the major differences is that the collisions between granular particles are inelastic. This implies that energy dissipation due to inelastic collisions plays an important role in the mechanism of fluctuation energy balance. Therefore, the generation of fluctuation energy due to shear motions, its dissipation due to inelastic collisions, and granular conduction should balance in the

fluctuation energy equation of the system. When fluctuation energy generated by shear motion is greater than energy dissipation, the excessive energy is conducted out of the system. In the opposite case, the deficient energy is conducted into the system from the outside. One of the purposes of this thesis was to examine this balance of fluctuation energy in a granular flow.

Conventional fluid mechanics assumes no-slip conditions which determine the local velocity and temperature independently of the flow field. For granular flow, however, there is velocity slip at the boundary in general. Furthermore, the boundary of the system performs shear work on the flow, generating fluctuation energy. At the same time, collisions of particles with the wall boundary dissipate the energy. Therefore, the boundary of the system may serve as either a source or a sink of fluctuation energy, depending on which of generation and dissipation dominates (see Jenkins and Richman [1986]). These boundary conditions of granular flow can not be obtained independently of the flow field, and studies on the slip velocity and fluctuation energy flux at the boundary face many difficulties. Thus, in the present work, an emphasis was put on measurements of various flow properties at the wall boundary, such as slip velocity, velocity fluctuations at the wall, and local solid fraction near the wall. Furthermore, the effect of the surface condition on these boundary properties was investigated by making measurements with various surface conditions.

Our knowledge of the rheological behavior of rapidly flowing granular materials has been advanced by theoretical works. For example, Ogawa *et al.* [1980], Savage and Jeffrey [1981], Jenkins and Savage [1983], and Lun *et al.* [1984] have provided constitutive relations that lead to a comprehension of how stresses are associated with solid fraction, shear rate, and granular temperature, and how fluctuation energy flux is related to granular temperature, solid fraction, and their gradients. Savage and Jeffrey [1981] introduced the nondimensional parameter, S, which is the ratio of the characteristic mean shear velocity to the granular temperature, and stress components were expressed as integrals involv-

ing S. Jenkins and Savage [1983] extended the analysis of Savage and Jeffrey by including energy dissipation due to inelastic collisions. In addition to the collisional contribution to the stresses, Lun *et al.* [1984] included the kinetic contribution that was assumed to be negligible in Jenkins and Savage's analysis. It was found that at high solid fraction the collisional contribution dominates in the mechanism of momentum transport but the kinetic contribution is dominant at low solid fraction where collisions are infrequent and particles move long distances between collisions. (The review papers by Savage [1984] and Campbell [1989b] give thorough coverage of many theoretical works.)

For simple shear flow where uniform velocity gradient, temperature, and density are assumed (and therefore there is no granular conduction), all the theoretical analyses predict the same behavior as Bagnold [1954] described in connection with his experiments, namely,

$$\tau_{ij} = \rho_p f_{ij}(\nu) d^2 \left(\frac{du}{dy}\right)^2$$

where τ_{ij} is the stress tensor, ρ_p the particle density, f_{ij} a tensor function of the solid fraction ν, d the particle diameter, and du/dy the local mean shear rate. Lun *et al.* [1984] presented a solution for simple shear flow, and the parameter S was obtained as a function of solid fraction and the coefficient of restitution. In application to chute flows, however, the nonuniformity of velocity gradient, granular temperature, and solid fraction over the depth of flow complicates the solution of the equations for chute flows. Furthermore, theoretical works have faced difficulties due to lack of knowledge of appropriate boundary conditions both at solid walls and at the free surface.

In addition to particle interactions with the wall boundary, interactions between particles also remain to be explored for further understanding of the rheological behavior. The coefficient of restitution and the surface friction of particles may be represented as two major properties of particles. The effect of a variable coefficient of restitution that depends on the particle impact velocity has been studied by Lun and Savage [1986]. It has been found that the coefficient of

restitution, which increases with decreasing impact velocity, causes the stresses to vary with the shear rate raised to a power less than two. The effect of particle rotation and surface friction in collisions between particles have also been studied by Lun and Savage [1987], Jenkins and Richman [1985], and Nakagawa [1988]. When the surface friction was included in the theory, calculations became too complicated. Therefore, the inclusion of the surface friction was applied only to special cases of very limited value.

Computer simulations of simple shear flows or Couette flows (for example, Campbell and Brennen [1985a], Walton and Braun [1986a, b], Campbell and Gong [1986], and Campbell [1989]) have added considerably to our knowledge of the rheology of granular material flows. For example, anisotropy of the granular temperature as solid fraction decreases has been found in most computer simulations while many theoretical works assume the temperature to be isotropic. Relatively little work has been done on the computer simulation of gravity flows. Campbell and Brennen [1985b] simulated chute flows with two-dimensional disks, presenting the profiles of velocity, solid fraction, and granular temperature over the depth of flow. Walton *et al.* [1988] have used three-dimensional spheres to simulate gravity flow of particles through arrays of cylindrical horizontal rods and down inclined chutes. Both have employed periodic boundaries, which imply steady, fully developed flow. Complicated interactions between particles and between particles and walls require further investigation. The effect of a variable coefficient of restitution has also been examined in the computer simulation by Walton and Braun [1986b]. The results manifested a deviation from those of the constant coefficient of restitution in a manner similar to that of Lun and Savage [1986], but the calculated stresses were significantly lower than those of experimental studies and Lun and Savage.

On the other hand, progress in experimental methods for granular materials has been very limited, being hindered by obvious difficulties involved in making point measurements of velocity, solid fraction, and granular temperature in the

interior of granular flows. For example, the granular temperature, in spite of its importance, had not been experimentally measured until Ahn *et al.* [1988] used fibre optic displacement probes to measure one component of the granular temperature. The present state of the experimental information on granular flows consists of a number of Couette flow studies (e.g., Savage and McKeown [1983], Savage and Sayed [1984], Hanes and Inman [1985], Craig *et al.* [1986]) and several studies of flows down inclined chutes (e.g., Ridgway and Rupp [1970], Bailard [1978], Augenstein and Hogg [1978], Savage [1979], Sayed and Savage [1983], Patton *et al.* [1987], and Ahn *et al.* [1988, 1989a]). The understandable initial objective of some of the Couette flow experiments, such as those of Savage and McKeown, was to produce a simple shear flow with uniform velocity gradient, uniform solid fraction, and hopefully, uniform granular temperature. To this end the surfaces of the solid walls were roughened to create a no-slip condition at the wall. Practical engineering circumstances require the knowledge of how to model the conditions for smooth walls at which slip occurs. This presents some difficulties because the boundary conditions on the velocity and granular temperature at the smooth walls are far from clear (see, for example, Campbell [1988]).

Only recently has the numerical analysis of the flow of granular materials been attempted, partly because the constitutive relations have been unclear and partly because the boundary conditions still remain uncertain. Johnson and Jackson [1987] proposed constitutive relations in which frictional and collisional-translational mechanisms are combined for stress transmission. Furthermore, they developed boundary conditions at the wall, which relate friction force and slip velocity at the wall with the large-scale roughness of the surface, and relate the wall-particle coefficient of restitution and fluctuation energy flux at the wall. Both relations were described in terms of local density and granular temperature. Using these boundary conditions, Johnson and Jackson [1988] attempted to numerically solve the chute flow of granular materials. Clearly the limitations

involved in an analytical approach to granular material flows lie in the postulated constitutive relations and boundary conditions and in the assumption that a continuum approach has validity. Therefore, without thorough understanding of constitutive relations and boundary conditions, the analytical results will be of limited value. Furthermore, the continuum assumption implies that the analysis will be of dubious validity when the depth of flow becomes less than several particle diameters.

Chute flows differ from Couette flows and have a "conduction" of granular temperature as indicated in the computer simulation of Campbell and Brennen [1985b]. In their work, a boundary layer next to the wall had a lower solid fraction and higher granular temperature than the bulk further from the wall, indicating a conduction from the boundary layer to the bulk. However, experimental measurements through the sidewalls by Ahn *et al.* [1989a] show that the solid fraction monotonically decreases with distance from the wall, and that the granular temperature is conducted from the free surface to the chute base. The analysis of fully developed chute flow by Ahn *et al.* [1989b] shows that the granular temperature can be conducted either from the wall boundary to the free surface, or from the free surface to the wall, depending on the values of the coefficient of restitution and the angle of chute inclination. The results also show a significant role played by the granular conduction in determining the profiles of granular temperature, solid fraction, and velocity. Furthermore, the granular conduction term and the dissipation term are found to be comparable in magnitude.

In chapter 3 of the present work, experiments on continuous, steady flows of granular materials down an inclined chute have been presented. With the help of two neighboring fibre optic probes, the vertical profiles of mean velocity, velocity fluctuation, and linear concentration were obtained at the sidewalls. Measurements of some basic flow properties such as solid fraction, velocity, shear rate, and velocity fluctuation were analyzed to understand the characteristics of

the chute flow. Finally, the rheological behavior of granular materials was studied with the experimental data. In chapter 4, the analysis of fully developed chute flow has been conducted to understand the nature of granular conduction and its role in determining the profiles of granular temperature, solid fraction, and mean velocity. The governing and constitutive equations of Lun *et al.* [1984] have been employed, and the results have been compared with the present experimental data and other computer simulations.

1.2 HEAT TRANSFER TO GRANULAR FLOWS

Convective heat transfer to gas-solid flows occurs in many engineering disciplines. In fluidized beds, gas flow causes the fluidization of particles which have only local velocity fluctuations with zero mean velocity. In packed beds, when there is a pressure gradient across the bed, gas flows around stationary particles. On the other hand, in moving beds or granular flows in an inclined chute, particles are transported by gravity while the interstitial gas is considered stationary.

In these gas-solid flows, heat transfer between the wall boundaries and the flows is involved, and the heat transfer characteristics are affected by the wall surface condition, such as the roughness of the wall boundaries, and the shape of the particles. The solid fraction is an important property of the flow and it has a major influence on the heat transfer characteristics. Especially, the local solid fraction near wall boundaries plays an important role in determining heat transfer between the wall boundaries and the flows.

Although fluidized beds, packed beds, and granular flows are inherently different from one another, many similarities exist in heat transfer characteristics. For example, in gas fluidized beds, the heat transfer coefficient increases with the fluidizing gas velocity, reaches a maximum, and slightly decreases with the further increase of gas velocity. (See, for example, Gelperin and Einstein [1971].) When the surface in packed beds is vibrated (see Muchowski [1980]), heat transfer

is improved as the frequency increases slowly for a given amplitude. But for further increase, the heat transfer coefficient reaches a maximum, and then falls for larger frequencies of vibration. The same phenomenon is also observed in heat transfer to granular flows in an inclined chute (see Spelt *et al.* [1982] and Patton *et al.* [1986]). That is, for high solid fraction, the increase of granular velocity improves convective heat transfer. As the velocity increases further, heat transfer coefficient reaches a maximum, after which heat transfer decreases because of the decrease of solid fraction. In spite of these similarities among fluidized beds, packed beds, and moving beds, however, the transfer of knowledge from one type of flow to another is somewhat limited.

The heat transfer in gas-solid flows involves the following mechanisms:

1. Wall-to-particle heat transfer.
   i) Heat transfer through gaseous gap between the wall and particles.
   ii) Heat transfer through the contact points between the wall and particles.
   iii) Radiation between the wall and particles.
2. Heat conduction in the bulk of the flow.
3. Heat convection by particle motions.
4. Radiation between particles and gas.

Heat conduction in the bulk of the flow was examined by Bauer and Schlünder [1978a, b]. They developed a model for the thermal conductivity without gas flow, and the model was compared with numerous experimental data. They also obtained the effective thermal conductivity when there is gas flow, with the assumption that the effective thermal conductivity is the sum of a convective transport due to the flow and of conduction in discrete solid phases.

The analysis of heat convection by particle motions is more difficult mainly because the particle motions themselves are not well known. Campbell and Wang [1986] have obtained the effective conductivity of shearing particle flows in an annular Couette shear cell. It has been shown that the effective conductivity can be decomposed into two parts. One is a configurational component which is a

function of solid fraction, and the other is a dynamic component which appears to be linearly proportional to the shear rate.

Recently the analysis of heat conduction through direct contact points between two surfaces has received considerable attention. For example, the microelectronic industry has studied heat conduction through contact points to eliminate the heat generated from microchips (for example, see Eid and Antonetti [1986]). In gas-solid flows, it has been found that heat conduction through the contact point contributes little to the overall heat transfer process except for the case in which solid particles with high thermal conductivity such as metal particles are used in a high vacuum. (See Wunschmann and Schlünder [1980], and Sun and Chen [1986]). In experiments in a room temperature environment, radiation contribution can also be neglected in the analysis.

While an interstitial gas plays little role in momentum transfer, heat conduction through the interstitial gas in the gap between the wall and a particle is the most important heat transfer mechanism in gas-solid flows. In many heat transfer models developed in the last decade, the gaseous gap between the wall and a particle is represented as a thermal contact resistance. Schlünder [1980, 1984] proposed an expression for the thermal contact resistance, which is based on physical fundamentals. Sullivan [1972] developed a model for convective heat transfer to granular flows. The model contains an experimental constant describing the thermal contact resistance between particles and the wall. For flows with high velocity, the contact resistance plays a particularly significant role. The model was correlated well with Sullivan's experimental data taken in a vertical hopper. For moving beds or stirred beds, Schlünder [1984] developed a model combining the contact resistance at the wall and the heat penetration resistance of the bulk. The model presented by Schlünder is, in fact, of the same form as that of Sullivan if the residence time of the moving bed on the heating wall is regarded as the velocity term in Sullivan's work.

The models of Sullivan and Schlünder, however, fail to predict the behavior

of fast flows with low solid fraction. In experiments in an inclined chute, Spelt *et al.* [1982] show that Sullivan's correlation accurately describes the characteristic of heat transfer to slow flows, but overpredicts results for fast flows. Patton *et al.* [1986] have found that for slow flows with high solid fraction (or subcritical flows) heat transfer characteristics follow Sullivan's correlation, but that once flows become supercritical with high velocity and low density the heat transfer rate decreases, deviating from the prediction of Sullivan, because of the decrease in solid fraction. In order to consider the effect of solid fraction variations, they have developed a model using Reynolds analogy. One of the disadvantages in the model, however, is that, in addition to the experimental constant for the thermal contact resistance, another parameter for solid fraction variation needs to be determined experimentally. Therefore, it is desirable to develop a simpler model which may be derived from more fundamental understanding of heat transfer characteristics.

In the present work, the models developed by Sullivan and Schlünder have been modified to include the effect of solid fraction variations, so that the slightly modified model may describe the heat transfer characteristics of both fast and slow flows (supercritical and subcritical flows). Furthermore, in order to explore a possibility of using numerical method for heat transfer analysis, a simple numerical analysis has been conducted. One of the advantages of the present analysis is that heat transfer can be predicted without determining any experimental constant. However, further improvement associated with assumptions in the analysis is required.

CHAPTER 2
ANALYTICAL BACKGROUND

Some of the existing governing equations and constitutive equations for granular material flows, especially those of Lun *et al.* [1984], will be reviewed in this chapter. They will serve as the framework for the analysis of fully developed chute flow, and the rheological models will be compared with the present experimental data.

2.1 GOVERNING AND CONSTITUTIVE EQUATIONS

The continuity equation, the momentum equations, and the translational fluctuation energy equation for granular materials are written in continuum forms as follows:

$$\frac{d\rho}{dt} = -\rho \nabla \cdot \mathbf{u} \tag{2.1}$$

$$\rho \frac{d\mathbf{u}}{dt} = \rho \mathbf{b} - \nabla \cdot \mathbf{P} \tag{2.2}$$

$$\frac{3}{2}\rho \frac{dT}{dt} = -\mathbf{P} : \nabla \mathbf{u} - \nabla \cdot \mathbf{q} - \gamma \tag{2.3}$$

In these equations, $\rho = \rho_p \nu$ represents the bulk density, where ρ_p is the particle density and ν is the solid fraction. The bulk velocity and the body force per unit mass are represented by $\mathbf{u}$ and $\mathbf{b}$ respectively, and $\mathbf{P}$ is the stress tensor. The granular temperature, T, is defined by $\frac{1}{3}(\langle u'^2 \rangle + \langle v'^2 \rangle + \langle w'^2 \rangle)$ where u', v', and w' are the three velocity fluctuation components. Finally, $\mathbf{q}$ is the flux of fluctuation energy, and γ is the rate of the dissipation of fluctuation energy per unit volume. In the translational fluctuation energy equation, the term $-\mathbf{P} : \nabla \mathbf{u}$ represents the work done to the system by the stresses, and the so-called conduction term, $-\nabla \cdot \mathbf{q}$, represents the fluctuation energy added to the system through the conduction of granular temperature.

The literature contains many proposed constitutive equations. Most of them, however, are not applicable over the entire range of solid fraction. For example,

the expressions of Jenkins and Savage [1983] fail at the boundary of the free surface of the chute flow. Only the results presented by Lun *et al.* [1984] seem to be satisfactory for application to chute flows. Following Lun *et al.*, the total stress tensor is written as

$$\mathbf{P} = \left\{ \rho_p g_1(\nu, e_p) T - \rho_p d \frac{8\sqrt{\pi}}{3} \eta \nu^2 g_0 T^{\frac{1}{2}} \nabla \cdot \mathbf{u} \right\} \mathbf{I} - 2\rho_p d g_2(\nu, e_p) T^{\frac{1}{2}} \mathbf{S}, \qquad (2.4)$$

where $\mathbf{I}$ is the identity matrix and $\mathbf{S}$ is given as $\mathbf{S} = \frac{1}{2}(u_{i,j} + u_{j,i}) - \frac{1}{3} u_{k,k} \delta_{ij}$. The particle diameter is d, and $\eta = (1 + e_p)/2$ where e_p is the coefficient of restitution for collisions between particles. The flux vector of fluctuation energy is

$$\mathbf{q} = -\rho_p d (g_3(\nu, e_p) T^{\frac{1}{2}} \nabla T + g_4(\nu, e_p) T^{\frac{1}{2}} \nabla \nu), \qquad (2.5)$$

and the rate of dissipation per unit volume is

$$\gamma = \frac{\rho_p}{d} g_5(\nu, e_p) T^{\frac{3}{2}}. \qquad (2.6)$$

Here $g_1(\nu, e_p), g_2(\nu, e_p), g_3(\nu, e_p), g_4(\nu, e_p)$, and $g_5(\nu, e_p)$ are the functions of ν and e_p as follows:

$$\begin{aligned}
g_1(\nu, e_p) &= \nu + 4\eta\nu^2 g_0, \\
g_2(\nu, e_p) &= \frac{5\sqrt{\pi}}{96} \left(\frac{1}{\eta(2-\eta)} \frac{1}{g_0} + \frac{8}{5} \frac{3\eta - 1}{2 - \eta} \nu + \frac{64}{25} \eta \left(\frac{3\eta - 2}{2 - \eta} + \frac{12}{\pi} \right) \nu^2 g_0 \right), \\
g_3(\nu, e_p) &= \frac{25\sqrt{\pi}}{16\eta(41 - 33\eta)} \left(\frac{1}{g_0} + \frac{12}{5} \eta \{1 + \eta(4\eta - 3)\} \nu \right. \\
&\quad \left. + \frac{16}{25} \eta^2 \{9\eta(4\eta - 3) + \frac{4}{\pi}(41 - 33\eta)\} \nu^2 g_0 \right), \\
g_4(\nu, e_p) &= \frac{15\sqrt{\pi}}{4} \frac{(2\eta - 1)(\eta - 1)}{41 - 33\eta} \left(\frac{1}{\nu g_0} + \frac{12}{5} \eta \right) \frac{d}{d\nu} (\nu^2 g_0), \\
g_5(\nu, e_p) &= \frac{48}{\sqrt{\pi}} \eta (1 - \eta) \nu^2 g_0.
\end{aligned}$$

And g_0, the radial distribution function, is chosen as suggested by Lun and Savage [1986], as follows:

$$g_0 = \left(1 - \frac{\nu}{\nu^*} \right)^{-2.5\nu^*},$$

where ν^* is the maximum shearable solid fraction for spherical particles. It should be noted that g_1, g_2, g_3, and g_5 are positive quantities for all ν and e_p while g_4 is always negative. Furthermore, g_1 and g_5 vanish as $\nu \rightarrow 0$ while g_0, g_2, g_3, g_4, and all the derivatives of g_0, g_1, g_2, g_3, g_4 with respect to ν do not vanish as $\nu \rightarrow 0$.

2.2 APPLICATION TO TWO-DIMENSIONAL FLOW

For two-dimensional steady flow, the constitutive equations for the normal and shear stresses become

$$P_{xx} = P_{yy} = \rho_p g_1 T - \rho_p d \frac{8\sqrt{\pi}}{3} \eta \nu^2 g_0 T^{\frac{1}{2}} \frac{\partial u}{\partial x}, \tag{2.7}$$

$$P_{xy} = P_{yx} = -\rho_p d g_2 \frac{\partial u}{\partial y} T^{\frac{1}{2}}, \tag{2.8}$$

where x and y are coordinates in the flow direction and in the direction normal to the flow respectively. In most flows where no significant acceleration in the x-direction exists, the second term in equation (2.7) can be neglected, and thus the normal stresses are approximated as

$$P_{xx} = P_{yy} = \rho_p g_1 T. \tag{2.9}$$

For simple shear flow where the velocity gradient is constant with uniform density and granular temperature, or for fully developed flow where all the quantities are invariant in the flow direction, equation (2.9) is the exact expression of equation (2.7). From equation (2.5), the y-component of fluctuation energy flux is given as

$$q_y = -\rho_p d \left(g_3 T^{\frac{1}{2}} \frac{\partial T}{\partial y} + g_4 T^{\frac{3}{2}} \frac{\partial \nu}{\partial y} \right). \tag{2.10}$$

The dissipation term in equation (2.6) remains unchanged.

2.2.1 Simple Shear Flow

For simple shear flow with uniform density and granular temperature, the continuity equation and the momentum equations are automatically satisfied. Since no fluctuation energy flux exists in the flow (see equation (2.10)), the

conduction term in the energy equation (2.3) vanishes. Therefore, the shear work term and the dissipation term should balance, and the fluctuation energy equation (2.3) simplifies to

$$0 = -P_{yx}\frac{\partial u}{\partial y} - \gamma. \tag{2.11}$$

Using this equation with (2.6) and (2.8), the ratio of the characteristic velocity gradient to the granular temperature is obtained as follows:

$$S = \frac{d\frac{du}{dy}}{T^{\frac{1}{2}}} = \left(\frac{g_5}{g_2}\right)^{\frac{1}{2}}. \tag{2.12}$$

Note that S is a function only of ν and e_p. Therefore, (2.9) and (2.8) can be written as follows:

$$P_{yy} = \rho_p\left(d\frac{du}{dy}\right)^2\frac{g_1 g_2}{g_5}, \tag{2.13}$$

$$P_{yx} = \rho_p\left(d\frac{du}{dy}\right)^2\frac{{g_2}^{3/2}}{{g_5}^{1/2}}. \tag{2.14}$$

The ratio of shear stress to normal stress, or friction coefficient, is also a function only of ν and e_p.

2.2.2 Fully Developed Chute Flow

In fully developed flow in an inclined chute, the derivatives parallel to the plane are zero. Therefore, the continuity equation (2.1) is automatically satisfied, and the momentum equations (2.2) become

$$\frac{\partial P_{yy}}{\partial y} = -\rho_p \nu g \cos\theta, \tag{2.15}$$

$$\frac{\partial P_{yx}}{\partial y} = \rho_p \nu g \sin\theta, \tag{2.16}$$

where θ is the angle of the chute inclination and g is the gravitational acceleration. Note that for the fully developed chute flow $-P_{yx}/P_{yy} = \tan\theta$. From equations (2.8) and (2.9), therefore, S is given by

$$S = \frac{d\frac{du}{dy}}{T^{\frac{1}{2}}} = \frac{g_1}{g_2}\tan\theta. \tag{2.17}$$

It should be noted that S is a function not only of ν and e_p but also of $\tan\theta$. And since ν varies over the depth of the chute flow, S also varies, tending to zero at the free surface. Under these circumstances (2.9) and (2.8) can be written as

$$P_{yy}\tan^2\theta = \rho_p\left(d\frac{du}{dy}\right)^2\frac{{g_2}^2}{g_1}, \tag{2.18}$$

$$P_{yx}\tan\theta = \rho_p\left(d\frac{du}{dy}\right)^2\frac{{g_2}^2}{g_1}. \tag{2.19}$$

Since fully developed chute flow does not have uniform temperature and solid fraction over the depth of flow, the conduction term remains in the energy equation (2.3) and it plays an important role in determining the profiles of granular temperature, solid fraction, and velocity (see Ahn *et al.* [1989b]). The fluctuation energy equation simplifies to

$$0 = -P_{yx}\frac{\partial u}{\partial y} - \frac{\partial q_y}{\partial y} - \gamma. \tag{2.20}$$

These characteristics of chute flows will be important in considering the experimental results presented in the next chapter, and the governing equations and the constitutive equations for fully developed chute flow will be employed in the analysis presented in chapter 4.

CHAPTER 3
EXPERIMENTAL STUDY OF SHEAR FLOWS OF GRANULAR MATERIALS

3.1 APPARATUS AND PROCEDURE

Granular materials flowing down an inclined chute were studied experimentally to understand the characteristics of chute flows and to acquire information on the rheological behavior of granular flows.

The present experiments were conducted in a long rectangular aluminum channel or chute, 7.62 cm wide and 1.2 m long. The aluminum base of the chute was 3.2 mm thick, and the aluminum sidewalls were 6.4 mm thick and 10.2 cm high. The chute was installed in a continuous flow, granular material facility, as previously described in Patton [1985] (see Figure 3.1). Slight modification was made on the facility built by Patton to accommodate a chute of smaller width and shorter length than that of Patton. The material entered the chute from an upper feed hopper and was collected in a collecting hopper from which, in turn, a mechanical conveyor delivered the material to the upper hopper. The conveyor was about 6 m long and capable of delivering coarse sand at a maximum flow rate of 70 tons per hour. The channel was positioned at different angles, θ, to the horizontal, from about 13° to 36°. Measurements were taken only after a steady state flow had been established. The flow into the channel was regulated by a vertical gate, and the opening between the gate and the channel base is referred to as the entrance gate height, h_o.

In these experiments two sizes of glass beads were used as granular materials; one is of mean diameter $d = 1.26$ mm with 2.9% standard deviation, and the other has $d = 3.04$ mm with 7.2% standard deviation. The maximum shearable solid fraction, ν^*, of the 1.26 mm beads is 0.61. For the 3.04 mm beads, ν^* is 0.59. The density of both granular materials is $\rho_p = 2500\,\mathrm{kg/m^3}$.

Two important instruments were used in the experiments; one is a gauge to

measure shear stress, and the other is a set of two fibre optic probes to measure mean velocity and velocity fluctuation. In order to measure shear stress of flowing material at the chute base, a rectangular hole, 11.4 cm long and 3.8 cm wide, was cut into the chute base and replaced by a plate supported by strain-gauged flexures sensitive to the shearing force applied to the plate. (See Figure 3.2). The clearance between the plate and the rest of the chute base was adjusted to be about 0.2 mm, much smaller than the particle sizes. Nevertheless, dirt would occasionally get trapped in the gap, and this necessitated cleaning of the gap and calibration of the gauge prior to each measurement. Calibration of this balance was achieved by placing weights on the plate with the channel set at various inclinations. The detailed procedure was as follows. The channel was set at an inclination of about 13°, and an offset voltage was read from the strain gauge. A 50 or 100 gram weight was placed on the shear plate, and the voltage difference was measured. This procedure was repeated at a different inclination of about 27°. The two voltage differences, the inclination angles, and the mass of the weight were used to obtain two calibration coefficients corresponding to the shear and normal forces on the plate. After calibration, from about 5 seconds before a flow started until about 10 seconds after the flow became steady, signals from the strain gauge were continuously read by a data acquisition system. The shear stress was then calculated from the average voltage output from the gauge, the calibration coefficients, and the normal stress calculated from the measurements of the flow depth and the mean solid fraction.

A system of fibre optic probes, similar to that originally devised by Savage [1979], was developed to measure particle velocities and their fluctuations at the chute base, the free surface, and the sidewalls. The system consisted of two MTI fibre optic displacement probes set with their faces flush in a lucite plug which was, in turn, either set flush in the chute base or sidewalls or held close to the free surface of the flowing granular material. The probe faces were 1.6 mm in diameter and of the type in which one semi-circle of the face consisted of transmitting fibres

and the other of receiving fibres. The specific geometry is shown in Figure 3.3. The distance between two displacement probes was selected to be about two particle diameters. This distance was carefully calibrated by placing the probes close to a revolving drum to which particles had been glued, and comparing the drum peripheral velocity with the velocity measured from the probe output.

The output from these velocity measuring devices was processed in the following way. First the signals from each of the two displacement probes were simultaneously digitized and stored using a data acquisition system that consisted of an analog-digital converter connected to the Zenith 140 personal computer. The sampling rate was adjusted so that, whatever the mean velocity of particles was, each of the two records detected the passage of 300 $\sim$ 600 particles. The time was measured by the 8253 Intel Programmable Timer installed inside the computer. The fastest sampling rate, at which most data were taken, was about 32 microseconds. Each record contained 8000 samples, and the total record time was about 0.5 second for most flows. The two records were digitally cross-correlated over the entire record in order to obtain the mean particle velocity, u. Figure 3.4 shows typical signals from the two probes, and the cross-correlation of these signals is presented in Figure 3.5. Furthermore, as shown in Figure 3.4, thresholds were set to identify the peaks on the two records corresponding to the passage of a particular particle. Since an average value of the time interval between the two peaks was obtained from the cross-correlation, identification of the two peaks of a particular particle in the two records was rather easily performed. When no such correspondence could be firmly established or where the peak was below a certain threshold, the data were discarded for the purposes of this second part of the analysis. However, where positive identification was made, the velocity of that individual particle was obtained from the time interval between the peaks it generated on the two records. In this way, a set of instantaneous particle velocities were obtained, and ensemble-averaging was used to obtain both the mean velocity, u, and the root-mean-square of velocity

fluctuation, u'. Though the latter represents only one component of velocity fluctuations, it should be some measure of granular temperature. Finally, the number of particle passages per unit time detected by the probe was divided by the mean velocity to obtain the characteristic particle spacing, s, and in turn the linear concentration, ν_{1D}, was calculated as $\nu_{1D} = d/s$ where d is the particle diameter. An estimate of the local solid fraction near the wall, ν_w, was calculated using $\nu_w = \pi\nu_{1D}^3/6$. All of these procedures (taking data, cross-correlating, searching and setting the most effective thresholds, identifying the peaks of particles, and calculation) were automatically controlled by the personal computer. In order to enhance the speed of the procedures, the computer was supported by the 8087-2 Numeric Coprocessor, and it typically took about a minute to complete the whole calculation.

In addition, point probes were used to record the depth, h, of flow at several longitudinal locations in the channel. Mass flow rate, $\dot{m}$, was obtained by timed collection of material discharging from the chute. Mean velocities at the chute base and at the free surface obtained by the fibre optic probes were averaged to give the average mean velocity, u_m, over the depth of the flow. For most flows, h was from 0.6 to 3 cm, $\dot{m}$ from 0.4 to 3 kg/sec, and u_m from 0.4 to 3 m/sec. A mean solid fraction, ν_m, could then be obtained as $\nu_m = \dot{m}/\rho_p h b u_m$ where b is the channel width. Furthermore, mean shear rate was calculated as $\Delta u/h$ where Δu is the difference between the two velocities at the base and at the free surface, and h is the depth of the flow. Normal stress was calculated by $\tau_N = \rho_p \nu_m g h \cos\theta$ where g is the gravitational acceleration, and shear stress, τ_S, was measured directly by the shear gauge. All the above measurements except for shear stress were made at two stations located at 72 cm and 98 cm downstream from the entrance gate. The shear gauge was located in the middle of these two stations. It should be noted that ν_w, u, u', τ_N, and τ_S are local properties while ν_m and $\Delta u/h$ represent quantities averaged over the depth of flow.

The procedure used to acquire the data was as follows. The angle of the

chute inclination and the entrance gate opening were set. After a steady flow was established, mean velocity, velocity fluctuations, and linear concentration both at the chute base and at the free surface were measured using two fibre optic probes at a station. If necessary, this procedure was repeated. The fibre optic probes were moved to another station, and measurements of various quantities were repeated. During these measurements, the mass flow rate and the depths of flow were measured several times. Then the gap between the shear plate and the rest of the chute base was cleansed, and calibration of the shear gauge was performed. After calibration a steady flow was established and the shear stress was measured. Cleaning of the gap, calibration of the shear gauge, and measurement of shear stress were repeated if necessary.

Measurements of u_w, u_s, and u'_w were repeatable within $\pm 1\%$, $\pm 3\%$, and $\pm 12\%$ respectively. The scatter in measurements of the mass flow rate was less than 1% of the average value. Repeatability of measurements of stresses was about $\pm 2\%$. Most errors in the whole procedure seemed to result from measurement of the depth of flow because the free surface was not well-defined.

Preliminary tests suggested that the flow could be influenced by the surface conditions of the chute base. Indeed the data were quite sensitive to the degree of the cleanliness of the aluminum chute base. Therefore, it was possible to create different surface conditions with the aluminum chute by controlling the cleanliness. In addition, a very thin film of liquid rubber (Latex) was applied to the chute base to give a totally different surface condition. This film was about 0.2 mm thick. Before conducting experiments, the chute was run long enough to achieve a steady state surface condition. With these precautions, data will be classified in this presentation by whether the chute base was "smooth," "moderately smooth," or "rubberized." To systematically characterize these different surface conditions, Coulombic friction coefficients were measured using the shear gauge and a block to which glass beads were glued. That is, after calibrating the shear gauge, a block under which glass beads were glued was set

in motion to slide down over the shear gauge. The whole signal was stored into the data acquisition system, and was carefully read to obtain the shear force exerted by the block upon the shear gauge. Two blocks with different weights (about 10 and 30 grams) were used to examine the effect of the normal force variation. No significant difference was observed. The surface condition of the aluminum plate of the shear gauge was maintained as close to that of the chute base as possible. The kinematic Coulombic friction coefficient of the smooth surface was 0.15; the moderately smooth and rubberized surface had coefficients of 0.22 and 0.38 respectively. Furthermore, smooth and moderately smooth surfaces yielded coefficients of restitution different from that of the rubber-coated surface; the former was 0.7 while the latter 0.5. These coefficients of restitution, e_w, between the wall surface and a particle should be distinguished from that between two particles, e_p.

3.2 PRELIMINARY MEASUREMENTS

3.2.1 Transverse Profiles

Originally the chute was designed to be wide enough to yield almost two-dimensional flow. To examine the effect of the sidewalls (and the extent to which this objective was achieved), fibre optic probe measurements were made at several lateral locations with various chute inclinations. The 1.26 mm glass beads were used in measurements of the transverse velocity profiles, and the surfaces of the aluminum chute base as well as the sidewalls were smooth. Velocities normalized by the velocity at the centerline are plotted in Figure 3.6. Comparison of the profiles on the free surface and on the chute base indicates that the flow at the free surface is more uniform and less affected by the sidewall than the flow at the base. This is a "corner effect" in which particles in the corner are slowed both by the chute base and the side wall. One could visually observe that particles in the corner were arranged in a distinct line that had high solid fraction and low velocity. It should also be noted from Figure 3.6 that the higher the velocity (or

the higher the chute inclination), the less significant the sidewall effect. Thus nonuniformity due to the sidewall was significant only at the base and at low velocities (low inclinations). We were particularly concerned about the sidewall effect on the shear gauge whose width was one half of that of the channel. The above results indicated that this sidewall effect would be very small.

3.3.2 Vertical Profiles

Vertical profiles were obtained by making measurements through lucite windows in the sidewalls. Savage [1979] made similar efforts to obtain velocity profiles at the sidewalls using fibre optic probes. Bailard [1978] obtained the vertical profiles of velocity and solid fraction by measuring cumulative mass flux profiles. Campbell and Brennen [1985b] in the computer simulation with circular discs obtained the profiles of velocity, granular temperature, and solid fraction. In the present work, fibre optic probes were used to measure velocity, its fluctuation, and linear concentration. It should be noted that, usually, fully developed flow could not be achieved because of the finite length of the chute.

Examples of vertical profiles for 3.04 mm glass beads with the rubberized surface are presented in Figure 3.7. The angle of the chute inclination was 17.8°. As illustrated in Figure 3.7 (a), velocity profile is fairly linear except within a distance of about one particle diameter from the base. The uniform velocity within the distance of one particle diameter indicates that there is a distinct layer at the corner, preventing particles from entering the layer from above, assuring the existence of the "corner effect." Note that the ratio of velocity at the base to that at the free surface is about one half, which is comparable with the results of the computer simulation by Campbell and Brennen [1985b]. This result should be distinguished from those of Savage [1979] and Bailard [1978] where almost zero velocity was obtained at the chute surfaces roughened by rough rubber sheets or attached particles.

Velocities at the center of the chute, both at the base and the free surface, are shown in Figure 3.7 (a) for comparison with the velocities at the sidewall. At the

free surface, the velocities at the center and at the sidewall are almost equal. But at the base there is some discrepancy due to the corner effect. This characteristic of the data suggests that the velocity profile in the center of the chute is similar to that at the sidewall except within one particle diameter distance from the base. An assumed velocity profile at the center is shown by the dotted line in Figure 3.7 (a). We also conclude from these observations that the shear rate, du/dy, can be approximated by the difference between the base and free surface velocities, Δu, divided by the depth, h, of the flow. This approximation has been used throughout the analysis which follows.

The profile of velocity fluctuations at the sidewall is presented in Figure 3.7 (b). It can be seen that the profile is fairly linear, and that fluctuations are larger at the free surface than at the chute base. Comparison between the sidewall and center values is also included in Figure 3.7 (b). At the free surface, no significant difference is encountered between the velocity fluctuations at the sidewall and at the center. But at the base, a small discrepancy is observed, which is again believed to be due to the corner effect. This fairly linear profile for velocity fluctuation was observed in most flows. Furthermore, the fluctuations were always higher at the free surface than at the base of the chute. These overall features are in contrast to the results obtained by Campbell and Brennen [1985b]. In their computer simulation, granular temperature near the solid wall was substantially higher than near the free surface, and the profile was far from linear. We believe this difference is probably due to the fact that 0.6 was used for e_p in the computer simulation while e_p for glass beads is more like 0.95 (Lun and Savage [1986]; refer to Ahn *et al.* [1989b] for more detail).

When Figure 3.7 (b) is closely examined, it raises some complicated problems in measurements of granular flows. For instance, a slight peak in the velocity fluctuation was consistently observed at a distance of one particle diameter from the chute base. This location coincides with the interface between the first and second layers of particles, which are quite distinct because of the corner effect.

Within each distinct layer, the fibre optic probes measure only longitudinal fluctuations for the particles within that layer. At the interface, however, particles from both layers contribute, and hence the difference in the mean velocities in the two layers enters into the result. Therefore, the fluctuations at the interface were observed to be slightly higher than elsewhere.

The profile of linear concentration, ν_{1D}, is presented in Figure 3.7 (c). Again, in the region near the base, the locations of the first and second layers and their interface can be determined by the details of the profile. The peak at $y/d \simeq 0.5$ indicates the location of the center of the first layer; the interfacial region has a lower concentration; the peak at $y/d \simeq 1.7$ corresponds to the center location of the second layer. This detailed structure seems to disappear above the second layer. Near the free surface, the linear concentration decreases gradually, and as a result it is difficult to determine the depth of flow accurately.

The monotonic decrease of solid fraction with distance from the wall as shown in Figure 3.7 (c) was a somewhat unexpected result. From previous experiments (Bailard [1978]) and from computer simulations (Campbell and Brennen [1985b]), it has been observed that solid fraction increases with distance from the base and it vanishes at the free surface after it achieves its maximum in the bulk. One of the reasons may be the difference in the boundary conditions used in the experiments. The experiments of Bailard used the surface on which particles were glued to create a no-slip condition at the boundary. On the other hand, the present experiments used relatively smooth surfaces. The discrepancy between the present data and the result of Campbell and Brennen may arise from the fact that the value of e_p used by Campbell and Brennen is different from that of the glass beads in the present experiments. The results of Ahn *et al.* [1989b] show that the profile of solid fraction can be either of Campbell and Brennen or of the present one, depending on the value of e_p.

Sidewall measurements at a higher angle of chute inclination with the rubberized surface and 3.04 mm glass beads are presented in Figure 3.8. The angle

was 22.7°, and the entrance gate opening was chosen to be smaller than that of Figure 3.7. The general features of the profiles are similar to those of Figure 3.7. The velocity profile is again fairly linear. The velocity fluctuation increases with distance from the chute base. The density profile exhibits monotonic decrease from the base to the free surface. Compared to the results of Figure 3.7, which were obtained at $\theta = 17.8°$, there is about a 40% increase in velocity and about a 100% increase in velocity fluctuation; the solid fraction gradient near the wall is larger than that of Figure 3.7. Measurements at the center of the chute are also plotted in Figure 3.8. Just as in Figure 3.7 (a), at the free surface the velocity at the center is equal to that at the sidewall while at the chute base some discrepancy is observed due to the corner effect. The fact that the detailed structure of the layers in the velocity profile is indistinct compared to that of Figure 3.7 indicates there is a convective process between the first and second layers.

Measurements on the smooth aluminum chute base are presented in Figure 3.9. The chute inclination was 22.7°, and the 1.26 mm glass beads were used. Compared to the data on the rubberized surface, the profiles of velocity and velocity fluctuation are more uniform. The velocity at the wall is more than 80% of that at the free surface. Velocity fluctuation is fairly uniform although there is a slight increase with distance from the chute base. The detailed structure of the layers due to the corner effect is clearly observed in all the profiles.

3.3 PRESENTATION OF EXPERIMENTAL DATA

3.3.1 Experimental Data on Basic Flow Properties

In this section, we examine how basic flow properties (such as velocities, velocity fluctuation, and shear rate) vary with solid fraction. Two kinds of solid fraction are used in this presentation; mean solid fraction, ν_m, and wall solid fraction, ν_w. The mean solid fraction is an average value over the depth of flow, and the wall solid fraction describes a density in the vicinity of the chute base. Because it is calculated from a measurement of linear concentration, the wall

solid fraction may not represent accurately the local solid fraction near the wall, but it is at least a qualitative, comparative measure.

The ratio of velocity at the wall, u_w, to velocity at the free surface, u_s, is plotted against mean solid fraction in Figure 3.10. Different symbols are used for different surface conditions. For the smooth surface, the ratio u_w/u_s is fairly constant and greater than 0.9, implying that the velocity profile over the depth is close to uniform. On the other hand, for the rubberized surface, the ratio increases with decreasing ν_m. In other words, the lower the solid fraction, the more uniform the velocity profile. Note the rather sudden change of u_w/u_s at $\nu_m \simeq 0.1$, which will be discussed later. As expected, the data for the moderately smooth surface lie between those for the smooth surface and the rubberized surface.

The mean shear rate, $\Delta u/h$, is plotted against mean solid fraction in Figure 3.11. For the smooth surface (see Figure 3.11 (a)), the shear rate monotonically increases with decreasing ν_m. (Recall, however, u_w/u_s remains constant as shown in Figure 3.10.) On the other hand, the moderately smooth and rubberized surfaces (see Figures 3.11 (b) and (c)) yield shear rates which first increase and then decrease as the solid fraction decreases. The values of ν_m at which the shear rate is a maximum are about 0.3 for the moderately smooth surface, and about 0.2 for the rubberized surface regardless of the particle size. Note that the steep change of the shear rate at $\nu_m \simeq 0.1$ for the rubberized surface corresponds to that of u_w/u_s in Figure 3.10.

The variation of the velocity fluctuation at the wall, u'_w, with wall solid fraction is examined in Figure 3.12 (a). Regardless of surface conditions, u'_w increases with decreasing ν_w. The use of wall solid fraction was essential for the examination of the local quantity u'_w. To illustrate this, the local quantity u'_w was plotted against the mean quantity ν_m as shown in Figure 3.12 (b). The use of the mean quantity with the local quantity leads to a wide scattering of the data. If examined more closely, the data reflected a strong dependency on

the entrance gate opening h_o. As observed in Figure 3.12 (b), the data have a distinct line for each h_o. This is because the mean solid fraction is closely related to h_o. Note that fully developed flow was not achieved in the present experiments (this will be discussed later). Therefore, the test section was directly affected by entrance conditions governed by h_o. When ν_w is used, the dependency on h_o largely disappears as shown in Figure 3.12 (c).

It is also interesting to present the velocity fluctuation in a nondimensionalized form. In Figure 3.13, the velocity fluctuation normalized by the mean velocity is plotted against wall solid fraction. Note all the quantities are local values measured at the wall. The ratio of u'_w to u_w for the rubberized surface is larger than that for the smooth surface. The ratio u'_w/u_w for the smooth surface shows little variation with ν_w. For the moderately smooth surface, u'_w/u_w changes only mildly with ν_w. However, the rubberized surface clearly shows the increase of u'_w/u_w with decreasing ν_w.

3.3.2 Experimental Data on Friction Coefficient

As previously mentioned, shear stress was directly measured by the shear gauge, and normal stress was calculated as $\rho_p \nu_m g h \cos\theta$ where ρ_p is the density of particles, g is the gravitational acceleration, h is the depth of flow, and θ is the angle of the chute inclination. Note both stresses were measured at the chute base wall. Recall from section 3.1 that kinematic Coulombic friction coefficients, μ_c, were measured for each surface condition; 0.15 for the smooth surface, 0.22 for the moderately smooth surface, and 0.38 for the rubberized surface.

The ratio of shear stress to normal stress, or friction coefficient, f, is plotted against wall solid fraction in Figure 3.14. For the smooth and moderately smooth surfaces, friction coefficients appear to be fairly constant. Furthermore, the values of friction coefficients are comparable to the kinematic Coulombic friction coefficients for each surface (though f is slightly higher than μ_c). On the other hand, for the rubberized surface, the friction coefficient is a decreasing function of solid fraction. And the Coulombic friction coefficient for the rubberized surface

does not seem to directly affect the friction coefficient for the flowing material. Therefore it may be concluded that the different surface conditions result in quite different types of boundary condition at the wall.

In Figure 3.15, the friction coefficient is plotted against velocity fluctuation normalized by mean velocity, or u'_w/u_w. For the smooth and moderately smooth surfaces, all the data are clustered at one region. For the rubberized surface, f seems to correlate quite well with u'_w/u_w; f increases with increasing u'_w/u_w. This phenomenon is independent of particle size.

3.3.3 Experimental Results on Rheological Behavior

The rheological behavior of granular material will be examined in this section. Stresses measured at the wall of the chute base will be related to the density, the shear rate, and/or the velocity fluctuation. In particular, following the rheological models by Lun *et al.* [1984], stresses will be normalized by $\rho_p(u'_w)^2$ (see equation (2.9), for any kind of flow), by $\rho_p(d\Delta u/h)u'_w$ (see equation (2.8), for any kind of flow), by $\rho_p(d\Delta u/h)^2$ (see equations (2.13) and (2.14), for simple shear flow), and by $\rho_p(d\Delta u/h)^2/\tan^2\theta$ (see equations (2.18) and (2.19), for fully developed flow). Comparisons with the results of Lun *et al.* will also be made. Note Lun *et al.* assume that the granular temperature is isotropic. Furthermore, they do not include the effect of particle rotation and surface friction. Therefore, some discrepancy may be expected in the comparison with the experimental data.

Normal stress normalized by $\rho_p(u'_w)^2$ is plotted against wall solid fraction in Figure 3.16 (a). Good correlation is found between the normalized stress and wall solid fraction with the former increasing with the latter. The data show no effect of surface conditions; all the data from the smooth, moderately smooth, and rubberized surfaces are fairly well correlated. When the normalized normal stress is plotted against the mean solid fraction as shown in Figure 3.16 (b), the data are more scattered. This may be explained by realizing that the normalized stress is a local quantity which should be related to the local wall solid fraction

rather than the mean solid fraction. In both figures, results for the rheological model postulated by Lun *et al.* [1984] (see equation (2.9)) are also plotted using $T = \langle u'^2 \rangle$.

Shear stress normalized by $\rho_p(d\Delta u/h)u'_w$ is plotted against wall solid fraction in Figure 3.17 (a). The normalized shear stress increases with increasing solid fraction. The data are also well correlated regardless of surface conditions. The results of Lun *et al.* [1984] (see equation (2.8)) are shown in the same figure for comparison. The discrepancy between the theoretical and experimental results is substantial. The normalized shear stress is presented again with mean solid fraction in Figure 3.17 (b).

In Figures 3.18 and 3.19, stresses normalized by $\rho_p(d\Delta u/h)^2$ are plotted against wall solid fraction and mean solid fraction. Lun *et al.* [1984] suggest that the stresses normalized by $\rho_p(d\Delta u/h)^2$ should be functions only of ν and e_p for the case of simple shear flow (see equations (2.13) and (2.14)). The normalized normal stress is plotted in Figure 3.18 and, contrary to the suggestion of Lun *et al.*, the data exhibit a dependency on the surface conditions; the data for each surface condition appear to conform to a different function over a wide range of solid fraction. These distinct curves for different surface conditions are independent of particle sizes. The rubberized surface clearly shows two asymptotes both at the high and low solid fractions. As ν approaches its maximum shear limit, ν^*, the normalized stress increases, and as $\nu \to 0$ a sharp increase is also observed. The data for the moderately smooth surface lie slightly above the data for the rubberized surface. The asymptote at low solid fraction shown in the data for the rubberized surface is not found in the data for the moderately smooth surface; the data cease decreasing and stay unvarying with decreasing solid fraction. The data taken from the smooth surface decreases monotonically with decreasing ν. The results from Lun *et al.* are also presented in Figure 3.18. The shear stress normalized by $\rho_p(d\Delta u/h)^2$ is plotted in Figure 3.19, and the results are similar to those of Figure 3.18.

Normal stress normalized by $\rho_p(d\Delta u/h)^2/\tan^2\theta$ and shear stress normalized by $\rho_p(d\Delta u/h)^2/\tan\theta$ are presented in Figures 3.20 and 3.21. The experimental data are too widely scattered to find any correlation with solid fraction. The data also show some dependency on surface conditions. Results for the rheological model presented by Lun *et al.* for fully developed flow are also plotted in Figures 3.20 and 3.21 (see equations (2.18) and (2.19)). Discrepancies between the experimental data and the theoretical results are substantial.

Finally, the parameter introduced by Savage and Jeffrey [1981],

$$S = \frac{d\frac{du}{dy}}{T^{\frac{1}{2}}}$$

is examined. Lun *et al.* [1984] suggest that S or $S/\tan\theta$ should be a function only of ν and e_p for the case of simple shear flow or fully developed flow respectively. (See equations (2.12) and (2.17).) In Figure 3.22, $d(\Delta u/h)/u'_w$ as an approximation of S is plotted against wall solid fraction, and the approximation of $S/\tan\theta$ is presented in Figure 3.23. In both figures, the data are widely scattered, showing strong dependency on surface conditions. For the rubberized surface, however, the data seem to increase with increasing ν.

From the experimental results on rheological behavior presented in this section, we observe that the data are fairly well correlated when the stresses are presented following the models of equations (2.8) and (2.9). When the stresses are normalized following the model for simple shear flow, the data exhibit a dependency on the surface conditions. When the stresses are normalized following the models for fully developed flow, the data are widely scattered. These will be discussed in the next section.

3.4 DISCUSSION

3.4.1 The Characteristics of Chute Flows

It is apparent from Figure 3.10 that the surface condition has considerable influence on the characteristics of chute flow. Different results have been achieved

by several authors when different surface conditions are used. For example, Bailard [1978] used a surface on which grains were glued, and Savage [1979] applied roughened rubber sheets to the surface. In both cases, the ratio of u_w to u_s was close to zero. Augenstein and Hogg [1978] obtained various u_w/u_s for various surface roughnesses. When a smooth surface with high friction coefficient was used by Campbell and Brennen [1985b] in computer simulations, the ratio of u_w to u_s was about $0.4 \sim 0.5$. The rubberized surface of the present experiments, therefore, is similar to those cases in Campbell and Brennen in which a no-slip condition at the contact surface was assumed. Despite these data, the present state of knowledge does not allow prediction of the slip at the wall. Indeed the features of the surface or of the flow which determine the slip are not well understood.

The surface conditions also influence velocity fluctuations at the wall as observed in Figure 3.13. For the smooth and moderately smooth surfaces, the ratio of u'_w to u_w is low and fairly constant. On the other hand, u'_w/u_w for the rubberized surface is high and increases as solid fraction decreases. These observations may imply the following: The rubberized surface is characterized by large velocity fluctuations particularly at lower solid fractions. The high fluctuations and the low solid fraction allow particles to move more freely from one location to another. One of the effects by these random motions is a decrease of velocity gradient in the direction normal to the flow. That is, when particles move from a layer with low mean velocity to a subsequent layer with high velocity, the mean velocity of the layer with high velocity is reduced. When particles move due to random motion from the upper layer with high mean velocity to the lower layer with low mean velocity, the opposite is true. This phenomenon is consistent with experimental observations. For the rubberized surface, u_w/u_s rather sharply increases at $\nu \simeq 0.1$ as the solid fraction is decreased (see Figure 3.10). As also observed in Figure 3.11 (c), the shear rate decreases as solid fraction decreases. For the smooth surface shown in Figure 3.11 (a), however, this decrease of the

shear rate is not observed since no substantial velocity fluctuation exists (see the data for the smooth surface in Figure 3.13).

3.4.2 Friction Coefficient and Boundary Conditions

In the present work, an attempt to investigate boundary conditions was made by changing chute surface conditions. The Coulombic friction coefficient, μ_c, was measured for each surface since it was anticipated that μ_c would be a major factor which determines whether or not particles slip when in contact with a solid boundary. Here the word "slip" means the tangential slip between the contact surfaces of the particle and the wall. The slip velocity is different from a velocity at the wall, u_w, which is the velocity of the particle center extrapolated to the wall. Clearly, even when slip velocity is zero, a particle touching the wall may roll and thus have non-zero center velocity.

When a particle collides with a wall such that the shear stress at the contact point exceeds a shear stress limit which the surface can withstand for the given normal stress at the contact point, slip will occur. Then the ratio of the shear stress to the normal stress at the contact point is adjusted to the Coulombic friction coefficient of the surface, i.e. $f = \mu_c$. On the other hand, when the ratio of τ_S to τ_N at the impact does not exceed μ_c, there will be no slip between the contact surfaces of the particle and the wall. In this case f is different from μ_c.

As seen in Figure 3.14, friction coefficients for the smooth and moderately smooth surfaces seem to be fairly constant. But for the rubberized surface the friction coefficient decreases with increasing solid fraction. Decreasing friction coefficients with increasing ν were also observed in the shear cell experiments of Savage and Sayed [1984] and in the computer simulations of Campbell [1989a]. However, the constant friction coefficients of the smooth and moderately smooth surfaces have not been observed previously. To explain these observations, we suggest the following. For the smooth and moderately smooth surfaces, slip occurs at the contact between particles and the surfaces, and the slip condition results in the constant friction coefficients equal to μ_c. On the other hand, the

varying friction coefficient for the rubberized surface suggests a no-slip condition at the boundary. The high Coulombic friction coefficient of the rubberized surface would inhibit any slip at the contact between particles and the surface.

When there is no slip, the following relation results from a simple analysis of the oblique impact of a single sphere on the flat surface [see appendix A]:

$$f = \frac{2}{7}\left(1 - \frac{\omega_1 r}{u_1}\right)\frac{\tan\alpha_1}{1+e_w}$$

where ω_1 is the rotational rate before impact, r is the radius of the sphere, and u_1 is the velocity tangential to the wall before impact. The impact angle α_1 is defined by $\tan^{-1}(u_1/v_1)$ where v_1 is the velocity normal to the wall before impact, and e_w is the wall-particle coefficient of restitution. In this equation, the friction coefficient or the ratio of τ_S to τ_N at the surface depends on the ratio of rotational velocity to tangential velocity, $\omega_1 r/u_1$, and on the impact angle, $\tan\alpha_1$.

In the present experiments, the value of $\tan\alpha_1$ could not be estimated. Another factor influencing f is the ratio of the rotational velocity ωr to the tangential velocity u before impact. Campbell [1988] has shown that next to the wall ω is considerably larger than the mean value, but that with a small distance from the wall ω is slightly less than the mean value. Therefore, when a particle next to the wall with high ω hits the wall, the friction coefficient will be low, but if a particle at a distance from the wall with low ω comes down and collides with the wall, the friction coefficient will be relatively high.

These phenomena suggest a possible explanation for the decrease in the friction coefficient as the solid fraction increases. At low solid fraction, particles move more freely from one layer to another. Thus more particles in the upper layers with small values of $\omega r/u$ move down to the boundary and collide with the wall. Because friction is measured in a statistical sense as a sum of frictions due to individual particles colliding with the wall, f is therefore high at low solid fraction. On the other hand, at high solid fraction and low granular temperature, very few particles in the upper layer with low $\omega r/u$ penetrate to the wall. As

a result, particles next to the wall with high rotational velocity will dominate collisions at the wall. Thus f would be smaller at high solid fraction.

This explanation appears to be consistent with the data for the rubberized surface where no slip is expected (see Figure 3.14). The general trend of decreasing f with increasing ν holds independent of particle size. In Figure 3.15, f is plotted against u'_w/u_w. When higher u'_w/u_w exists, particles with low ω in the upper layer more easily move down to the boundary and collide with the wall. That is, as u'_w/u_w increases, the intrusion of particles with low ω from the upper layer into the boundary becomes more frequent, causing f to increase. As a result, the friction coefficient appears to be a fairly linear function of u'_w/u_w for the rubberized surface.

For the smooth and moderately smooth surfaces, slip occurs and μ_c controls the boundary conditions. Therefore, f is comparable to μ_c (see Figure 3.14), and f is unrelated to u'_w/u_w (see Figure 3.15). (However, one might argue from Figure 3.15 that for the smooth and moderately smooth surfaces f is small because u'_w/u_w is small. Then it may be concluded that regardless of the surface conditions f has a fairly linear relation to u'_w/u_w.)

3.4.3 Stresses and Rheological Behavior

In Figures 3.16 (a) and 3.17 (a), the experimental data are fairly well correlated when stresses are normalized following the rheological models by Lun *et al.* [1984]. The models should hold for any flow whether it is a fully developed flow or not. The data are also internally consistent, independent of the surface boundary conditions. However, when the stresses are normalized following the model for simple shear flow of Lun *et al.*, the experimental data show the dependency on the surface conditions, as presented in Figures 3.18 and 3.19. This may be because chute flows differ in many ways from simple shear flow.

The chute flows in the present experiments were not fully developed. This is confirmed by comparing friction coefficient with the tangent value of the chute inclination angle. The ratio of $\tan\theta$ to f is plotted in Figure 3.24. If flow is fully

developed, the ratio should be 1. The results show that most of the data do not correspond to fully developed flows. Therefore, when these data are presented in Figures 3.20 and 3.21 following the models for fully developed flow, considerable scatter is observed. However, some fully developed flows are obtained with the rubberized surface. With this idea in mind, shear stress normalized by $\rho_p(d\Delta u/h)^2/\tan\theta$ is plotted again in Figure 3.25 using only data for which $\tan\theta/f < 1.25$. Note that the normal stress normalized by $\rho_p(d\Delta u/h)^2/\tan^2\theta$ is in fact identical with the normalized shear stress in the case of $\tan\theta \simeq f$. The scatter shown in Figures 3.20 and 3.21 disappears from Figure 3.25, and all the data are rather well correlated. In Figure 3.26, $S/\tan\theta$ is plotted for only those data for which $\tan\theta/f < 1.25$. The data are again in good correlation contrary to the scatter found in Figure 3.23. The selected data also agree well with the rheological behavior suggested by Lun *et al.* [1984] (see equation (2.17)).

From investigations of various rheological models, it may be concluded that the rheological models for general flow (equations (2.8) and (2.9)) give good correlation to the present experimental data (see Figures 3.16 and 3.17). The rheological model for fully developed flow (equation (2.18) or (2.19)) is also confirmed by some selected experimental data which are close to fully developed flow (see Figure 3.25).

CHAPTER 4
ANALYSIS OF THE FULLY DEVELOPED CHUTE FLOW OF GRANULAR MATERIALS

4.1 FORMULATION OF THE BOUNDARY VALUE PROBLEM

In the present analysis of fully developed chute flow, the constitutive equations of Lun *et al.* [1984] for granular materials are used along with the basic equations of motions. As presented in chapter 2, the momentum equations and the translational fluctuation energy equation for fully developed chute flow are as follows:

$$\frac{\partial P_{yy}}{\partial y} = -\rho_p \nu g \cos\theta, \tag{4.1}$$

$$\frac{\partial P_{yx}}{\partial y} = \rho_p \nu g \sin\theta, \tag{4.2}$$

$$-P_{yx}\frac{\partial u}{\partial y} - \frac{\partial q_y}{\partial y} - \gamma = 0, \tag{4.3}$$

where θ is the angle of the chute inclination, and g is the gravitational acceleration. Note that for the fully developed chute flow $-P_{yx}/P_{yy} = \tan\theta$.

The constitutive equations of normal and shear stresses for fully developed chute flow are also presented in chapter 2 as

$$P_{yy} = \rho_p g_1 T, \tag{4.4}$$

$$P_{yx} = -\rho_p d g_2 \frac{\partial u}{\partial y} T^{\frac{1}{2}}, \tag{4.5}$$

and the y-component of fluctuation energy flux is

$$q_y = -\rho_p d\left(g_3 T^{\frac{1}{2}}\frac{\partial T}{\partial y} + g_4 T^{\frac{3}{2}}\frac{\partial \nu}{\partial y}\right). \tag{4.6}$$

The rate of dissipation per unit volume is given as

$$\gamma = \frac{\rho_p}{d} g_5 T^{\frac{3}{2}}. \tag{4.7}$$

In the above expressions, g_1, g_2, g_3, g_4, and g_5 are functions of ν and e_p as shown in chapter 2.

Equations (4.1)-(4.3) with (4.4)-(4.7), after nondimensionalization, can be written in the following form:

$$\frac{\partial \nu}{\partial y^*} = -\frac{1}{g_1' T^*}\left(\nu + g_1 \frac{\partial T^*}{\partial y^*}\right), \tag{4.8}$$

$$\begin{aligned}\frac{\partial^2 T^*}{\partial y^{*2}} = \frac{1}{g_1'^2(g_1 g_4 - g_1' g_3)}\Bigg[& T^* g_1'^3 \left\{\frac{g_1^2}{g_2}\tan^2\theta - g_5\right\} \\ & + \frac{1}{T^*}\left(\frac{\partial T^*}{\partial y^*}\right)^2 \left\{\frac{1}{2}g_1'^3 g_3 - g_1 g_1'^2 g_3' + \frac{1}{2}g_1 g_1'^2 g_4 + g_1^2 g_1' g_4' - g_1^2 g_1'' g_4\right\} \\ & + \frac{1}{T^*}\frac{\partial T^*}{\partial y^*}\left\{g_1 g_1' g_4 + (2 g_1 g_1' g_4' - 2 g_1 g_1'' g_4 - g_1'^2 g_3 + \frac{1}{2}g_1'^2 g_4)\nu\right\} \\ & + \frac{1}{T^*}\left\{g_1' g_4 \nu + (g_1' g_4' - g_1'' g_4)\nu^2\right\}\Bigg],\end{aligned} \tag{4.9}$$

$$\frac{\partial u^*}{\partial y^*} = \frac{g_1}{g_2} T^{*\frac{1}{2}} \tan\theta. \tag{4.10}$$

Here the dimensionless spatial coordinate y^*, granular temperature T^*, and mean velocity u^* are defined by:

$$y^* = \frac{y}{d},$$

$$T^* = \frac{T}{gd\cos\theta},$$

$$u^* = \frac{u}{\sqrt{gd\cos\theta}}.$$

And in g_1', g_3', g_4', and g_1'' the dashes denote differentiation with respect to ν. These differential equations are nonlinear, and must be solved simultaneously. Equations (4.8) and (4.9) can be solved for ν and T^*; u^* follows from equation (4.10). It is important to note that ν and T^* have solutions independent of u^*.

The above system of differential equations (4.8)-(4.10) requires boundary conditions both at the wall of the chute base and at the free surface. At the free surface, ν must vanish as y^* goes to infinity, and the energy flux, q_y, must be zero. When all the conditions are examined carefully, it is obvious that if $\partial T^*/\partial y^*$ vanishes at the free surface then all the other conditions are automatically satisfied. When this gradient of the granular temperature tends to zero at the free surface, the gradient of solid fraction is always negative, and thus

the solid fraction vanishes in an approximately exponential manner. Since the solid fraction vanishes at the free surface, the gradient of the solid fraction tends to zero. Therefore, the energy flux vanishes because both gradients of granular temperature and solid fraction vanish at the free surface. Note that the gradient of mean velocity also vanishes since the solid fraction tends to zero at the free surface. Therefore, all the stresses and their derivatives vanish as ν goes to zero, satisfying the momentum equations at the free surface. The energy equation is also satisfied since all three terms in the equation (4.3) vanish independently at the free surface.

Hence the boundary value problem is formulated as follows: The differential equations, (4.8), (4.9), and (4.10), are to be solved with three boundary values at the wall (ν, T^*, and u^* at $y^* = 0$), and one boundary condition at the free surface ($\partial T^*/\partial y^* = 0$ at $y^* = \infty$). A "shooting method" has been chosen to solve this boundary value problem. That is, for given ν, T^*, and u^* at the wall, a guess is made for the value of $\partial T^*/\partial y^*$ at $y^* = 0$. With these four values, the above differential equations are integrated from $y^* = 0$ to $y^* = \infty$. If $\partial T^*/\partial y^*$ at $y^* = \infty$ is not zero after integration, another $\partial T^*/\partial y^*$ at $y^* = 0$ is tried. This iterative procedure is continued until $\partial T^*/\partial y^*$ at $y^* = \infty$ becomes zero. In practice, iterations were done until the ratio of the temperature gradient at the free surface to that at the wall became about 10^{-6}, and the differential equations were for most cases integrated up to $y^* = 10 \sim 100$. A fourth order Runge-Kutta method was employed, and no convergence problems were encountered.

In order to check the above system of differential equations, an alternative way has been sought in appendix B. No difference was found between the results of the two methods.

The above boundary value problem has two parameters (e_p and $\tan\theta$) and three boundary values (ν, T^*, and u^*) at the wall. It is clear that the two parameters are physically appropriate. But the three boundary values at the wall may demand further physical interpretation. In a chute flow, the opening

of an entrance gate controls mass flow rate, $\dot{m}$, and the surface condition of the chute base provides two more physical constraints, namely, the wall-particle coefficient of restitution, e_w, and the roughness of the surface, δ. More generally the last two conditions may be considered as conditions governing the normal and tangential impulses experienced by particles when they collide with the wall.

The combination of the three conditions (such as $\dot{m}$, e_w, and δ) with the two parameters (e_p and $\tan\theta$) determines the three boundary values, ν, T^*, and u^* at the wall, and thus characterizes the entire flow. If a particular combination of ν, T^*, and u^* at the wall does not satisfy the wall boundary conditions, there may be a problem with the convergence of ν to zero at the free surface, implying that there is no realistic solution with those parameters and wall boundary values. Therefore, once ν, T^*, and u^* are properly chosen to satisfy the boundary conditions at the wall, all the free surface conditions are automatically satisfied.

It is noteworthy that the boundary conditions at the free surface are automatically satisfied in the present analysis. In other literature, there have been efforts to satisfy the free surface boundary conditions using various techniques. For example, Johnson and Jackson [1988] have attempted a numerical analysis similar to the present one. In their analysis the spatial coordinate, Y, was normalized by h, the depth of flow. Since h is not well defined, it was necessary to define a small layer adjacent to the free surface. The location of this layer was then defined as h, and a boundary value problem was solved between $Y = 0$ and $Y = h$. Later the results near $Y = h$ were matched to asymptotic low density solutions in the neighborhood of the free surface. The asymptotic solutions were obtained by demanding that the solid fraction and the derivatives of velocity and granular temperature vanish as $Y \to \infty$.

4.2 RESULTS OF ANALYSIS AND COMPARISONS

4.2.1 Results of Analysis

As described earlier, the flow properties, ν, T^*, and u^*, were obtained as

functions of y^*, the distance from the chute base normalized by the particle diameter. Each result was specified by the two parameters, e_p and $\tan\theta$, and three boundary values at the wall, ν_w, T_w^*, and u_w^*. The results for $\sqrt{T^*}$ and u^* were normalized by $\sqrt{T_w^*}$ and u_w^* respectively.

Though two parameters and three boundary values created numerous variations, the results could be classified into two distinct types and a transitional type according to the form of the granular temperature profile. The first type is illustrated by the solution shown in Figure 4.1 for which $e_p = 0.95$, $\tan\theta = 0.4$, $T^* = 2$, $\nu_w = 0.2$, and $u^* = 10$. Note that granular temperature increases with distance from the wall. The profile of solid fraction exhibits a monotonic decrease from the wall to the free surface, and it is clear that solid fraction vanishes at the free surface. The profile of mean velocity appears to be roughly parabolic. Near the wall the profile is fairly linear, and the velocity gradient tends to zero at the free surface. The physical location of the free surface, h, is ill-defined in view of the solid fraction profile. One might reach different conclusions about the value of h depending on whether the granular temperature or the velocity profile is being examined.

Obvious differences in the profile of the granular temperature occur for the second type illustrated in Figure 4.2 for which $e_p = 0.6$ and the other values remain unchanged. First of all, the temperature gradient is now negative. The variation of the magnitude of the temperature with distance from the chute base is substantial. The different choice of the value of the coefficient of restitution also results in a particular type of solid fraction profile, where the maximum solid fraction is achieved in the center of the flow and lower densities occur both at the wall and at the free surface. In this case, the free surface is more clearly defined.

Finally, a transitional type that contains features of both the first and second types is illustrated in Figure 4.3. Note that $e_p = 0.8$ and $\nu_w = 0.3$ while the other parameter and boundary values are not changed. The granular temperature first

increases with distance from the wall boundary, then decreases at larger distances from the wall, and then becomes uniform near the free surface. The profile of solid fraction is similar to that of the first type.

The question of when each of these types of granular temperature profiles occurs will be discussed later. In this presentation, the first, second, and last types will be referred to as Type I, Type II, and Type III, respectively.

The effect of the variation of the parameter $\tan\theta$ is investigated in Figure 4.4. The results show that higher gradients of granular temperature and velocity arise from a higher angle of chute inclination, and the depth of flow also increases. This is consistent with a physical understanding of the chute flow. That is, for a higher inclination angle, particles move faster and collide with greater impact, resulting in the increase of granular temperature and velocity gradient. The increase of the overall granular temperature causes dilatation near the wall, which is accompanied by an increase in the depth of flow. As a result, the solid fraction for the higher chute inclination is lower near the wall but higher at a distance from the wall.

The effect of the variation of boundary values at the wall is examined in Figures 4.5 and 4.6. Comparison shows that a larger value of granular temperature at the wall results in an increase in the granular temperature gradient and thus the overall granular temperature. As a consequence, (see equation (4.10)), the gradient of mean velocity also increases. The increase of granular temperature is also accompanied by an increase in the depth of flow. These results are consistent with the observation of the present experiments in chapter 3 (though the details are not included). On the surface where higher temperature is created, higher gradients of temperature and velocity are observed, and the depth of flow is increased.

The effect of the variation of solid fraction at the wall is examined in Figure 4.6. When a larger solid fraction is prescribed at the wall, the granular temperature, the depth of flow, and the mean velocity all increase significantly. These

results agree with the experimental observations. In order to have a high solid fraction at a given chute inclination, the mass flow rate needs to be large, and this implies a deeper flow.

4.2.2 Comparison with Experimental Results

Few experimental data are available for comparison with these analytical results. In particular, there are almost no measurements of granular temperature. Furthermore, the wall boundary conditions are not sufficiently well understood to allow us to estimate the values of T^*, ν, and u^* at the wall. The experiments of chapter 3 or Ahn *et al.* [1989a] represent an attempt to acquire the necessary data. In measurements through the sidewalls, the profiles of one component of granular temperature, mean velocity, and linear concentration were obtained. For comparison with the present results, granular temperature and solid fraction are obtained from one component of granular temperature, $\langle u'^2 \rangle$, and linear concentration, ν_{1D}, by taking $T = \langle u'^2 \rangle$ and $\nu = \pi \nu_{1D}^3/6$. Furthermore the value of $e_p = 0.95$ is appropriate for the glass beads used in the experiments (see Lun and Savage [1986]) and this value of e_p is employed in all the results presented.

In a strict sense the solid fraction goes to zero at the wall since the particles are spherical. As a result, the appropriate wall solid fraction to be used in the corresponding continuum model is rather unclear. Therefore two candidate choices are employed in the comparisons which follow. One is the solid fraction which was obtained at the measurement location closest to the wall. The other is the maximum solid fraction which was usually obtained at between a half and one particle diameter distance from the wall.

Experimental data in Figure 3.9 for 1.26 mm diameter glass beads flowing down a chute with a smooth aluminum surface are compared with the present analysis in Figure 4.7. The chute inclination angle θ was 22.7°, and the boundary values at the wall, $T_w^* = 0.935$ and $u_w^* = 11.3$ are taken from the experiments. Two wall solid fractions are used as described above, namely, 0.205 and 0.304.

The profile of granular temperature from the experiments shows a general increase of temperature with distance from the wall. This increasing feature is predicted by the present analysis. With $\nu_w = 0.205$, the magnitude of granular temperature is also well predicted. Moreover, the monotonic decrease of solid fraction with distance from the wall is consistent with the experiments. Near the wall, the result for the case of $\nu_w = 0.304$ shows better agreement with the experiments, but at the free surface the present analytical result deviates from the experiments. For $\nu_w = 0.205$, the depth of flow of the analysis is consistent with that of the experiments while there is slight discrepancy near the wall. In addition, good agreement is observed between the profiles of mean velocity for the case of $\nu_w = 0.205$.

For the second comparison, experimental data in Figure 3.8 with a rubber-coated chute base are presented again in Figure 4.8. This rubber-coated surface created quite different boundary conditions; compared to a smooth aluminum surface, the depth of flow was high, mean velocity was usually low, and both the gradients of mean velocity and granular temperature were high. In the experiments, the 3.04 mm glass beads were used, and the chute inclination angle was 22.7°. Boundary values at the wall, $T_w^* = 0.44$ and $u_w^* = 4.388$ are taken from the experiments, and $\nu_w = 0.179$ and $\nu_w = 0.244$ are chosen as alternative solid fractions at the wall. Considerable discrepancy is observed between the profiles of granular temperature. The present analysis yields almost uniform granular temperature while the experimental data display significant granular conduction from the free surface to the wall. On the other hand, a remarkable agreement is found in the profiles of solid fraction, especially in the case of $\nu_w = 0.244$. The depth of flow as well as the general shape of solid fraction profile is well predicted in the present analysis. In the profiles of mean velocity, a deviation of the analysis from the experimental data is found. The discrepancies found in the profiles of granular temperature and mean velocity could be a result of the experimental flow not being fully developed. One might surmise that this

flow would obtain a higher granular temperature as it became fully developed. If a larger value of T_w^* is input to the present analysis, considerable increases of granular temperature and mean velocity result (as shown in Figure 4.5).

4.2.3 Comparison with Computer Simulation

Comparison of the present analysis can also be made with the computer simulations of Campbell and Brennen [1985b]. The results of Campbell and Brennen for $\theta = 30°$ or $\tan\theta = 0.577$, $e_p = 0.6$, and $e_w = 0.8$ and their Type A boundary condition are presented in Figure 4.9. The results with two-dimensional disks were converted into three-dimensional values by taking $\nu = 4\nu_{2D}^{\frac{3}{2}}/3\sqrt{\pi}$ and $T = \frac{1}{2}(\langle u'^2\rangle + \langle v'^2\rangle)$. The boundary values were $T_w^* = 7$, $u_w^* = 14$, and $\nu_w = 0.14$. The results of the present analysis with these parameters and boundary values are shown in Figure 4.9. When $\tan\theta = 0.577$ is used as a parameter in the analysis, a fundamental difference is found. The results of Campbell and Brennen are of Type II while the present analysis yields a Type III flow. However, when $\tan\theta = 0.45$ is used for the analysis, comparison shows excellent agreement between the analysis and the computer simulation. Both profiles of granular temperature have negative gradients, and their magnitudes are also in good agreement. The profiles of solid fraction are qualitatively similar, and the depth of flow is also well predicted. A discrepancy in the magnitude of solid fraction may arise from the fact that the computer simulations were done with two-dimensional disks. In the case of $\tan\theta = 0.45$, the mean velocity profiles also show good agreement between the computer simulation and the present analysis.

In short, good agreement is achieved in the case of $\tan\theta = 0.45$, which is slightly different from the value of the computer simulation. This may imply that the present analysis confirms the possibility of the existence of Type II flow but does not accurately predict when that type of flow takes place.

The results of Campbell and Brennen's computer simulations at the small chute angle of $\theta = 20°$ could not be reproduced by the present analysis. The analysis yielded a Type II temperature profile while the computer simulations

produced a type of plug flow. That is, the minimum granular temperature was achieved in the center of the flow, and higher temperature occurred both at the wall and at the free surface. The solid fraction profile of the analysis was similar to Type I while the computer simulation result had the profile of Type II.

Comparisons of the present analysis with experiments and computer simulations lead to the following conclusions. The experimental data are similar to Type I flow in which a positive temperature gradient and monotonically decreasing solid fraction are observed. The present analysis also produces the results of Type I as long as the boundary values are properly chosen. The general profiles of flow properties are well predicted though some discrepancies in their magnitudes are observed. On the other hand, the computer simulations have Type II flows for sufficiently high chute inclinations. The granular temperature decreases with distance from the wall, and the solid fraction increases near the wall and decreases with further distance from the wall. These results can also be produced by the present analysis when a slight change in the parameter $\tan\theta$ is made.

The fundamental difference between the experimental results and the computer simulations is the value of the coefficient of restitution ($e_p = 0.95$ for the experiments and $e_p = 0.6$ for the computer simulations). The different values of e_p result in Type I flow for the experiments and in Type II flow for the computer simulations. This will be discussed further in the next section.

4.3 THE NATURE OF GRANULAR CONDUCTION

For fully developed chute flows, the translational fluctuation energy equation (4.3) may be written as follows:

$$W + Q - \gamma = 0$$

where W is the rate of the work done by stresses to the system per unit volume, Q is the rate of the fluctuation energy added to the system per unit volume through the conduction of granular temperature, and γ is the dissipation rate

per unit volume. For a simple shear flow, the conduction term disappears from the energy equation. But for chute flows the role of the conduction term or its magnitude compared to other terms has never been clear. In this section the fundamental nature of the conduction term will be discussed.

Equation (2.17) makes it possible to evaluate the work done by shear stress, and thus all the terms in the fluctuation energy equation are given as follows:

$$W^* = \frac{{g_1}^2}{g_2} T^{*\frac{1}{2}} \tan^2\theta,$$
$$\gamma^* = g_5 T^{*\frac{3}{2}},$$
$$Q^* = \gamma^* - W^*,$$

where W^*, γ^*, and Q^* are shear work term, dissipation term, and granular conduction term nondimensionalized by $\rho_p(gd\cos\theta)^{\frac{3}{2}}/d$. Furthermore, it is recalled that

$$Q^* = -\frac{\partial q^*}{\partial y^*},$$

where q^*, the fluctuation energy flux nondimensionalized by $\rho_p(gd\cos\theta)^{\frac{3}{2}}$, is given as

$$q^* = -(g_3 T^{*\frac{1}{2}} \frac{\partial T^*}{\partial y^*} + g_4 T^{*\frac{3}{2}} \frac{\partial \nu}{\partial y^*}).$$

It can be noted from the constitutive equations that γ^* is quite sensitive to the value of e_p while W^* is less sensitive, and that γ^* vanishes as e_p approaches 1. Therefore, for large e_p (e.g., 0.95) W^* is larger than γ^*, and this results in a negative value of Q^*. The opposite is true for small e_p such as 0.6. For a positive Q^*, the gradient of q^* is negative, and a positive gradient of q^* is achieved for negative Q^*. But the boundary condition at the free surface requires that $q^* \to 0$ as $y^* \to \infty$. Consequently, for a fixed ν, a negative value of q^* is obtained for all y^* in the case of a positive gradient of q^*, and a positive value of q^* in the case of a negative gradient of q^*. In other words, for a sufficiently large e_p, a negative energy flux, q^*, is achieved along with a negative granular conduction term, Q^*. And for a sufficiently small e_p, a positive Q^* results in a positive energy flux.

As ν varies over the depth of the flow, however, the above argument may need modification. The effects of ν and $\tan\theta$ on the conduction term can be examined along with the effect of e_p as follows. The zero of Q^* is found by examining the following equation for Q^*:

$$Q^* = \left(g_5 - \frac{{g_1}^2}{g_2}\tan^2\theta\right)T^{*\frac{1}{2}} = 0.$$

This is solved as shown in Figure 4.10. Each curve represents zeros of Q^* for a given e_p. If $\tan\theta$ is greater than the value on the curve for a given ν, negative values of Q^* are obtained, and if $\tan\theta$ is smaller, then $Q^* > 0$. For example, for $\tan\theta = 0.4$, negative values of Q^* result for all ν in the case of $e_p = 0.95$, but positive values result in the case of $e_p = 0.6$.

The effects of e_p, ν, and $\tan\theta$ on the conduction term, were examined in detail for solutions of Type I, Type II, and Type III flows. The energy flux, q^*, and the conduction term, Q^*, are plotted in Figures 4.11 (a), (b), and (c) with the same parameters and boundary values as given in Figures 4.1, 4.2, and 4.3 respectively. As expected from the results of Figure 4.10 in the case of $e_p = 0.95$ and $\tan\theta = 0.4$, negative Q^* is achieved in Figure 4.11 (a) and thus negative q^*. But for $e_p = 0.6$ and $\tan\theta = 0.4$ in Figure 4.11 (b), positive Q^* and q^* emerge, which are in accordance with the results of Figure 4.10. When q^* is negative at the wall boundary, it means that the wall absorbs the fluctuation energy. For this case, the granular temperature is expected to be low near the wall while high temperature is exhibited at the free surface, and thus the fluctuation energy is conducted from the free surface to the wall. The generation of fluctuation energy through shear motion feeds fluctuation energy into the bulk, where it is partly absorbed at the wall boundary and partly dissipated away. On the other hand, positive fluctuation energy flux at the wall implies that the wall should supply energy to the flow. Unless energy is provided to granular materials through the wall (for example, by vibrating the chute base), there can be no such positive fluctuation energy flux and therefore no such flow. (Note that changes to granular material flows wrought by vibration are well known in industrial practice.) In the

experiments of chapter 3, when the angle of the chute inclination was less than about 12°, there was no flow unless the chute was agitated. This is consistent with the results of Figure 4.10 in which the zero of Q^* for $e_p = 0.95$ is achieved at $\tan\theta \simeq 0.22$.

With this idea in mind, it is interesting to study a hypothetical experiment in which there is no shear motion but granular materials are allowed to have granular temperature which might be supplied by wall vibration. Then fluctuation energy will be conducted from the wall and should be dissipated inside the bulk. Now let us examine such a state using the present analysis. The mean velocity and its gradient are zero, and $\tan\theta = 0$. From Figure 4.10, it is expected that the conduction term will be positive for all values of the coefficient of restitution. The solutions are illustrated in Figure 4.12, in which $e_p = 0.9$ and 0.95, $\tan\theta = 0$, $\nu_w = 0.2$, and $T_w^* = 5$. As expected, the solutions are of Type II because of a positive conduction term. Temperature decreases with distance from the wall, and solid fraction increases near the wall but decreases with further distance from the wall. Comparison between the results for different values of e_p show, as expected, that for low e_p the fluctuation energy dissipates faster than for high e_p. Therefore, the case of the lower e_p results in a lower temperature at the free surface.

At this point, it is necessary to study how solid fraction varies with granular temperature. Physically it is clear that it is difficult for particles to stay close in the presence of high temperature. Therefore, when the temperature is high, the solid fraction is low. The variation of solid fraction with granular temperature can be explained in more detail by using equation (4.8):

$$\frac{\partial \nu}{\partial y^*} = -\frac{1}{g_1' T^*}\left(\nu + g_1 \frac{\partial T^*}{\partial y^*}\right).$$

When the temperature gradient is negative, the solid fraction gradient can be positive since both g_1 and g_1' are always positive. Therefore, when the temperature decreases significantly with distance from the wall, the solid fraction increases near the wall as shown in Figures 4.2 and 4.12. Furthermore, when

the temperature is lower, the magnitude of the solid fraction gradient is higher. Hence the solid fraction for $e_p = 0.9$ increases more than for $e_p = 0.95$ as shown in Figure 4.12. The equation (4.8) also explains the variation of solid fraction near the free surface. Near the free surface, g_1' tends to 1, g_1 is the same order as ν, and the temperature gradient is negligible. Therefore, ν decreases approximately as e^{-y^*/T^*}. When the temperature is low at the free surface, a rapid decrease of solid fraction occurs. Therefore, the free surface is clearly defined as shown in Figure 4.2. On the other hand, when the temperature is high near the free surface, the solid fraction decreases slowly with distance, resulting in the case of Figure 4.1. These phenomena can also be observed from Figure 4.12 where lower T^* at the free surface results in a sharper decrease of ν (see the case of $e_p = 0.9$).

Figure 4.11 (c) is an interesting case for which q^* and Q^* start with negative values but become positive and tend to zero as the free surface is approached. The boundary values at the wall ($\nu = 0.3$) and the two parameters ($e_p = 0.8$ and $\tan\theta = 0.4$) give a negative value of Q^* from Figure 4.10. As ν decreases from the wall to the free surface, a positive Q^* is to be obtained from Figure 4.10. This particular profile of energy flux over the depth gives rise to the particular shape of temperature profile in Figure 4.3. Note from Figure 4.11 (c) that a local maximum of q^* is achieved when $Q^* = 0$.

The fundamental question of the magnitude of conduction term in the chute flow is answered in Figure 4.13 where the ratio of the conduction term to the dissipation term is plotted against y^*. Figures 4.13 (a), (b), and (c) are the results from cases of Figures 4.1, 4.2, and 4.3 respectively. In none of Figures 4.13 (a) and (b) is the conduction term insignificant relative to the dissipation term. In a transitional case such as Figure 4.13 (c), the conduction term is relatively smaller than the dissipation term. In fact, the ratio of the conduction term to the dissipation term is given as follows:

$$\frac{Q^*}{\gamma^*} = 1 - \frac{{g_1}^2}{g_2 g_5} \tan^2\theta.$$

In Figure 4.14, ${g_1}^2/g_2g_5$ normalized by the value at $\nu = 0$ is plotted as a function of ν and e_p. Note that ${g_1}^2/g_2g_5$ at $\nu = 0$ is given as follows:

$$\left(\frac{{g_1}^2}{g_2g_5}\right)_{\nu=0} = \frac{2}{5}\left(\frac{3-e_p}{1-e_p}\right).$$

Therefore, Q^*/γ^* varies from 1 (when $\theta = 0$) to $-\infty$ (when $e_p = 1$), and conduction is always important. In general, the magnitude of the ratio is large for large e_p, and small for small e_p. When negative conduction exists, a higher chute inclination yields a larger value for the ratio. That is, for a higher chute inclination, the conduction term plays a more important role relative to the dissipation term than for a lower chute inclination. When the conduction is positive, the opposite is true.

Since $W^*/\gamma^* = 1 - Q^*/\gamma^*$, the shear work term is small compared to the dissipation term when the conduction term is positive. When the conduction term is negative, W^*/γ^* is relatively large. (Note the comparison between Figures 4.13 (a) and (b).) When W^*/γ^* is small (such as in Figure 4.13 (b)), granular temperature is low because fluctuation energy is slowly generated by the shear work. Furthermore, the flow dissipates well because of a low coefficient of restitution. As a result, the high density at the center of the flow is not dilated as shown in Figure 4.2.

CHAPTER 5
EXPERIMENTAL STUDY OF HEAT TRANSFER TO GRANULAR FLOWS

5.1 APPARATUS AND PROCEDURE

Convective heat transfer to granular material flowing down an inclined chute has been studied experimentally. Since this experimental program was conducted during the early stages of the entire research, the experimental facilities and instruments were relatively simple compared to those for the experiments on shear flows of granular materials.

In general, the basic design of the overall experimental setup was similar to that of Spelt [1981]. A hopper with about 100 liter capacity was installed on the top of the hopper stand, and from the hopper granular materials were discharged into the chute. At the exit of the chute the discharging materials were collected using a container. The granular materials in the container were manually fed back into the hopper. The chute was pivoted at the middle of the hopper stand, and was supported by a bar which was in turn supported by two cantilevered support arms extending from the hopper stand. The angle of the chute inclination was adjusted by changing the location of the bar along the support arms. The dimensions of the chute were the same as those in the shear flow experiment; 7.62 cm wide and 1.2 m long.

The previous works (Spelt [1981] and Patton [1985]) had indicated that the electrostatic charge within flowing granular materials could be a problem affecting the reproducibility of results. Indeed, the buildup of static charge was observed in the present experiments with the small 0.50 mm glass beads. (However, the buildup was insignificant with the other materials of larger particle diameters.) Therefore, all the parts of the chute were made of aluminum, and the whole experimental setup was electrically grounded in order to minimize the effect of electrostatic charge.

The test section consisted of a heating plate; 5.1 cm wide and 15.2 cm long. A rectangular hole, 6.3 cm wide and 17.2 cm long, was cut into the chute base and replaced by the heating plate. The heating plate comprised a copper plate, a heating element, a phenolic plate, and a guard heating element, which were glued together on the top of each other using an epoxy with a high thermal conductivity. (See Figure 5.1.) In order to create constant temperature condition at the wall, copper was chosen as the top portion of the heating plate because of its high thermal conductivity. Under the copper plate was a 50 W ribbon heater manufactured by Sierracin/Thermal Systems. The electrical resistance of the heater was measured, and thus the power output of the heater was calculated reading the voltage across the heater. The variation of the resistance with temperature appeared to be insignificant, and it was neglected in calculating the power output.

The phenolic plate and the guard heater were used to insulate the bottom of the heater under the copper plate. Once the power output of the top heater was selected so as to yield a reasonable temperature difference between the flowing material and the copper plate, the temperature under the phenolic plate was adjusted by the guard heater. By adjusting two temperatures on the top and bottom of the phenolic plate to be close to each other, the heat transfer across the phenolic plate was minimized, and most of the heat generated by the top heater could be assumed to be convected to the flowing granular material. The top and guard heaters were identical, and their powers were independently controlled by two 120 V A.C. variable autotransformers. The thicknesses of the copper and phenolic plates were 1.2 mm and 6.4 mm respectively.

The heating plate was installed with four setscrews in the holes at the chute base. The gap between the heat plate and the chute base was filled first with styrofoam and then with the product "Bond-O" (a bonding resin) as shown in Figure 5.1. The bonding resin allowed a smooth transition from the chute base to the heating plate, eliminating possible flow disturbance due to the gap.

All the temperatures were measured using 0.13 mm thick Type K chromel-alumel thermocouples. These thermocouples were all connected to a rotary switch mounted in an insulated box. The thermocouple voltages, which were read with a microvoltmeter, were converted into temperature using the following calibration curve:

$$\Theta = -0.270 + 0.02984 \times V^{0.976},$$

where Θ is temperature in °C, and V is the thermocouple voltage in microvolts. The above curve was obtained from the table of National Bureau of Standards over the temperature range of $10° \sim 60°$C.

The temperature of the upstream flow was measured with a thermocouple which was glued in between two small pieces of copper. This thermocouple was located in a small reservoir between the hopper and the entrance gate.

Nine thermocouples were placed under the copper plate in order to obtain the average temperature of the copper plate. The thermocouples on the copper plate were of the series-junction type. The chromel and alumel wires were separately welded to the bottom of the copper plate. This ensured that the thermocouples were in good contact with the copper plate, so that they would read the accurate temperature of the copper plate. If a thermocouple were in bad contact with the copper plate, a voltage across the thermocouple would appear clearly erroneous.

In addition to the thermocouples on the copper plate, three thermocouples were located on each side of the phenolic plate. Ideally the two temperatures on the top and bottom of the phenolic plate were to be the same by adjusting the power output of the guard heater. However, since in fact there was always a slight temperature difference, the heat flux across the phenolic plate had to be calculated. In most cases, the temperature difference was controlled to be less than 0.2 °C, and the heat flux through the phenolic plate was much less than 1% of the heat convected to the flow. The thermal conductivity of the phenolic plate was measured to be about 0.3 W/m · °C.

In order to estimate heat loss through the styrofoam and the "Bond-O" in the gap between the heating plate and the chute base, three thermocouples were located in the chute base outside the gap and opposite the heating plate. The exact locations are shown in Figure 5.1. The heat loss coefficient through the gap was calibrated in the following way: The copper plate was covered with a 5 cm thick styrofoam. The average temperature of the copper plate was measured. The maximum heat loss through the styrofoam insulator was estimated by considering the thermal conductivity of styrofoam, the thickness and area of the styrofoam, and the temperature difference between the copper plate and the room. The heat loss through the insulator appeared to be no more than 10% of the total heat generation during this calibration. Heat loss through the phenolic plate was also estimated by measuring temperature difference across the phenolic plate. Therefore, the net heat flux through the gap was calculated from the total heat generation less the heat losses through the styrofoam insulator and the phenolic plate. The average temperature difference across the gap was also measured. Thus the heat loss coefficient through the gap was calibrated with $\pm 5\%$ repeatability and found to be 0.11 W/°C. During the experiments, the total heat loss through the gap was usually less than 10% of the heat convected to the flow, but in some cases it reached up to about 20%.

The depth of flow was measured at two locations upstream and downstream of the heating plate. The techniques of measuring the depth of flow and mass flow rate were the same as those of the shear flow experiment. Since the use of the fibre optic probes had not been developed when this heat transfer experiment was conducted, measurements of velocity and solid fraction were made using the techniques developed by Patton [1985]. Once the flow reached a steady state, two parallel plates were pushed into the flow. The material trapped between the two plates was carefully collected and measured. The mean solid fraction, ν_m, was then determined as

$$\nu_m = \frac{M}{\rho_p b h L},$$

where M is the mass of the material captured between the plates, ρ_p the density of the solid particle, b the width of the chute, h the depth of flow, and L the distance between the plates. From the mean solid fraction and mass flow rate, the mean velocity over the depth of flow was obtained. After the use of fibre optic probes was developed, this method was compared with the technique using the fibre optic probes. The results were similar when the flows were slow. However, as the flow velocity increased, the discrepancy between two methods became larger; the method using two plates always yielded higher mean solid fraction, in some cases, by as much as 35%. This discrepancy is probably caused by the difficulty of inserting the parallel plate and the inaccuracy of this procedure, particularly at high velocity.

In order to obtain very slow flows with high solid fraction, an aluminum plate was clamped over the end of the chute. This plate formed a weir over or under which granular material had to flow. If a Froude number is defined as $\mathrm{Fr} = U/\sqrt{gh\cos\theta}$ (where U is the mean velocity, g the gravitational acceleration, h the depth of flow, and θ the angle of the chute inclination), then these very slow flows are all subcritical in the sense that Fr is less than 1.

The experiments were conducted with three different sizes of glass beads (0.50 mm, 1.26 mm, and 3.04 mm) in order to examine the effect of particle size. In addition, 3.15 mm polystyrene beads and 2.22 mm mustard seeds were also used because their thermal properties and densities are quite different from those of glass beads. Measurements of the thermal conductivity and diffusivity of each material were made and the details are included in appendix C. Specific heat capacity was calculated from the density, the thermal conductivity, and the thermal diffusivity. All these are listed in Table 1. Most values are in good agreement with those measured by Sullivan [1973].

The procedure used to acquire the heat transfer data was as follows. First, the angle of chute inclination and the entrance gate opening were set. As a flow was established, the power output of the top heater was adjusted to yield a

reasonable temperature difference between the flowing materials and the copper plate. Then the power output of the guard heater was adjusted with great care to make the temperature difference across the phenolic plate as small as possible. The temperature difference between the flow and the copper plate was usually about 20°C, and the temperature difference across the phenolic plate was less than 0.2°C. When a steady state was achieved, the mass flow rate and the depth of flow were measured. Following this, all the temperatures were quickly recorded. Finally, the mean solid fraction was measured. The whole procedure took 15 $\sim$ 25 minutes.

5.2 PRESENTATION OF EXPERIMENTAL DATA

Granular flow in an inclined chute shares some of the characteristics of the open channel flow of liquids. When a flow is in a subcritical regime, it is dependent on the downstream conditions. The flow is slow and characterized by high solid fraction. On the other hand, a supercritical flow has a relatively low solid fraction, and the granular material flows rapidly down the chute. The variation of solid fraction with Froude number is shown in Figure 5.2. In the subcritical regime (Fr $<$ 1), the solid fraction shows little variation with Froude number, and its value is about 0.6. But when flows are in the supercritical regime (Fr $>$ 1), the solid fraction varies substantially with Froude number.

The heat transfer to granular flows is also characterized by the two flow regimes as shown in Figure 5.3. In the subcritical regime, the heat transfer rate increases with increasing Froude number. For each granular material, the maximum heat transfer rate occurs just before the flow changes into a supercritical flow. But once the flow becomes supercritical, the heat transfer rate decreases with increasing Froude number in spite of the increase of velocity. This is because the decrease of solid fraction with Froude number causes the heat transfer rate to decrease. It should also be noted that the smaller the particle diameter, the larger the heat transfer coefficient.

Following the works of Sullivan and Sabersky [1975] and Patton *et al.* [1986], the present data are plotted in terms of the modified Nusselt number, Nu^*, and the modified Peclet number, Pe^*, where

$$Nu^* = \frac{hd}{k_g}, \tag{5.1}$$

$$Pe^* = \frac{UL}{\alpha_c}\left(\frac{d}{L}\right)^2\left(\frac{k_c}{k_g}\right)^2. \tag{5.2}$$

In the above, h is the convection heat transfer coefficient, d the particle diameter, L the length of the heating plate, U the mean velocity. And k_g is the thermal conductivity of gas, and k_c and α_c are the thermal conductivity and diffusivity of the granular material measured at the critical solid fraction. Note that air was used as the interstitial gas in all of the present experiments. In Figure 5.4, for a given material, Nu^* increases with increasing Pe^*, and after it reaches a maximum, Nu^* decreases with further increase in Pe^*. This phenomenon is closely associated with that of Figure 5.3, in that the data for increasing Nu^* with increasing Pe^* correspond to the subcritical flow, and the data for decreasing Nu^* with high Pe^* are in the supercritical regime. In other words, the heat transfer rate increases with increasing velocity since the solid fraction remains near the critical solid fraction. Once the flows become supercritical, Nu^* decreases because of the decrease of solid fraction as Pe^* increases. All the granular materials show similar trends, and all the data in the subcritical regime form a single curve regardless of particle size or material. This is the same phenomenon observed by Patton *et al.* [1986], and the single curve has been predicted from the model developed by Sullivan and Sabersky [1975]:

$$Nu^* = \frac{1}{\chi + \frac{\sqrt{\pi}}{2}\sqrt{\frac{1}{Pe^*}}}, \tag{5.3}$$

where χ is an experimental constant. For the present data $\chi = 0.025$ is chosen while Sullivan and Sabersky used $\chi = 0.085$. In Figure 5.4, the equation (5.3) with $\chi = 0.025$ is also presented.

The above model of Sullivan and Sabersky predicts the data quite satisfactorily in the subcritical regime where granular materials flow slowly with high solid fraction, but it fails to predict the behavior of the heat transfer as the flow becomes supercritical. This incompleteness of the model leads to the introduction of two new parameters; the effective Nusselt number, $\mathrm{Nu}^*_{\mathrm{eff}}$, and the effective Peclet number, $\mathrm{Pe}^*_{\mathrm{eff}}$.

The effective Nusselt number and the effective Peclet number are defined as follows:

$$\mathrm{Nu}^*_{\mathrm{eff}} = \mathrm{Nu}^* \frac{k_c}{k_e}, \tag{5.4}$$

$$\mathrm{Pe}^*_{\mathrm{eff}} = \mathrm{Pe}^* \frac{\alpha_c}{\alpha_e} \left(\frac{k_e}{k_c}\right)^2, \tag{5.5}$$

where k_e and α_e are the effective thermal conductivity and diffusivity of granular materials at a given mean solid fraction. The effective thermal conductivity is obtained from the results of Gelperin and Einstein [1971] as follows:

$$\frac{k_e}{k_g} = 1 + \frac{\nu(1 - k_g/k_s)}{k_g/k_s + 0.28(1-\nu)^{0.63(k_g/k_s)^{-0.18}}}, \tag{5.6}$$

where ν is the solid fraction, and k_g/k_s is the ratio of the thermal conductivity of gas to the thermal conductivity of the solid particle. The effective thermal diffusivity is obtained as

$$\alpha_e = \frac{k_e}{\rho_p \nu c_p},$$

where ρ_p is the particle density, and c_p is the specific heat capacity of the solid particle. The effective Nusselt number and the effective Peclet number simply take into account the variation of solid fraction which was neglected in the Sullivan and Sabersky formula. Note that when the mean solid fraction is equal to the critical solid fraction, the effective Nusselt and Peclet numbers are identical with the modified Nusselt and Peclet numbers.

The data for glass beads are plotted in Figure 5.5 using the effective coordinates. All the data points follow the shape of a single curve fairly well regardless of the flow regime. This may be explained by considering that when the effective

thermal conductivity and diffusivity are used for the data with solid fraction less than the critical value, the effective Nusselt number becomes larger than the modified one, and the effective Peclet number becomes smaller. As a result, the data in the supercritical regime in Figure 5.4 are shifted to the predicted curve for the subcritical regime. Therefore, when the effective Nusselt number and the effective Peclet number are introduced, all the data in both flow regimes can be represented reasonably well by a single equation which is of the same form as that developed by Sullivan and Sabersky (equation (5.3)). The following expression using the effective Nusselt and Peclet numbers is plotted in Figure 5.5.

$$\mathrm{Nu}^*_{\mathrm{eff}} = \frac{1}{\chi + \frac{\sqrt{\pi}}{2}\sqrt{\frac{1}{\mathrm{Pe}^*_{\mathrm{eff}}}}}, \tag{5.7}$$

where the value for χ is chosen as 0.025.

The data with materials different from glass beads are also plotted in Figure 5.6. The data for polystyrene beads and mustard seeds in the subcritical regime are well correlated with glass beads. But the data for polystyrene beads and mustard seeds in the supercritical regime are deviated from equation (5.7) for reasons that are not yet fully understood.

5.3 DISCUSSION

The necessity of introducing the effective Nusselt number and the effective Peclet number is associated with the fact that granular flow is a compressible flow. This calls for modifications to the previous Nusselt number and Peclet number of Sullivan and Sabersky (equations (5.1) and (5.2)) which were used for fairly constant high density flows. The new parameters should include density-dependent terms which can account for any kind of flow with various solid fractions. In the present work, the effective Nusselt number and the effective Peclet number have been defined using the effective thermal conductivity and diffusivity which vary with the density of the granular medium. This has made it possible to predict the rate of heat transfer to various flows using the single expression (5.7). The

effective parameter system unifies both subcritical and supercritical flow regimes with a single equation. Therefore, once the velocity and mean solid fraction of a flow are measured along with information on the properties of the granular medium, the heat transfer rate can be determined by equation (5.7) provided the experimental constant χ is known. In this section, the nature of χ and the physical meaning of equation (5.7) will be discussed.

The nature of the constant χ has been investigated by several authors. Sullivan [1973] and Sullivan and Sabersky [1975] introduced the thermal conductance between particles and the wall (or the wall-particle heat transfer coefficient, h_{wp}). They postulated that the wall-particle heat transfer coefficient be proportional to the conductivity of the interstitial gas k_g, and to the inverse of the particle characteristic length d (or the particle diameter). Therefore, the dimensionless proportionality constant χ was defined as $\chi = h_{wp}d/k_g$. They also suggested that χ should vary with changes in the local geometrical arrangement of particles near the wall. That is, a different wall surface condition such as the roughness of the wall or a different shape of particles would change the value for χ.

Schlünder [1980, 1984] also developed an expression for h_{wp}, namely,

$$h_{wp} = \phi_A \frac{4k_g}{d}\left[\left(1 + \frac{2l + 2\delta}{d}\right)\ln\left(1 + \frac{d}{2l + 2\delta}\right) - 1\right], \tag{5.8}$$

where ϕ_A is the surface coverage factor, l is the modified mean free path of gas molecules, and δ is the roughness of the surfaces. The surface coverage factor has a value of about 0.85 at the critical solid fraction. The value for l is given as 1.7×10^{-7} m by Schlünder or 2.7×10^{-7} m by Martin [1984] for air at 1 atm and 300° K. The equation (5.8) was obtained integrating the local conduction flux across the gas-filled gap between a sphere and a plane at a point contact.

The results of both Sullivan and Sabersky [1975] and Schlünder [1984] indicate that h_{wp} is proportional to the reciprocal of the particle diameter. This implies that the smaller the particle diameter, the larger the total convection heat transfer coefficient. This relation between the diameter and the heat transfer rate is supported to some extent by Figure 5.3 in which the heat transfer rate

is larger for the smaller particles.

The results of Schlünder suggest that χ should not be constant but rather given as

$$\chi = 4\phi_A \left[\left(1 + \frac{2l + 2\delta}{d} \right) \ln\left(1 + \frac{d}{2l + 2\delta} \right) - 1 \right]. \tag{5.9}$$

It states that χ is a function of d and δ as well as ϕ_A. The surface coverage factor ϕ_A, which is defined as the area on the wall surface projected by particles per unit area, must vary with solid fraction. Furthermore, for rapid flows with low solid fraction, particles are not in constant contact with the wall surface, and the distance between the particles and the wall serves as the roughness δ, changing the value for χ. Hence it is clear that the value of χ should be dependent on the solid fraction ν. Therefore, in what follows, χ and h_{wp} will denote the constant values at the critical solid fraction which characterizes subcritical flows, and h_{wp}^{ν} will be used for the density-dependent quantity at various ν.

Following the procedure of Schlünder [1984], a modified model can be developed in which the contact resistance at the wall and the heat penetration resistance of the bulk are density-dependent. For the contact resistance, h_{wp}^{ν} will be used instead of h_{wp}. In the term for the heat penetration resistance, $\mathrm{Pe}_{\mathrm{eff}}^{*}$ will be used in place of Pe^{*}. Then the equation (5.3) of Sullivan and Sabersky, which is virtually the same as that of Schlünder, becomes

$$\frac{hd}{k_g} = \frac{1}{\dfrac{k_g}{h_{wp}^{\nu} d} + \dfrac{\sqrt{\pi}}{2}\sqrt{\dfrac{1}{\mathrm{Pe}_{\mathrm{eff}}^{*}}}}.$$

This expression is not directly useful because it is almost impossible to estimate h_{wp}^{ν} with the present knowledge. After slight manipulation, the above equation can be arranged as

$$\frac{hd}{k_g} \frac{1}{1 - \dfrac{h}{h_{wp}^{\nu}} + \dfrac{h}{h_{wp}}} = \frac{1}{\dfrac{k_g}{h_{wp} d} + \dfrac{\sqrt{\pi}}{2}\sqrt{\dfrac{1}{\mathrm{Pe}_{\mathrm{eff}}^{*}}}}. \tag{5.10}$$

Note that equation (5.10) is identical to equation (5.3) when ν becomes the critical solid fraction. For solid fraction much less than the critical solid fraction,

the following assumptions are made:

$$\frac{h}{h_{wp}^{\nu}} \sim 1 \quad \text{and} \quad \frac{h}{h_{wp}} \sim \frac{k_e}{k_c}.$$

Then the right-hand side of equation (5.10) becomes $\mathrm{Nu}_{\mathrm{eff}}^{*}$ and thus the whole equation becomes identical to equation (5.7).

The first approximation, $h \sim h_{wp}^{\nu}$, comes from the assumption that, for low solid fraction, the contact resistance at the wall is much larger than the heat penetration resistance in the bulk and thus plays a more important role in determining the overall heat transfer coefficient. The breakdown of this assumption may occur either when the particle diameter is small and thus the contact resistance at the wall becomes small (see equation (5.8)), or when the thermal conductivity of the material is low and thus the heat penetration resistance becomes large. In either case, the contact resistance at the wall is comparable to the heat penetration resistance, and the approximation of $h \sim h_{wp}^{\nu}$ is not valid. The second approximation may be explained as follows: First of all,

$$\frac{h}{h_{wp}} = \frac{h_{wp}^{\nu}}{h_{wp}} \frac{h}{h_{wp}^{\nu}}.$$

Note that the first approximation, $h/h_{wp}^{\nu} \sim 1$, can be used again. Furthermore, since the difference between h_{wp} and h_{wp}^{ν} comes from the increasing spacing between the wall and particles due to the decrease of solid fraction, which also causes the change from k_c to k_e, one may assume that

$$\frac{h_{wp}^{\nu}}{h_{wp}} \sim \frac{k_e}{k_c}.$$

Hence comes the second approximation. The validity and breakdown of the assumptions may be observed from Figure 5.5 where 1.26 mm and 3.04 mm glass beads are well correlated with equation (5.7) but a slight scatter is found with 0.50 mm glass beads. From Figure 5.6, it is also observed that glass beads (relatively good conductor) are well correlated with equation (5.7) but polystyrene beads (poor conductor) are not well correlated.

The difficulty in determining the value for χ at the critical solid fraction is associated with the complexity of the local geometric arrangement of particles. In particular, the roughness δ significantly affects the value for χ. This may explain why the value for χ of the present experiments is different from that of Sullivan and Sabersky. First, the difference in cleanliness of the surfaces of the heating plates used in two experiments may result in different values for χ. Second, it may be noted that the experiment of Sullivan and Sabersky was conducted with a vertical rectangular pipe while the present experiment has been done in an inclined chute. As a result, in the experiment of Sullivan and Sabersky, once a particle moves off the wall, it takes a longer time for the particle to come back to the wall. But in the present experiment in an inclined chute, the particles that are slightly above the wall come into contact with the wall in a relatively shorter time because of normal velocity due to gravity. Therefore, for high density flows, the experiment of Sullivan and Sabersky is expected to have a larger average gaseous gap between the particles and the wall. This larger average gaseous gap serves as larger roughness of the wall surface in the equation of Schlünder. Consequently, the value for χ in Sullivan and Sabersky's experiment is larger than that in the present experiment.

As a brief summary, the prediction of heat transfer rate in both the subcritical and supercritical regimes becomes possible using the single expression (5.7) with the effective Nusselt number and Peclet number. However, the breakdown of the use of equation (5.7) is also observed for the case in which the particle diameter is small or the thermal conductivity of the material is low. The estimate of the constant χ using a simple analysis is limited because of complexities in the surface conditions, the particle shapes, and the specific configurations of experimental facilities.

CHAPTER 6
NUMERICAL ANALYSIS OF HEAT TRANSFER TO GRANULAR FLOWS

The purpose of the present numerical analysis of heat transfer is to explore the possibility of using numerical methods in heat transfer problems on granular flows. In particular, heat transfer in the supercritical flow regime is of prime interest. The basic idea behind the present numerical analysis is that the heat transfer rate should be related to velocity and local density near the wall, provided that the particle random motion in the direction normal to the wall is not an important factor in the heat transfer process. The analysis requires a precise description of the density profile near the wall.

6.1 DENSITY-VARYING SINGLE PHASE CONTINUUM MODEL

6.1.1 Energy Equation and Boundary Conditions

For a two-dimensional flow in which the x-direction is the direction of flow and the y-direction is the direction normal to a flat plate, the energy equation is represented as

$$\rho c u \frac{\partial \Theta}{\partial x} = \frac{\partial}{\partial y}\left(k \frac{\partial \Theta}{\partial y}\right),$$

where Θ is the thermodynamic temperature. A simple calculation shows that the dissipation term in the energy equation of granular materials is negligible in the present application. For granular flows, the density ρ and the thermal conductivity k vary with y and their profiles are required. The combination of density and specific heat capacity of the granular medium, ρc, may be approximated by $\rho_p \nu c_p$, which is the value for the solid particle phase, since the density of the solid particle is much larger than that of gas. The major breakdown of this approximation occurs very close to the wall where ν is very low. However, when the interstitial gas is quasi-stationary near the wall, the gaseous quantity $(\rho c u)_{\text{gas}}$ plays little role in the convective heat transfer equation because the gas

heat flux $(\rho cu)_{gas}$ is negligible relative to the heat flux of the solid particles.

Consequently the present numerical analysis makes the following assumptions:

1) The interstitial gas is quasi-stationary. This is especially critical very near the wall where the solid fraction is very low. Because the no slip condition at the wall applies to the interstitial gas, this assumption is probably reasonable. The gas motions caused by particle motions are assumed to be negligible in heat transfer mechanism.

2) The solid phase has a constant uniform velocity denoted as U. This assumption is reasonable because only the region near the wall is important in heat transfer and within the small region the velocity is fairly uniform. This assumption was later verified by including the effect of velocity gradient in the energy equation though details of this are not included here.

Hence the granular medium is described as a single phase continuum, and in the energy equation ρcu is approximated by $\rho_p \nu c_p U$.

A constant wall temperature condition has been imposed from the leading edge of the heating plate to the trailing edge. The length of the heating plate is denoted as L. Then the boundary conditions are as follows:

$$\Theta(x,0) = \Theta_w \quad \text{for } 0 \le x \le L,$$
$$\Theta(x,0) = 0 \quad \text{for } x < 0,$$
$$\Theta(x,\infty) = 0.$$

The temperature, spatial coordinates, and thermal conductivity are nondimensionalized as follows:

$$\Theta^* = \frac{\Theta}{\Theta_w},$$
$$x^* = \frac{x}{L},$$
$$y^* = \frac{y}{d},$$
$$k^* = \frac{k}{k_g}.$$

The energy equation then becomes

$$\nu \mathrm{Pe}^{**} \frac{\partial \Theta^*}{\partial x^*} = \frac{\partial}{\partial y^*}\left(k^* \frac{\partial \Theta^*}{\partial y^*}\right), \tag{6.1}$$

where

$$\mathrm{Pe}^{**} = \frac{UL}{\alpha_c}\left(\frac{d}{L}\right)^2 \left(\frac{k_c}{k_g}\right)\frac{1}{\nu_c}. \tag{6.2}$$

And the boundary conditions become

$$\Theta^*(x^*, 0) = 1 \quad \text{for } 0 \le x^* \le 1,$$

$$\Theta^*(x^*, 0) = 0 \quad \text{for } x^* < 0,$$

$$\Theta^*(x^*, \infty) = 0.$$

6.1.2 Profiles of Solid Fraction and Thermal Conductivity

Granular flows in an inclined chute are characterized by complex density profiles. The density of a flow varies along the chute and also varies over the depth of flow. Furthermore, due to the detailed shape of particles and the random motion of particles, the density profile near the wall is extremely complex. Since the region near the wall is important in heat transfer process, it is necessary to examine the density profile near the wall in detail.

As a first approximation the heat transfer analysis employs the following assumptions.

1) There is no active convective motion in the y-direction due to random particle motion. Therefore, particles in the first layer next to the wall remain in the first layer.
2) Only the first layer next to the wall is of prime concern in the heat transfer to supercritical flows. In other words, the thermal boundary layer for rapid flows is in most cases less than one diameter in thickness. This assumption was validated by examining temperature profiles in the results.
3) Within the first layer, particles are uniformly or randomly distributed.

Because of the nature of these assumptions, the analysis may be valid only for rapid granular flows (or supercritical flows).

With the above assumptions, the local density of uniformly distributed particles over the space of the first layer is obtained. The height of the first layer is

assumed to be the characteristic particle spacing s, which is calculated from the mean solid fraction ν_m as

$$s^* = \frac{s}{d} = \left(\frac{\pi/6}{\nu_m}\right)^{1/3}.$$

If ν_m is greater than $\pi/6$, then s^* is assumed to be 1; in other words, all the particles are in contact with the wall if ν_m is greater than $\pi/6$.

It is assumed that the centers of particles are uniformly distributed between $y = d/2$ and $y = s - d/2$. Then the following solid fraction profile is obtained.

For $0 \leq y^* \leq (s^* - 1)$,

$$\nu(y^*) = \nu_m \frac{s^*}{s^* - 1}(3y^{*2} - 2y^{*3}). \tag{6.3}$$

For $(s^* - 1) \leq y^* \leq 1$,

$$\nu(y^*) = \nu_m s^*(-6y^{*2} + 6s^*y^* - 2s^{*2} + s^* + 1). \tag{6.4}$$

The region above $y = d$ or $y^* = 1$ is not taken into consideration. The solid fraction profile $\nu(y^*)$ is an increasing function of y^*, and it is also assumed that $\nu(y^*)$ is equal to ν_m above y^*_m at which $\nu(y^*)$ becomes ν_m.

For example, the solid fraction profile in case of $\nu_m = 0.4$ is illustrated in Figure 6.1 (a). Since $s^* = 1.09$ for $\nu_m = 0.4$, equation (6.3) is used for $0 < y^* < 0.09$. According to equation (6.4), the mean solid fraction is achieved at $y^*_m = 0.24$. Therefore, equation (6.4) is used for $0.09 < y^* < 0.24$, and $\nu(y^*) = \nu_m$ above $y^* = 0.24$.

This profile, including the sudden change of solid fraction at y^*_m, seems rather artificial. However, it is found that the results of the numerical analysis are quite insensitive to the form of the profile above y^*_m, provided the flow is rapid with high Pe**. For slow flows with low Pe**, the thermal boundary layer must be larger than one particle diameter, and the above profile may be no longer appropriate for the heat transfer analysis.

The profile of thermal conductivity is obtained from the result of Gelperin and Einstein [1971], which is shown in equation (5.6). The solid fraction profile

obtained above is used in equation (5.6). The ratio $k_s/k_g = 35$, 8.4, and 6.7 are selected for glass, mustard seed, and polystyrene respectively. The profile of thermal conductivity for $\nu_m = 0.4$ is shown in Figure 6.1 (b).

6.1.3 Numerical Schemes

With the profiles of solid fraction and thermal conductivity, and with one parameter, Pe^{**}, the equation (6.1) is numerically solved for Θ^* using a simple explicit method. At a grid point (x_i^*, y_j^*), where $x_i^* = i\Delta x^*$ and $y_j^* = j\Delta y^*$ with $i, j = 1, 2, 3...$, the equation (6.1) is approximated as

$$\Theta^{*i+1}_j = \Theta^{*i}_j + \frac{\Delta x^*}{2(\Delta y^*)^2}\frac{1}{\nu_j Pe^{**}}\Big\{(k^*_{j-1} + k^*_j)\Theta^{*i}_{j-1} - (k^*_{j-1} + 2k^*_j + k^*_{j+1})\Theta^{*i}_j + (k^*_j + k^*_{j+1})\Theta^{*i}_{j+1}\Big\},$$

where ν_j and k_j^* are the values at y_j^*. A criterion for the stability of the system is

$$1 - \frac{\Delta x^*}{2(\Delta y^*)^2 \nu_j Pe^{**}}(k^*_{j-1} + 2k^*_j + k^*_{j+1}) > 0.$$

Since ν_j has the minimum at $j = 1$, the stability condition becomes

$$\Delta x^* < \frac{2(\Delta y^*)^2 \nu_1 Pe^{**}}{k^*_{j-1} + 2k^*_j + k^*_{j+1}}.$$

The instability of the system was a problem, especially for flows with low Pe^{**} and ν.

The modified Nusselt number is defined as

$$Nu^* = \frac{hd}{k_g} = -k^* \frac{\partial \Theta^*}{\partial y^*}\Big|_{y^*=0}.$$

The last term in the above expression can be obtained integrating the equation (6.1) from $y^* = 0$ to $y^* = \infty$. Therefore,

$$Nu^* = \int_0^\infty \nu Pe^{**} \frac{\partial \Theta^*}{\partial x^*} dy^*.$$

The integration was done numerically, and the Nusselt number was averaged over the heating plate.

6.2 RESULTS OF ANALYSIS AND COMPARISON

6.2.1 Results of Analysis

The present numerical analysis involves a large number of assumptions which, in particular, may cease to be valid for slow flows with high solid fraction. However, in order to examine how high the mean solid fraction can be, results were obtained even for high solid fraction.

In Figure 6.2, the modified Nusselt number Nu^* is plotted against the Peclet number Pe^{**} for various mean solid fraction, ν_m. For a given solid fraction, Nu^* increases with Pe^{**}, and for a given Pe^{**}, Nu^* increases with ν_m. But Nu^* at $\nu_m = 0.6$ seems to be underestimated when the increments of Nu^* with increasing ν_m are considered. This may be because the solid fraction profiles were not accurately determined for high solid fraction. For example, when ν_m is greater than $\pi/6 \simeq 0.52$, the characteristic spacing s^* is unity. It implies that there is little distinction in cases of $\nu_m > 0.52$. Therefore, the increment of Nu^* between $\nu_m = 0.5$ and 0.6 appears to be small.

It may be interesting to compare the results with the case in which the constant heat flux at the wall is assumed as a boundary condition. Figure 6.3 shows there is only a slight difference between the results for the two boundary conditions. This also assures that any deviation from the constant wall temperature condition has little effect on the heat transfer results.

Another parameter in the present analysis is the thermal conductivity ratio of solid phase to gas phase. As shown in Figure 6.1 (b), the ratio k_s/k_g influences the profile of the thermal conductivity of the granular medium. The effect of k_s/k_g on the numerical results is demonstrated in Figure 6.4 in which the cases of $k_s/k_g = 35$ and 6.7 are compared. For low mean solid fraction, the results are little affected by the values of k_s/k_g. But as solid fraction increases, the difference becomes substantial.

Finally, the temperature profiles at the trailing edge ($x^* = 1$) are investi-

gated for various Pe** and ν_m. The effect of Pe** on the temperature profile is shown in Figure 6.5. The higher the Peclet number, the smaller the thermal boundary layer. Note that for Pe** > 100 the thickness of the thermal boundary layer is less than one particle diameter, as required by the assumptions behind the solid fraction profile. In Figure 6.6, the effect of ν_m for a given Pe** is examined. For lower mean solid fraction, a thicker thermal boundary layer is observed. Physically, for low solid fraction, particles can move more freely in the direction normal to the flat plate. As a result, heat is convected to a location further from the flat plate through the vertical motions of particles. Analytically, a higher solid fraction plays a role similar to a higher Peclet number (see equation (6.1)). In the present analysis, a lower mean solid fraction results in a larger characteristic particle spacing and thus a larger height of the first layer where particles are in random motions or uniformly distributed. This is consistent with the previous physical argument. However, this observation should not be confused with the fact that for a higher mean solid fraction the overall heat transfer rate is larger (see Figure 6.2).

6.2.2 Comparison with Experimental Data

In Figure 6.7, the results of the numerical analysis for $k_s/k_g = 35$ are compared with the present experimental data for three sizes of glass beads. Different symbols are used for different mean solid fractions. In general, the numerical results show the same magnitudes and the same trends as the experimental data. However, as anticipated earlier, the Nusselt number obtained numerically for $\nu_m = 0.6$ is somewhat smaller than that of the experimental data. This indicates that the present analysis may not be accurate for the flows with high solid fraction. Nevertheless, the discrepancy between the analysis and the experimental data for high solid fraction does not appear to be substantial.

In Figure 6.8, the experimental data with polystyrene beads ($k_s/k_g = 6.7$) and mustard seeds ($k_s/k_g = 8.4$) are also plotted along with the data for glass beads ($k_s/k_g = 35$). The numerical results agree well with all the experimental

data. This may be because, though dependent on the value of k_s/k_g, the numerical results for low solid fraction are little affected by the values of k_s/k_g (see Figure 6.4).

In spite of numerous assumptions involved in the energy equation and the profiles of solid fraction and thermal conductivity, the present results demonstrate that the basic mechanism is sufficiently well understood to justify using numerical methods in heat transfer analysis. When the details of flow conditions near the wall are better understood, the numerical approach to heat transfer problems may be improved.

CHAPTER 7
SUMMARY AND CONCLUSION

Experimental Study of Shear Flows of Granular Materials

Experiments on continuous, steady flows of granular materials down an inclined chute have been made with the objectives of understanding the characteristics of chute flows, and of acquiring information on the rheological behavior of granular materials. Two neighboring fibre optic displacement probes were used to measure (1) the mean velocity by cross-correlating two signals from the probes, (2) one component of velocity fluctuations by identifying each particle from the signals and thus obtaining the velocity of each particle, and (3) the mean particle spacing at the boundaries by counting the frequency of particle passage. The mean particle spacing also gave qualitative information on density near the boundaries. In addition, a strain-gauged plate was employed to directly measure shear stress at the chute base. The surface of the chute base was carefully controlled to yield three distinct surface conditions; smooth aluminum surface, moderately smooth aluminum surface, rubber-coated surface. Each surface condition was characterized by Coulombic friction coefficient and the coefficient of restitution between the chute base and a particle.

The preliminary experiments indicate that the flow at the free surface is less affected by the sidewalls than at the chute base; the transverse velocity profile at the free surface is close to uniform. It is also observed that the higher the velocity (or the higher the chute inclination), the less significant the sidewall effect.

Vertical profiles of velocity, velocity fluctuation, and linear concentration have been measured through lucite windows in the sidewalls. The velocity profile is fairly linear except for the region within the distance of one particle diameter from the chute base. Velocity fluctuation increases with distance from the chute base. This granular conduction from the bulk of the flow to the chute base wall is opposite to what we observe from the results of Campbell and Brennen [1985b].

The results of Ahn *et al.* [1989b] or chapter 4 in the present thesis indicate that granular temperature can be conducted either toward or away from the chute base, depending on the value of the particle-particle coefficient of restitution and the chute inclination. In the present measurements, linear concentration always decreases monotonically with distance from the chute base. This result is also different from the results found in the other literature. The surface condition of the chute base plays an important role in the above profiles. The profiles of velocity and its fluctuation with the smooth surface (the surface with low Coulombic friction coefficient) are more uniform than those with the rubber-coated surface (the surface with high Coulombic friction coefficient).

The characteristics of the chute flow of granular materials have been studied by measuring various basic flow properties. The experimental data are strongly affected by the surface condition of the chute base. The ratio of velocity fluctuation to mean velocity is fairly constant for the smooth and moderately smooth surfaces, but for the rubberized surface it clearly increases as the solid fraction decreases. And the ratio for the rubberized surface is much larger than those for the smooth and moderately smooth surfaces. Regardless of the surface conditions, the mean shear rate increases at high solid fraction with decreasing solid fraction. But for the rubberized surface the mean shear rate shows a drastic decrease at low solid fraction. The high ratio of velocity fluctuation to mean velocity causes particles to move from one location to another more frequently, and as a result the velocity gradient is reduced. For the smooth surface where the ratio is low, the decrease of mean shear rate is not observed with decreasing solid fraction.

The variation of friction coefficient with solid fraction is similar to that of the ratio of velocity fluctuation to mean velocity. For the smooth and moderately smooth surfaces, the friction coefficient is fairly constant. But for the rubberized surface, it increases with decreasing solid fraction. As a result, the friction coefficient appears to be a linear function of the ratio of velocity fluctuation to

mean velocity.

The stress measurements have also been used to study the rheological behavior of granular material. In particular, the rheological models presented by Lun *et al.* [1984] have been compared with the experimental results. The rheological models for general flow (equations (2.8) and (2.9)) give good correlation to the present experimental data. With the smooth and moderately smooth surfaces, it was not possible to create fully developed flow, probably because of low Coulombic friction coefficients for the surfaces. But some selected experimental data with the rubberized surface, which are close to fully developed flow, are well correlated with the rheological models for fully developed flow (equation (2.18) or (2.19)). Since the chute flows of the present experiments are characterized by granular conduction, the rheological models for simple shear flow (equations (2.13) and (2.14)) do not provide good correlation for the present experimental data.

Analysis of the Fully Developed Chute Flow of Granular Materials

The analysis of fully developed flow has been conducted to investigate the role of granular conduction in determining the profiles of granular temperature, solid fraction, and mean velocity. The governing equations and the constitutive relations presented by Lun *et al.* [1984] have been employed in the present analysis, and the boundary value problem has been formulated with two parameters (e_p and $\tan\theta$). This boundary value problem has been numerically solved by the "shooting method." Three boundary values at the wall (ν_w, T_w, and u_w) are required for the solution, and the boundary conditions at the free surface are met by adjusting the gradient of temperature at the wall. The results show all the boundary conditions at the free surface are satisfied once the wall boundary conditions are properly chosen; at the free surface, ν vanishes, and the gradients of ν, T, and u also vanish, satisfying the condition of no energy flux at the free surface.

The solutions fall into two categories, and the two parameters (e_p and $\tan\theta$) determine which type of flow will occur. The first type has a granular temperature which increases from the wall boundary to the free surface. The solid fraction monotonically decreases with distance from the chute base, and the free surface is not well defined. The second type exhibits high temperature near the chute base, and a rapid decrease of the temperature as the free surface is approached. In the latter type the solid fraction is low at both boundaries but high in the center of the flow, and the free surface is rather clearly defined. A transitional type is also found which exhibits features of both the first and second types of flow; the temperature increases near the wall but decreases thereafter. The solid fraction has a profile similar to the first type.

These profiles are closely connected to the role of the granular conduction term in the fluctuation energy equation. The conduction term, which depends on e_p, $\tan\theta$, and ν, determines the energy flux, and thus the gradients of granular temperature and solid fraction, causing different profiles to occur. The conduction term appears to be significant in magnitude compared to the dissipation term. This behavior is fundamentally different from simple shear flow in which no conduction exists.

The effect of the variations of the parameter and wall boundary values is also studied. As the chute inclination angle increases, granular temperature, mean velocity, and the depth of flow increase. A higher granular temperature at the wall also causes an overall increase in temperature, mean velocity, and flow depth. An increase in the solid fraction at the wall also yields the same result.

Comparisons with experiments and computer simulations have been made. The experiments of Ahn *et al.* [1989a] or section 3.2.2 in the present thesis correspond with Type I flows. The experimental data show that, with distance from the chute base, the solid fraction decreases monotonically, and granular temperature increases, indicating granular conduction from the free surface to the wall. The results of the present analysis are consistent with those data. The

general profiles of flow properties are well predicted though some discrepancies in their magnitudes are observed. On the other hand, the computer simulations by Campbell and Brennen [1985b] correspond to Type II flows. Granular conduction from the wall to the free surface is observed, and the solid fraction is low at both boundaries but high in the bulk. Good agreement between the present analysis and the computer simulations is found when a slightly different value of the parameter $\tan\theta$ is used as an input. The decrease of granular temperature with distance from the wall is well predicted, and the profile of solid fraction is similar to that of the computer simulations. Some discrepancies may be due to the fact that the computer simulations were conducted with two-dimensional disks.

The different types of flow occurring in the experiments and the computer simulations are the results of the different values of the coefficient of restitution appropriate to those circumstances. A high value of e_p, such as the value of about 0.95 in the experiments, causes the granular temperature to be conducted from the free surface to the wall, and a low value of e_p, such as the value of 0.6 used in the computer simulations, results in granular conduction in the opposite direction.

Experimental Study of Heat Transfer to Granular Flows

The convective heat transfer to granular flows has been studied experimentally. Three sizes of glass beads, polystyrene beads, and mustard seeds were used to investigate the effects of different particle size and different thermal properties. The flat heating plate was installed at the hole cut into the chute base, and temperatures were measured using thermocouples. The results, similar to those of Patton *et al.* [1986], are characterized by the two flow regimes. In the subcritical regime the heat transfer rate increases with increasing velocity, but in the supercritical regime the heat transfer rate decreases with decreasing solid fraction as the velocity increases further.

In order to accommodate the variation of solid fraction, the previous model of Sullivan and Sabersky [1975] has been slightly modified using the effective Nusselt number and the effective Peclet number, which include the terms dependent on solid fraction. The modified model has provided a single expression (5.7) to describe the heat transfer characteristics of both fast and slow flows (supercritical and subcritical flows). The experimental data are fairly well correlated with the modified model though some data with polystyrene beads (poor conductor) substantially deviate from the prediction of the model. The value of the experimental constant χ in the present experiments is found to be different from that of Sullivan and Sabersky, because of different configurations of experimental facilities. The determination of χ still remains for further study.

Numerical Analysis of Heat Transfer to Granular Materials

The numerical analysis of convective heat transfer to granular materials has been performed. The prime objective of the present numerical analysis was to explore the feasibility of using numerical methods in heat transfer problems on granular flows. The basic idea behind the present numerical analysis was that the heat transfer rate should be related to the velocity and the local density near the heating plate, provided that the particle motion in the direction normal to the wall is not an important factor in the heat transfer process.

The density-varying single phase continuum model has been developed for numerical analysis. The two-dimensional energy equation was simplified by assuming that the interstitial gas is quasi-stationary and that the solid phase has a constant uniform velocity. The governing equation has one parameter (the Peclet number, Pe**) and requires the profiles of solid fraction and thermal conductivity. The solid fraction profile has been obtained assuming that only the layer next to the wall is of importance in the heat transfer process and that within the layer particles are uniformly or randomly distributed. With these assumptions the profile depends only on the mean solid fraction. The profile of thermal

conductivity has been determined with the solid fraction profile and the result of Gelperin and Einstein [1971] which contains the parameter k_s/k_g. A constant wall temperature condition has been chosen as the boundary condition, and the equation has been solved using a simple explicit method.

The results are presented in terms of the Nusselt number Nu*, the Peclet number Pe**, and the mean solid fraction ν_m. For a given ν_m, Nu* increases with Pe**, and for a given Pe**, Nu* increases with ν_m. The effect of a different boundary condition such as a constant wall heat flux and the effect of the variation of k_s/k_g have been studied, and no significant effect has been found. The temperature profile at the trailing edge has also been presented. The thermal boundary layer appears to be less than one particle diameter thick for higher Peclet numbers (e.g., Pe** $>$ 100). Finally, the numerical results have been compared with the experimental data obtained in chapter 5, and reasonable agreement is observed in the comparison.

REFERENCES

Ahn, H., Brennen, C.E., and Sabersky, R.H., 1988, Experiments on chute flows of granular materials. *Micromechanics of granular materials*, (ed. M. Satake and J.T. Jenkins), Elsevier Pub. Co., Amsterdam, 339-348.

Ahn, H., Brennen, C.E., and Sabersky, R.H., 1989a, Measurements of velocity, velocity fluctuation, density, and stresses in chute flows of granular materials. *To be submitted to J. App. Mech.*

Ahn, H., Brennen, C.E., and Sabersky, R.H., 1989b, Analysis of the fully developed chute flow of granular materials. *To be submitted to J. App. Mech.*

Augenstein, D.A., and Hogg, R., 1978, An experimental study of the flow of dry powders on inclined surfaces. *Powder Technology* **19**, 205-215.

Bagnold, R.A., 1954, Experiments on a gravity-free dispersion of large solid particles in a Newtonian fluid under shear. *Proc. R. Soc. Lond.* **A225**, 49-63.

Bailard, J., 1978, "An Experimental Study of Granular-Fluid Flow." Ph.D. Thesis, University of California, San Diego.

Bauer, R., and Schlünder, E.U., 1978a, Effective radial thermal conductivity of packings in gas flow. Part I. Convective transport coefficient. *Int. Chem. Eng.* **18**, No. 2, 181-188.

Bauer, R., and Schlünder, E.U., 1978b, Effective radial thermal conductivity of packings in gas flow. Part II. Thermal conductivity of the packing fraction without gas flow. *Int. Chem. Eng.* **18**, No. 2, 189-204.

Campbell, C.S., 1982, "Shear Flow of Granular Materials." Ph.D. Thesis, California Institute of Technology.

Campbell, C.S., 1986, The effect of microstructure development on the collisional stress tensor in a granular flow. *Acta Mechanica* **63**, 61-72.

Campbell, C.S., 1988, Boundary interactions for two-dimensional granular flows: Asymmetric stresses and couple stresses. *Micromechanics of granular materials*, (ed. M. Satake and J.T. Jenkins), Elsevier Pub. Co., Amsterdam, 163-174.

Campbell, C.S., 1989a, The stress tensor for simple shear flows of a granular material. *J. Fluid Mech., to be published.*

Campbell, C.S., 1989b, Rapid granular flows. *Prepared for Volume 22 of the Annual Review of Fluid Mechanics.*

Campbell, C.S., and Brennen, C.E., 1985a, Computer simulation of granular shear flows. *J. Fluid Mech.* **151**, 167-188.

Campbell, C.S., and Brennen, C.E., 1985b, Chute flows of granular material: some computer simulation. *J. App. Mech.* **52**, 172-178.

Campbell, C.S., and Gong, A., 1986, The stress tensor in a two-dimensional granular shear flow. *J. Fluid Mech.* **164**, 107-125.

Campbell, C.S., and Gong, A., 1987, Boundary conditions for two-dimensional granular flows. *Proceedings of the International Symposium on Multiphase Flows,* Hangzhou China, **1**, 278-283.

Campbell, C.S., and Wang, D.G., 1986, The effective conductivity of shearing particle flows. *Proc. of 8th Int. Heat Transfer Conference* **4**, 2567-2572.

Craig, K., Buckholz, R.H., and Domoto, G., 1986, An experimental study of the rapid flow of dry cohesionless metal powders. *J. App. Mech.* **53**, 935-942.

Drake, T.G. and Shreve, R.L., 1986, High-speed motion pictures of nearly steady, uniform, two-dimensional, inertial flows of granular material. *J. Rheology* **30**, 981-993.

Eid, J.C., and Antonetti, V.W., 1986, Small scale thermal contact resistance of aluminum against silicon. *Proc. of 8th Int. Heat Transfer Conference*, 659-664.

Gelperin, N.I., and Einstein, V.G., 1971, Heat transfer in fluidized beds. *Fluidization*, (ed. J.F. Davidson and D. Harrison), Academic Press, London and New York, 471-568.

Hanes, D.M., and Inman, D.L., 1985, Observations of rapidly flowing granular-fluid flow. *J. Fluid Mech.* **150**, 357-380.

Holman, J.P., 1981, "Heat Transfer." Fifth edition, McGraw-Hill Book Company, New York, 116.

Hui, K., Haff, P.K., Ungar, J.E., and Jackson, R., 1984, Boundary conditions for high-shear grain flows. *J. Fluid Mech.* **145**, 223-233.

Jenkins, J.T., and Richman, M.W., 1985, Kinetic theory for plane flows of a dense gas of identical, rough, inelastic, circular disks. *Phys. Fluid* **28**, 3485-3494.

Jenkins, J.T., and Richman, M.W., 1986, Boundary conditions for plane flows of smooth, nearly elastic, circular disks. *J. Fluid Mech.* **171**, 53-69.

Jenkins, J.T., and Savage, S.B., 1983, A theory for the rapid flow of identical, smooth, nearly elastic particles. *J. Fluid Mech.* **130**, 187-202.

Johnson, P.C., and Jackson, R., 1987, Frictional-collisional constitutive relations for granular materials, with application to plane shearing. *J. Fluid Mech.* **176**, 67-93.

Johnson, P.C., and Jackson, R., 1988, Frictional-collisional equations of motion for particulate flows and their application to chutes. *Submitted to J. Fluid Mech.*

Lun, C.K.K., and Savage, S.B., 1986, The effects of an impact velocity dependent coefficient of restitution on stresses developed by sheared granular materials. *Acta Mechanica* **63**, 15-44.

Lun, C.K.K., and Savage, S.B., 1987, A simple kinetic theory for granular flow of rough, inelastic, spherical particles. *J. App. Mech.* **54**, 47-53.

Lun, C.K.K., Savage, S.B., Jeffrey, D.J. and Chepurniy, N., 1984, Kinetic theories for granular flow: inelastic particles in Couette flow and slightly inelastic particles in a general flowfield. *J. Fluid Mech.* **140**, 223-256.

Martin, H., 1984, Heat transfer between gas fluidized beds of solid particles and the surfaces of immersed heat exchanger elements, Part I. *Chem. Eng. Process* **18**, 157-169.

Maw, N., Barber, J.R., and Fawcett, J.N., 1976, The oblique impact of elastic spheres. *Wear* **38**, 101-114.

Maw, N., Barber, J.R., and Fawcett, J.N., 1981, The role of elastic tangential compliance in oblique impact. *J. of Lubrication Technology* **103**, 74-80.

Muchowski, E., 1980, Heat transfer from the bottoms of vibrated vessels to packings of spheres at atmospheric pressure and under vacuum. *Int. Chem. Eng.* **20**, No. 4, 564-576.

Nakagawa, M., 1988, "Kinetic Theory for Plane Flows of Rough, Inelastic Circular Discs." Ph.D. Dissertation, Cornell University, Ithaca, NY.

Ogawa, S., Umemura, A., and Oshima, N., 1980, On the equations of fully fluidized granular materials. *J. App. Math. Phys. (ZAMP)* **31**, 483-493.

Patton, J.S., 1985, "Experimental Study of Shear Flows and Convective Heat Transfer Characteristics of Granular Materials." Ph.D. Thesis, California Institute of Technology.

Patton, J.S., Brennen, C.E., and Sabersky, R.H., 1987, Shear flows of rapidly flowing granular materials. *J. App. Mech.* **54**, 801-805.

Patton, J.S., Sabersky, R.H., and Brennen, C.E., 1986, Convective heat transfer to rapidly flowing granular materials. *Int. J. Heat Mass Transfer* **29**, No. 8, 1263-1269.

Ridgway, K., and Rupp, R., 1970, Flow of granular material down chutes. *Chem. Proc. Eng.* **51**, 82-85.

Savage, S.B., 1979, Gravity flow of cohesionless granular materials in chutes and channels. *J. Fluid Mech.* **92**, 53-96.

Savage, S.B., 1984, The mechanics of rapid granular flows. *Advances in Applied Mechanics* **24**, (ed. J. Hutchinson and T.Y. Wu), Academic Press, 289-366.

Savage, S.B., and Jeffrey, D.J., 1981, The stress tensor in a granular flow at high shear rates. *J. Fluid Mech.* **110**, 255-272.

Savage, S.B., and McKeown, S., 1983, Shear stress developed during rapid shear of dense concentrations of large spherical particles between concentric cylinders. *J. Fluid Mech.* **127**, 453-472.

Savage, S.B., and Sayed, M., 1984, Stresses developed by dry cohesionless granular materials in an annular shear cell. *J. Fluid Mech.* **142**, 391-430.

Sayed, M., and Savage, S.B., 1983, Rapid gravity flow of cohesionless granular materials down inclined chutes. *J. Appl. Math. Phys.* **34**, 84-100.

Schlünder, E.U., 1980, Heat transfer to moving spherical packings at short contact times. *Int. Chem. Eng.* **20**, No. 4, 550-554.

Schlünder, E.U., 1984, Heat transfer to packed and stirred beds from the surface of immersed bodies. *Chem. Eng. Process* **18**, 31-53.

Spelt, J.K., 1981, "An Experimental Study of Heat Transfer to Flowing Granular Media." Report No. E200.3, California Institute of Technology.

Spelt, J.K., Brennen, C.E., and Sabersky, R.H., 1982, Heat transfer to flowing granular material. *Int. J. Heat Mass Transfer* **25**, No. 6, 791-796.

Sullivan, W.N., 1973, "Heat Transfer to Flowing Granular Media." Ph.D. Thesis, California Institute of Technology.

Sullivan, W.N., and Sabersky, R.H., 1975, Heat transfer to flowing granular media. *Int. J. Heat Mass Transfer* **18**, 97-107.

Sun, J., and Chen, M.M., 1986, A theoretical analysis of heat transfer due to particle impact. ASME Paper No. 86-WA/ HT-89.

Walton, O.R., 1984, Computer simulation of particulate flow. Energy and Tech. Rev., Lawrence Livermore Lab., May 1984, p. 24.

Walton, O.R., and Braun, R.L., 1986a, Viscosity, granular-temperature, and stress calculations for shearing assemblies of inelastic, frictional disks. *J. of Rheology* **30(5)**, 949-980.

Walton, O.R., and Braun, R.L., 1986b, Stress calculations for assemblies of inelastic spheres in uniform shear. *Acta Mechanica* **63**, 73-86.

Walton, O.R., Braun, R.L., Mallon, R.G., and Cervelli, D.M., 1988, Particle-dynamics calculations of gravity flow of inelastic, frictional spheres. *Micromechanics of granular materials*, (ed. M. Satake and J.T. Jenkins), Elsevier Pub. Co., Amsterdam, 153-162.

Wunschmann, J., and Schlünder, E.U., 1980, Heat transfer from heated surfaces to spherical packings. *Int. Chem. Eng.* **20**, No. 4, 555-563.

APPENDIX A
THE OBLIQUE IMPACT OF INELASTIC SPHERES

Nomenclature

e_w	wall-particle coefficient of restitution in direction normal to the wall
f	friction coefficient defined as the ratio of J_x to J_y
I	momentum of inertia of the sphere about its center
J_x, J_y	tangential and normal components of the impulse at the wall
K	ratio of the radius of gyration to the radius of the sphere; $(I/mr^2)^{1/2}$
m	mass of the sphere
r	radius of the sphere
U_s	slip velocity at the contact surface
u_1, u_2	tangential velocities before and after impact
v_1, v_2	normal velocities before and after impact
α_1	impact angle given by $\tan^{-1}(u_1/v_1)$
μ	Coulombic friction coefficient
ω_1, ω_2	rotational rates before and after impact

Introduction

A simple analysis is developed for the oblique impact of an inelastic sphere on a half-space. Two solutions are obtained, depending on the boundary conditions. When slip occurs at the contact point between the sphere and the wall during the entire collision process, one solution is obtained with an assumption that the ratio of the tangential impulse to the normal impulse, the friction coefficient f, should be constant, equal to Coulombic friction coefficient, μ. The other solution is obtained when no slip condition at the contact point is assumed; in this case, appropriate tangential conditions are sought to equate the tangential velocity after impact, u_2, to its rotational velocity, $\omega_2 r$, and f is not necessary to remain constant.

In some cases in which impact angles are relatively low for a given surface condition, negative slip between the contact surfaces may occur due to the elastic recovery of the surface (see Maw *et al.* [1976, 1981]). In this analysis the negative slip will be neglected because of its application to the chute flow where high impact angles are expected.

In the derivation, it is assumed that μ is constant, and that e_w is also constant, independent of the impact angle and impact velocity. In the analysis the values of μ and e_w are assumed to be known.

Analysis

Taking all the quantities as positive by choosing a proper direction for each vector quantity, the following relations are obtained from linear and angular momentum conservations (see Figure A.1).

$$J_x = m(u_1 - u_2),$$

$$J_y = m(v_1 + v_2),$$

$$J_x r = I(\omega_2 - \omega_1).$$

And at the contact point,

$$\omega_2 r = u_2 - U_s.$$

And from the assumption,

$$e_w = v_2/v_1.$$

Now we have five equations with six unknowns; J_x, J_y, u_2, v_2, ω_2, and U_s. Therefore, we need one more condition to solve the system. Note that the case in which $\omega_1 r/u_1 > 1$ is excluded.

a) For the case in which slip occurs:

The friction coefficient, or the ratio of J_x to J_y, is assumed to be equal to μ. That is,

$$\mu = \frac{J_x}{J_y}.$$

Then, letting $K^2 = I/mr^2$ and $\tan\alpha_1 = u_1/v_1$, the quantities after impact are derived as follows:

$$
\begin{aligned}
v_2 &= e_w v_1, \\
\frac{u_2}{u_1} &= 1 - \frac{\mu(1+e_w)}{\tan\alpha_1}, \\
\frac{U_s}{u_1} &= 1 - \left(1 + \frac{1}{K^2}\right)\frac{\mu(1+e_w)}{\tan\alpha_1} - \frac{\omega_1 r}{u_1}, \\
\frac{\omega_2 r}{u_1} &= \frac{1}{K^2}\frac{\mu(1+e_w)}{\tan\alpha_1} + \frac{\omega_1 r}{u_1}.
\end{aligned}
$$

Note $K^2 = 2/5$ for a sphere.

b) For the case in which no slip occurs:

From no slip condition, we have $U_s = 0$. Then

$$
\begin{aligned}
v_2 &= e_w v_1, \\
\frac{u_2}{u_1} &= \frac{1}{1+K^2}\left(1 + K^2\frac{\omega_1 r}{u_1}\right), \\
\frac{\omega_2 r}{u_1} &= \frac{1}{1+K^2}\left(1 + K^2\frac{\omega_1 r}{u_1}\right).
\end{aligned}
$$

And the friction coefficient is given as

$$
f = \frac{K^2}{1+K^2}\left(1 - \frac{\omega_1 r}{u_1}\right)\frac{\tan\alpha_1}{1+e_w}.
$$

In the above equation, it should be noted that f cannot exceed μ. When the ratio of J_x to J_y is greater than μ, slip occurs and the solution does not hold any more.

APPENDIX B

ANALYSIS OF THE FULLY DEVELOPED CHUTE FLOW

Two momentum equations (4.1) and (4.2), and the fluctuation energy equation (4.3), with (4.4)-(4.7), may be reduced to the following alternative forms:

$$
\begin{aligned}
q^* &= -\int_0^{y^*} \left(g_5 - \frac{g_1^2}{g_2} \tan^2\theta \right) T^{*\frac{1}{2}} dy^* + q_w^*, \\
\frac{\partial T^*}{\partial y^*} &= \frac{1}{g_1' g_3 - g_1 g_4} \left(g_4 \nu - g_1' \frac{q^*}{T^{*\frac{1}{2}}} \right), \\
\frac{\partial \nu}{\partial y^*} &= -\frac{1}{T^* (g_1' g_3 - g_1 g_4)} \left(g_3 \nu - g_1 \frac{q^*}{T^{*\frac{1}{2}}} \right), \\
\frac{\partial u^*}{\partial y^*} &= \frac{g_1}{g_2} T^{*\frac{1}{2}} \tan\theta.
\end{aligned}
$$

Note that g_1 through g_5 are functions of e_p and ν, and thus q^*, T^*, ν, and u^* are functions of e_p and y^*. In addition to two parameters (e_p and $\tan\theta$), three boundary values (T^*, ν, and u^*) are given at the wall. The boundary value problem was solved by a "shooting method." The energy flux at the wall, q_w^*, is chosen by trial and error to satisfy the boundary condition at the free surface, which is $q^* \to 0$ as $y^* \to \infty$.

The integration was done by a simple scheme such as the well-known trapezoid rule, and the differential equations were solved by the Euler method. There were no problems with convergence, and these simple methods were sufficient to study the general characteristics of the chute flows.

APPENDIX C
MEASUREMENTS OF THERMAL PROPERTIES

C.1 THERMAL DIFFUSIVITY

In order to measure thermal diffusivity, the semi-infinite medium is considered which is maintained at an initial temperature Θ_i and then is suddenly elevated and maintained at a temperature Θ_o. The temperature distribution at any x position in the medium is given as a function of time τ as follows:

$$\frac{\Theta(x,\tau)-\Theta_o}{\Theta_i-\Theta_o}=\operatorname{erf}\frac{x}{2\sqrt{\alpha\tau}},$$

where erf is the Gauss error function.

The principal apparatus is a four by four inch copper plate attached to a heater whose power output is controlled by a variable autotransformer. One thermocouple measures the temperature of the copper plate, and the other thermocouple is located at the distance x from the center of the copper plate to measure the temperature of the granular medium. The experimental procedure begins with a rapid increase in the copper plate temperature to some Θ_o which is about 25°C above the initial temperature Θ_i. In order to maintain Θ_o, the power output of the heater is controlled as time proceeds. The temperature at the position x is recorded every minute. Usually $\tau = 20\,\text{min.}$ and $x \sim 2\,\text{cm}$ were chosen in calculating α. It took about a minute to raise the copper plate temperature from Θ_i to Θ_o, and the temperature Θ_o was maintained with a tolerance of 0.3°C.

C.2 THERMAL CONDUCTIVITY

The semi-infinite medium with the initial temperature Θ_i is again considered to directly measure thermal conductivity. At $\tau = 0$, the surface is suddenly exposed to a constant heat flux q_o. The solution for this case is (see Holman [1981])

$$\Theta(x,\tau)-\Theta_i=\frac{q_o}{k}\left\{\frac{2\sqrt{\alpha\tau}}{\sqrt{\pi}}\exp\left(\frac{-x^2}{4\alpha\tau}\right)-x\left(1-\operatorname{erf}\frac{x}{2\sqrt{\alpha\tau}}\right)\right\}.$$

Once the thermal diffusivity α is known, therefore, the thermal conductivity k can be obtained by measuring q_o, τ, x, and $\Theta(x,\tau)$.

A four by four inch heater is placed in the granular medium, and a thermocouple is located at the distance x from the center of the heater. After the heater is turned on, the heat flux, the elapsed time, and the temperature at x are recorded at regular intervals. The power output of the heater was usually about $1500\,\mathrm{W/m^2}$, and the distance x was about 2 cm. Various values for τ were used in calculating k using the previous measurements of α.

The specific heat capacity c was then obtained using the values of α and k as follows:

$$c = \frac{k}{\rho_p \nu_c \alpha}.$$

Since the density of the interstitial gas is far lower than that of the solid particles, the above approximation is valid. All the properties were measured at the critical solid fraction ν_c.

	glass beads	glass beads	glass beads	polystyrene beads	mustard seeds
diameter (mm)	3.04	1.26	0.50	3.15	2.22
standard deviation (%)	7.2	2.9	14.9	19.7	12.6
critical solid fraction	0.59	0.61	0.60	0.58	0.64
solid density (kg/m^3)	2500	2500	2500	1010	1100
thermal conductivity ($W/m \cdot °C$)	0.20	0.20	0.20	0.073	0.092
thermal diffusivity (m^2/s)	1.5×10^{-7}	1.5×10^{-7}	1.5×10^{-7}	0.93×10^{-7}	0.87×10^{-7}

Table 1. Properties of granular materials

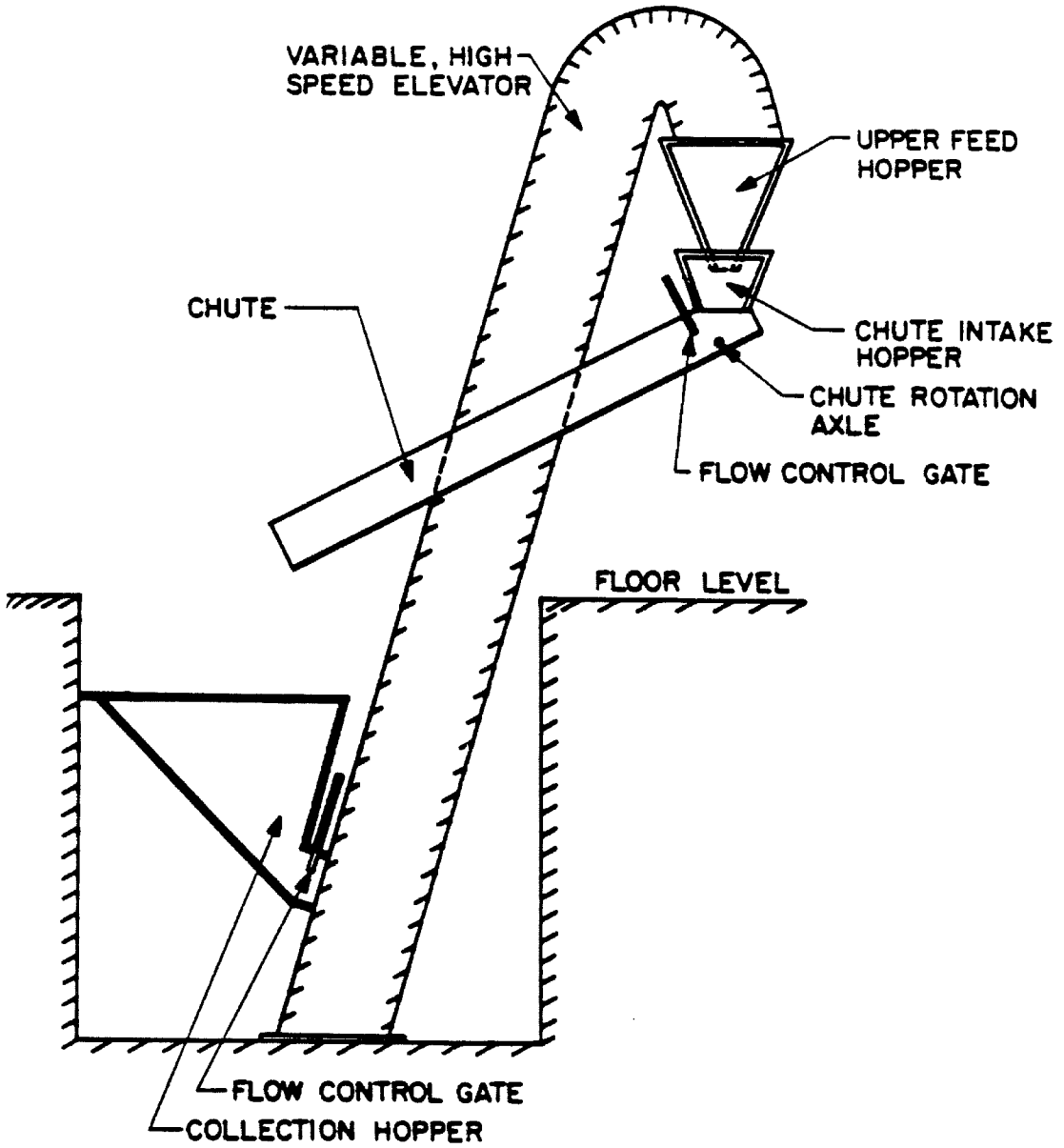

Figure 3.1. Schematic of the experimental facility.

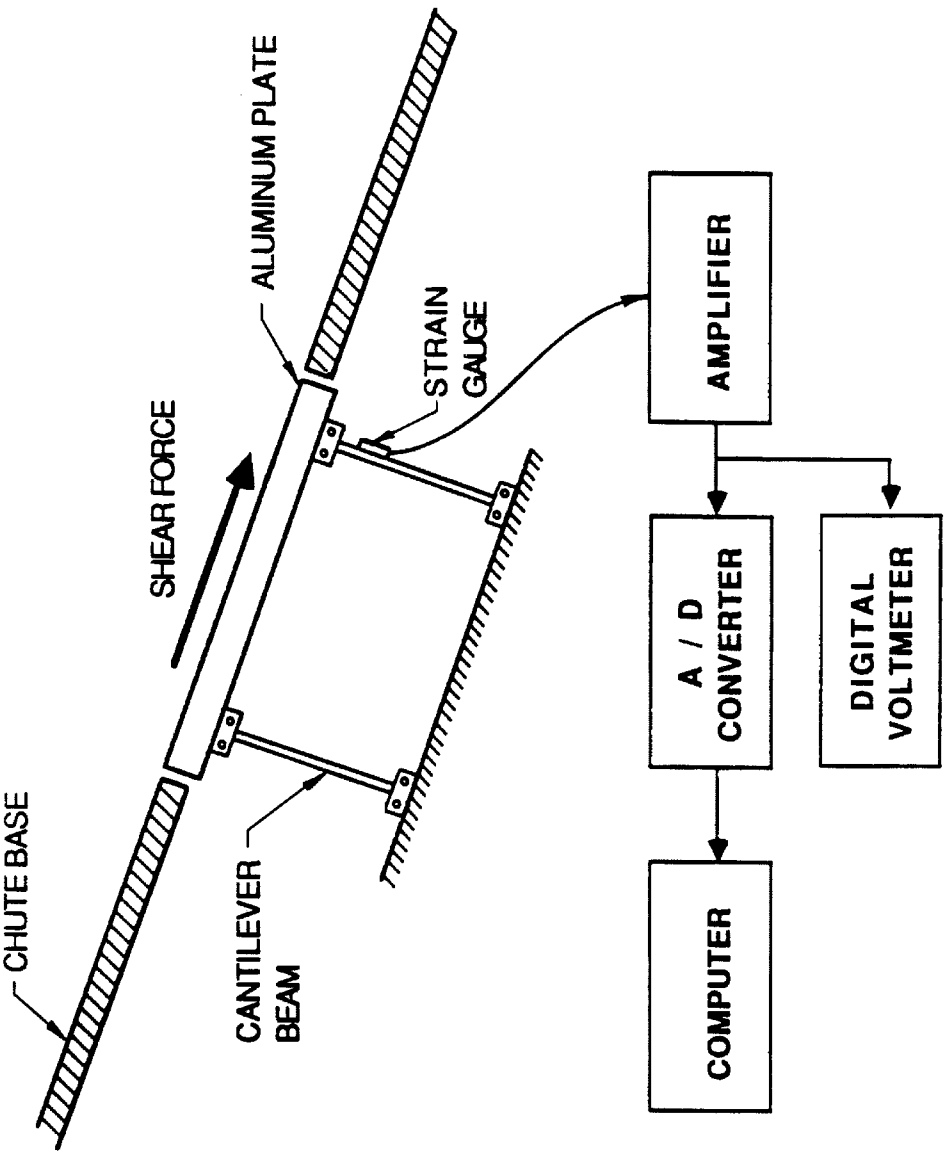

Figure 3.2. Schematic of the shear gauge.

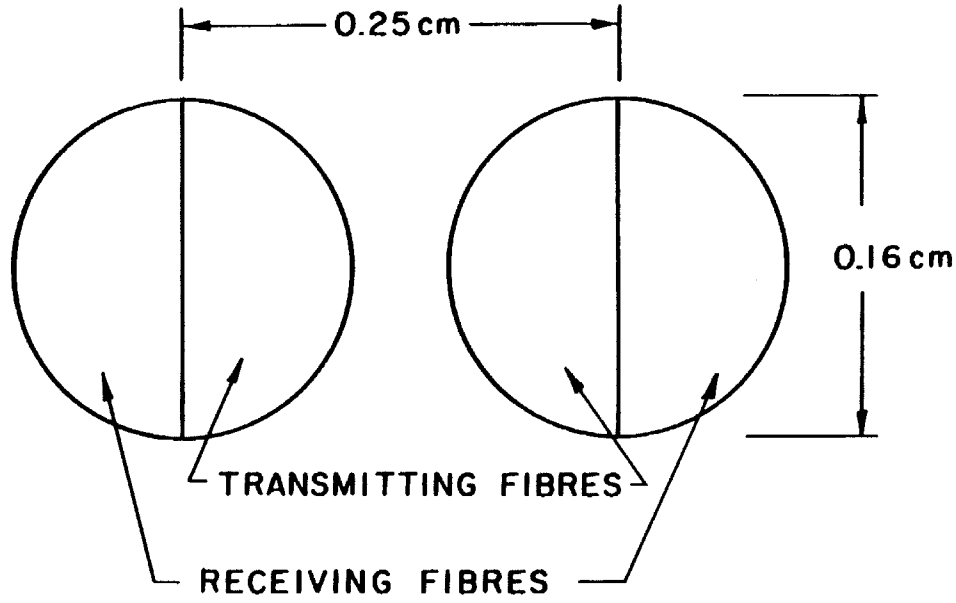

Figure 3.3. Geometry of the faces of the two displacement probes used for velocity measurements with the 1.26 mm diameter glass beads.

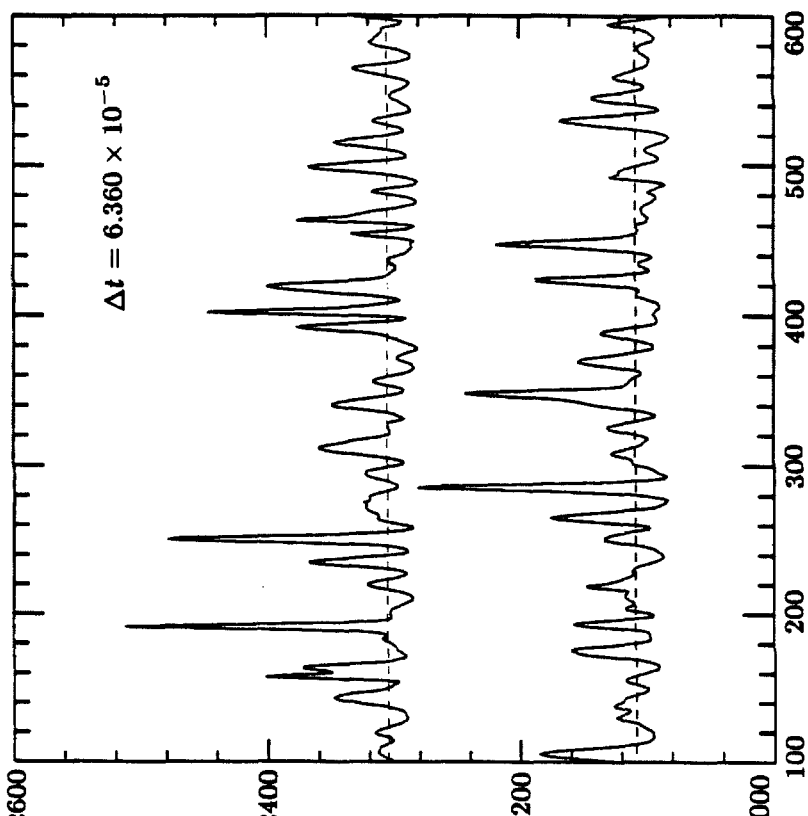

Figure 3.4. Typical signals from two neighboring fibre optic probes. Voltage output (1 unit = 2.44 millivolts) against the time, t, normalized by the time interval between each sample, $\Delta t = 6.360 \times 10^{-5}$ sec. Threshold voltages shown in dotted lines.

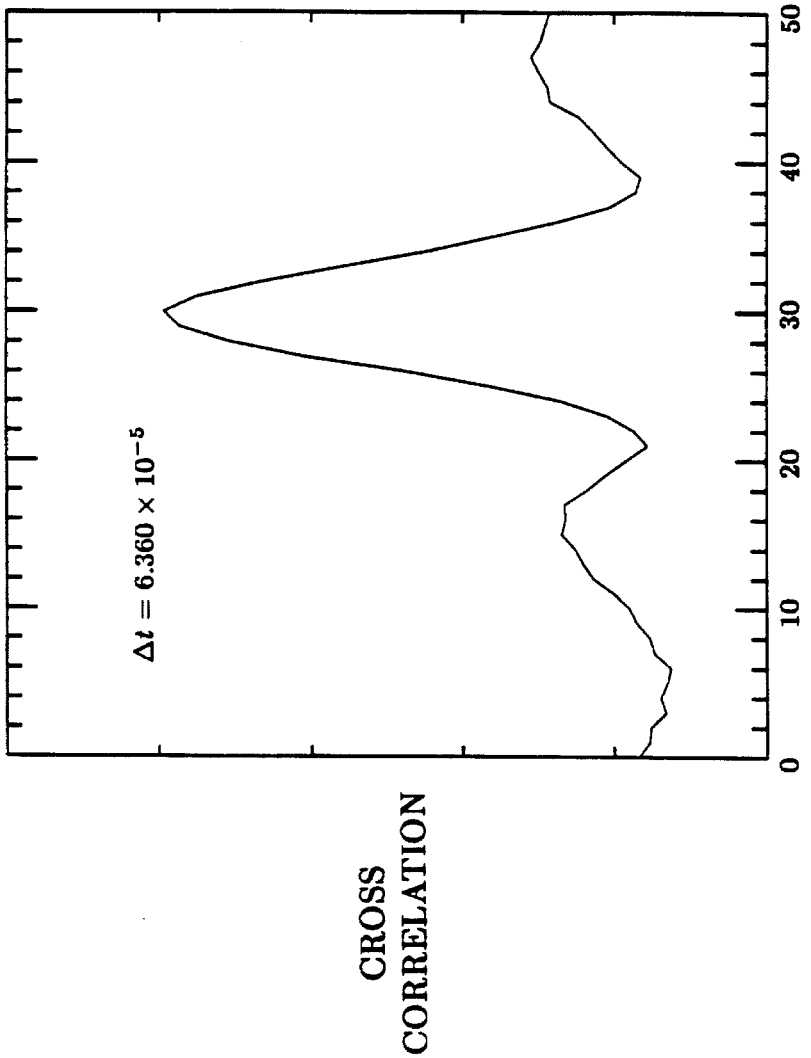

Figure 3.5. Output of cross-correlation of two signals shown in Figure 3.4.

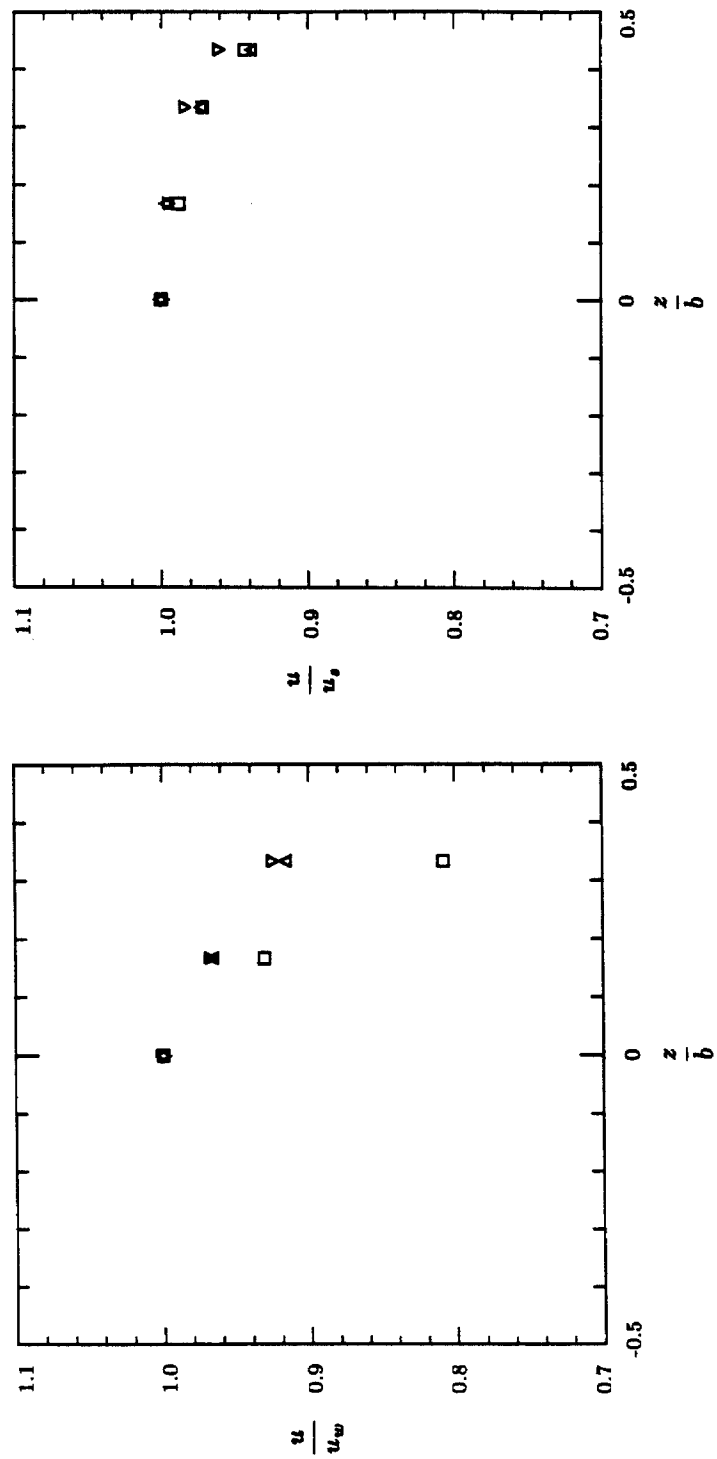

Figure 3.6. The transverse velocity profiles (a) at the chute base and (b) at the free surface; mean velocity normalized by mean velocity at the center against the lateral location, z, normalized by the chute width, $b = 76.2$ mm. □, $\theta = 17.8°$, $\nu_m = 0.54$, $u_w = 0.898$ m/sec, and $u_s = 1.118$ m/sec; △, $\theta = 22.7°$, $\nu_m = 0.50$, $u_w = 1.386$ m/sec, and $u_s = 1.639$ m/sec; ▽, $\theta = 32.2°$, $\nu_m = 0.49$, $u_w = 2.055$ m/sec, and $u_s = 2.263$ m/sec. u_w, velocity at the center on the chute base; u_s, velocity at the center on the free surface.

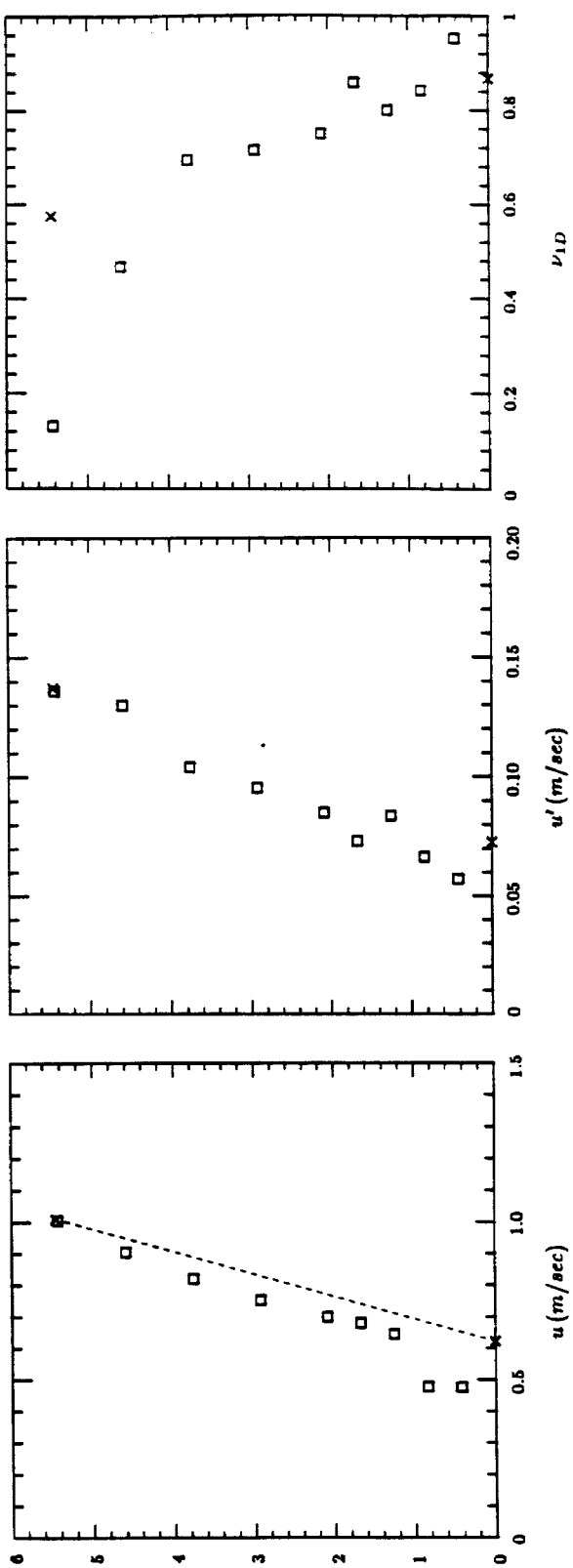

Figure 3.7. The vertical profile at the sidewall, □. Vertical location, y, normalized by the particle diameter d against (a) mean velocity, (b) velocity fluctuation, and (c) linear concentration. ×, data at the center of the chute. Dotted line, the assumed velocity profile at the center of the chute. Data were taken at $\theta = 17.8°$ on the rubberized surface; $\nu_m = 0.30$, $h_o = 25.4$ mm, and $d = 3.04$ mm.

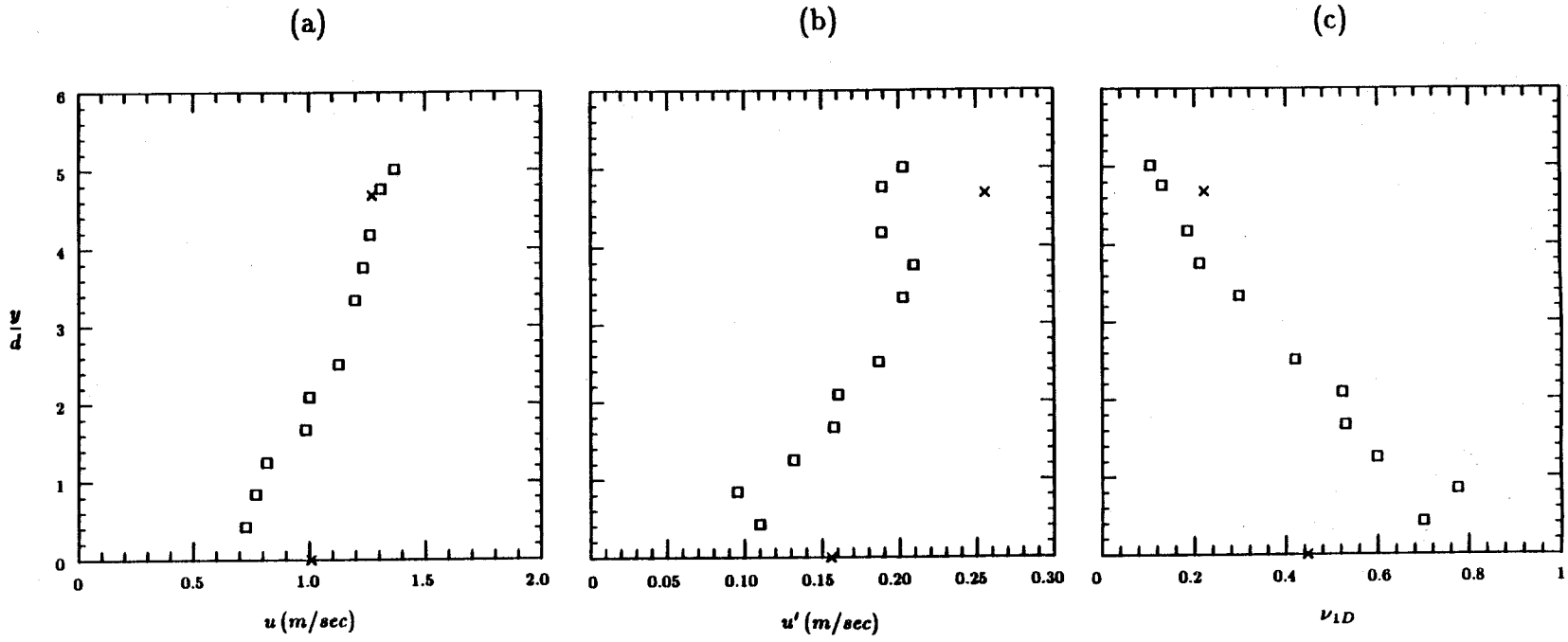

Figure 3.8. The vertical profile at the sidewall, □. Vertical location, y, normalized by the particle diameter d against (a) mean velocity, (b) velocity fluctuation, and (c) linear concentration. ×, data at the center of the chute. Data were taken at $\theta = 22.7°$ on the rubberized surface; $\nu_m = 0.10$, $h_o = 15.9\,\text{mm}$, and $d = 3.04\,\text{mm}$.

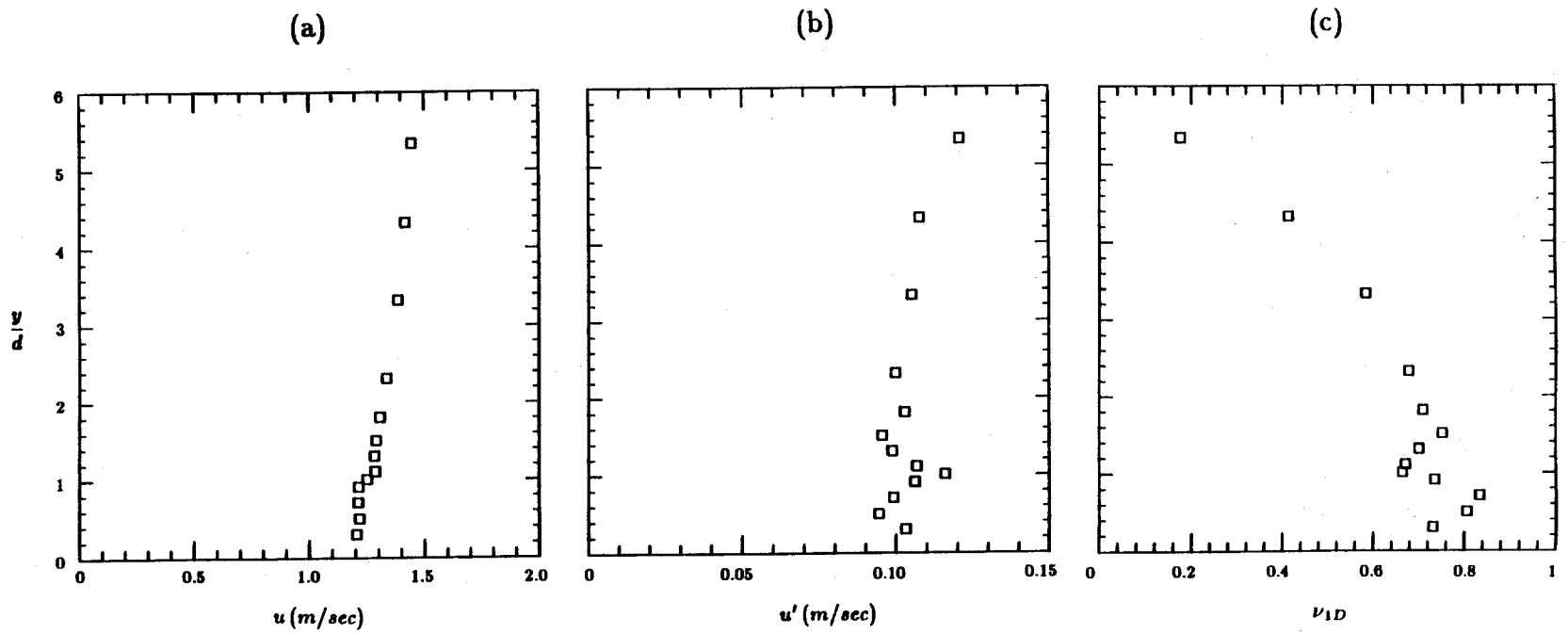

Figure 3.9. The vertical profile at the sidewall, □. Vertical location, y, normalized by the particle diameter d against (a) mean velocity, (b) velocity fluctuation, and (c) linear concentration. Data were taken at $\theta = 22.7°$ on the smooth surface; $h_o = 15.9\,\text{mm}$ and $d = 1.26\,\text{mm}$.

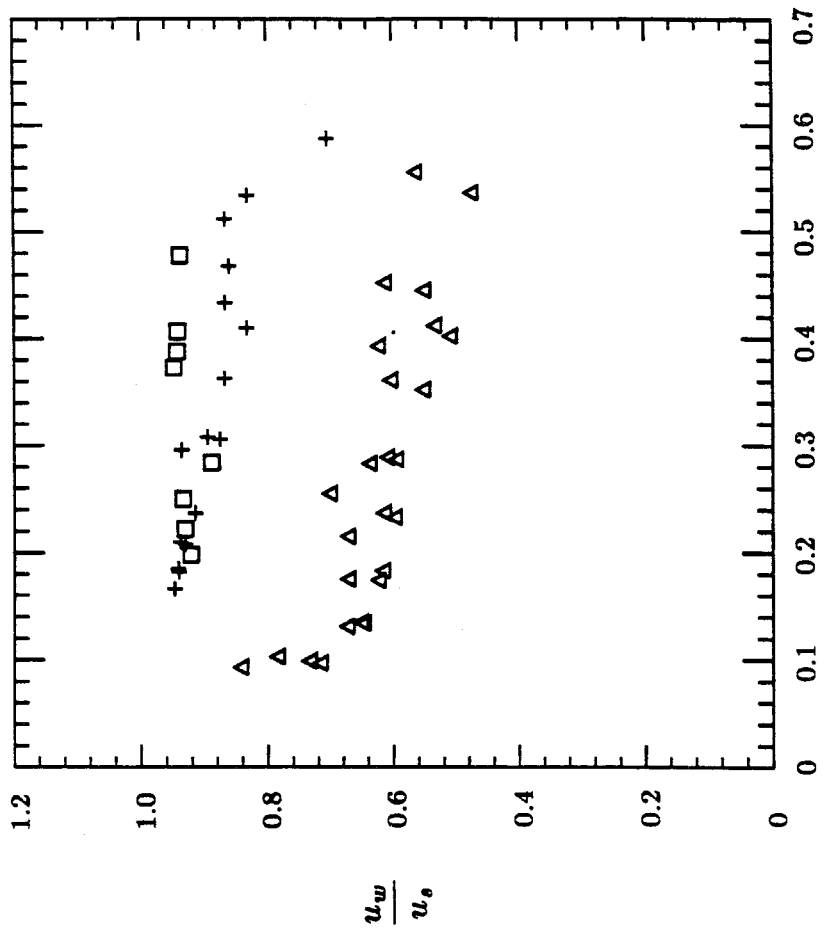

Figure 3.10. The ratio of velocity at the chute base wall to velocity at the free surface, u_w/u_s, against mean solid fraction, ν_m. □, the smooth surface; +, the moderately smooth surface; △, the rubberized surface.

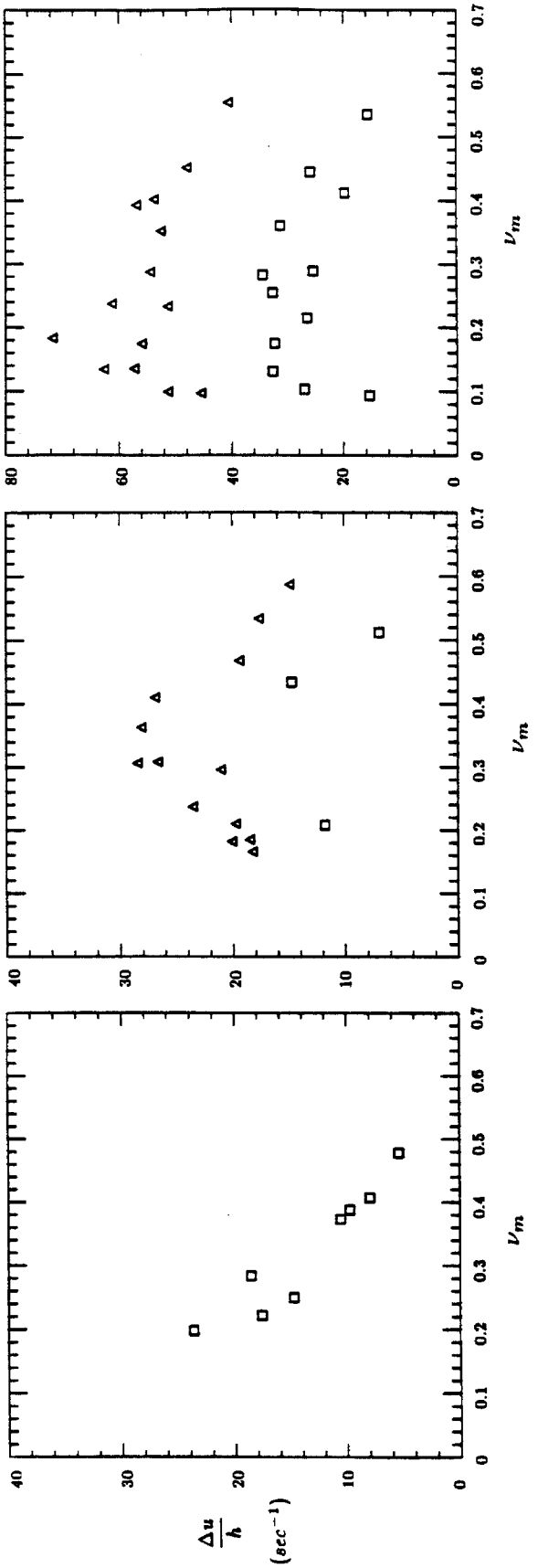

Figure 3.11. The shear rate, $\Delta u/h$, against mean solid fraction, ν_m: (a) the smooth surface, (b) the moderately smooth surface, and (c) the rubberized surface. □, $d = 3.04$ mm; △, $d = 1.26$ mm.

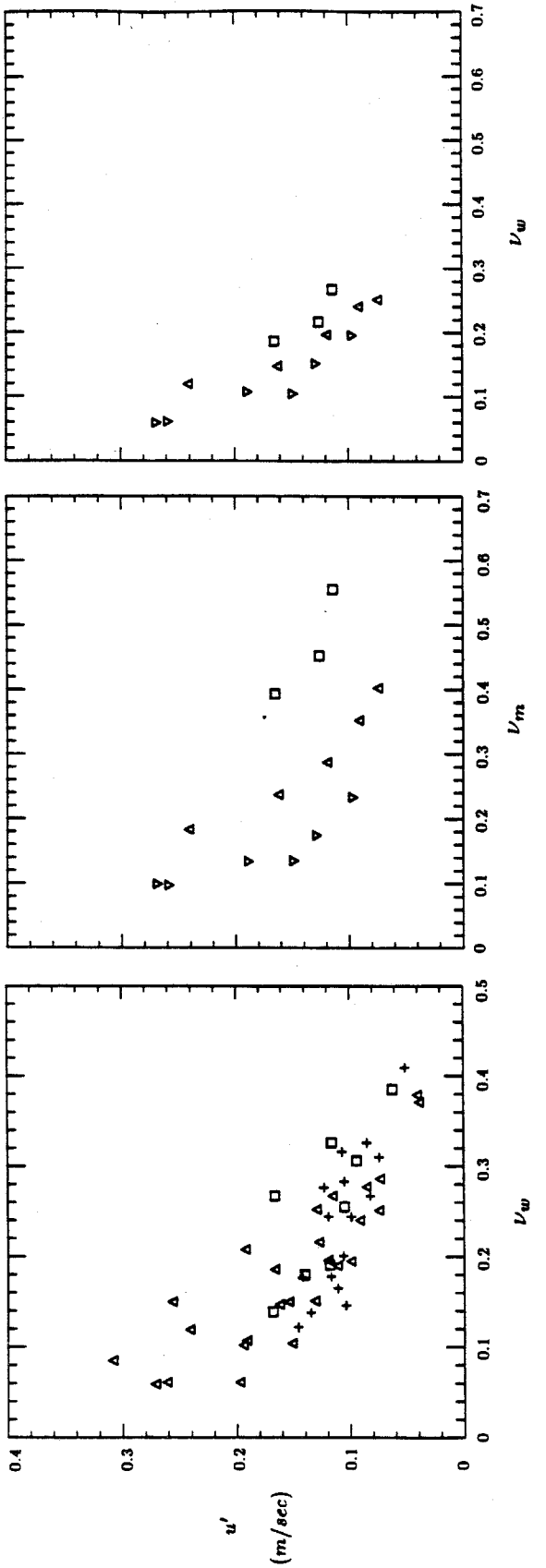

Figure 3.12. The longitudinal velocity fluctuation at the wall, u'_w, against solid fraction with the rubberized surface. (a) Data for $d = 1.26$ mm and $d = 3.04$ mm. □, the smooth surface; +, the moderately smooth surface; △, the rubberized surface. (b) Data for $d = 1.26$ mm. □, $h_o = 38.1 \sim 50.8$ mm; △, $h_o = 25.4$ mm; ▽, $h_o = 12.7 \sim 15.9$ mm. (c) Data as in (b).

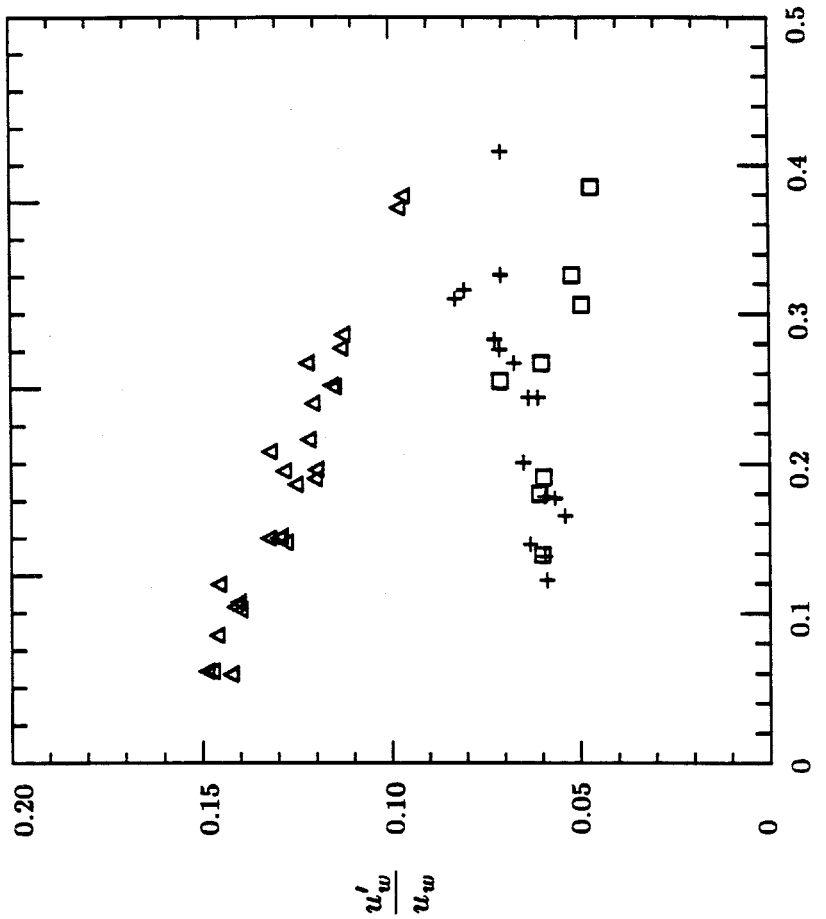

Figure 3.13. The longitudinal velocity fluctuation at the chute base wall normalized by mean velocity, u'_w/u_w, against wall solid fraction, ν_w. □, the smooth surface; +, the moderately smooth surface; △, the rubberized surface.

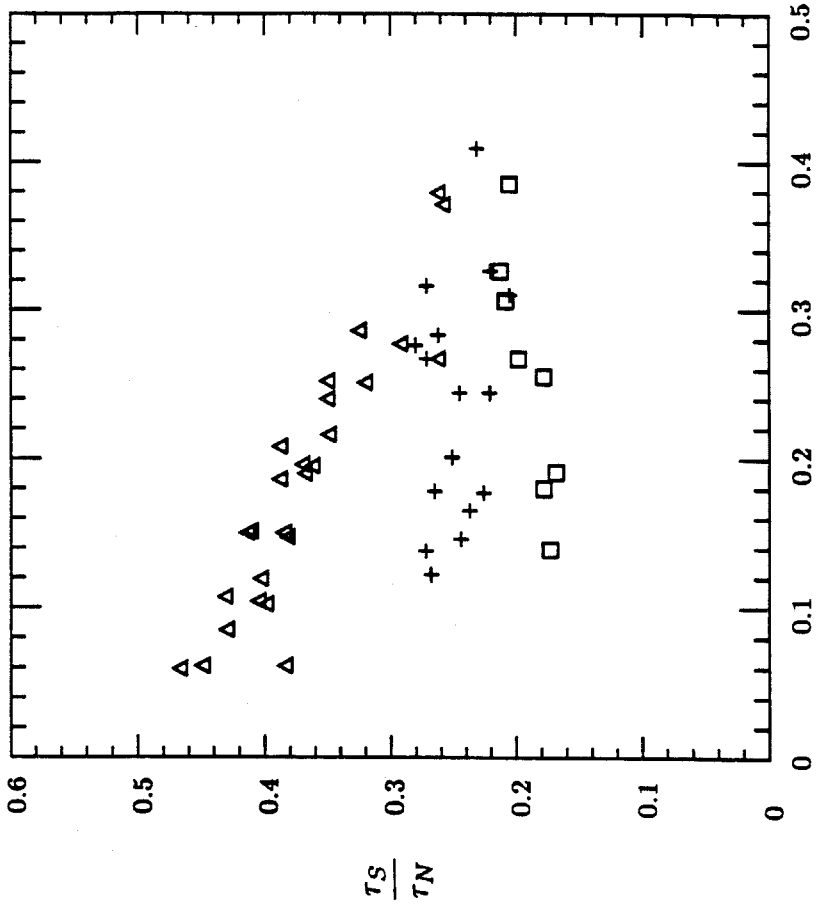

Figure 3.14. Friction coefficient at the wall, $f = \tau_S/\tau_N$, against wall solid fraction, ν_w. □, the smooth surface; +, the moderately smooth surface; △, the rubberized surface.

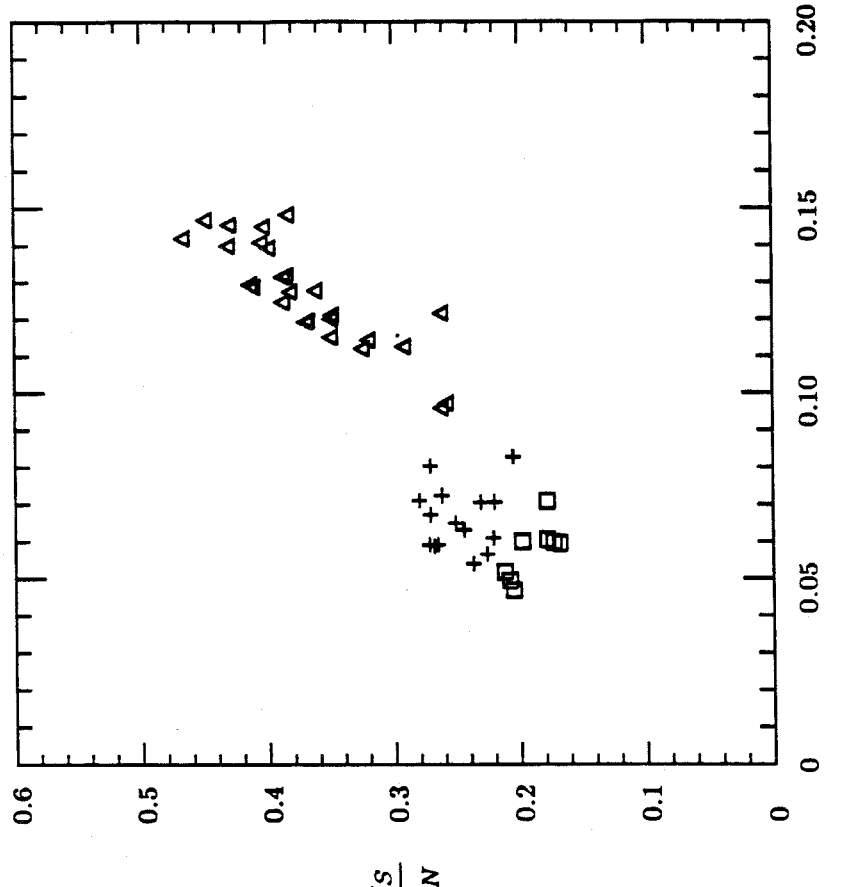

Figure 3.15. Friction coefficient at the wall, $f = \tau_S/\tau_N$, against longitudinal velocity fluctuation at the wall normalized by mean velocity, u'_w/u_w. □, the smooth surface; +, the moderately smooth surface; △, the rubberized surface.

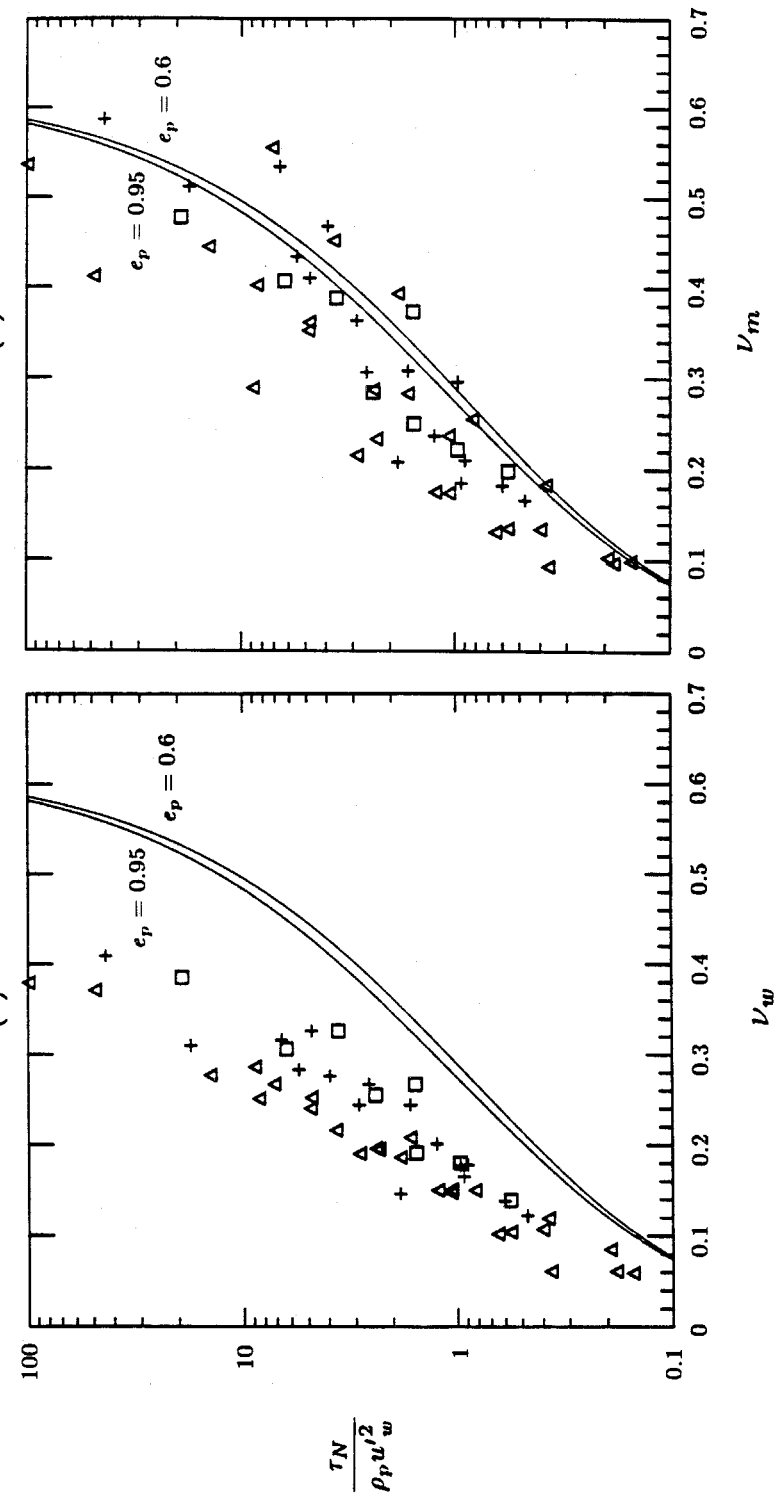

Figure 3.16. The normalized normal stress, $\tau_N/\rho_p u_w'^2$, against (a) wall solid fraction, ν_w, and (b) mean solid fraction, ν_m. □, the smooth surface; +, the moderately smooth surface; △, the rubberized surface. The solid lines, the results of Lun et al. [1984].

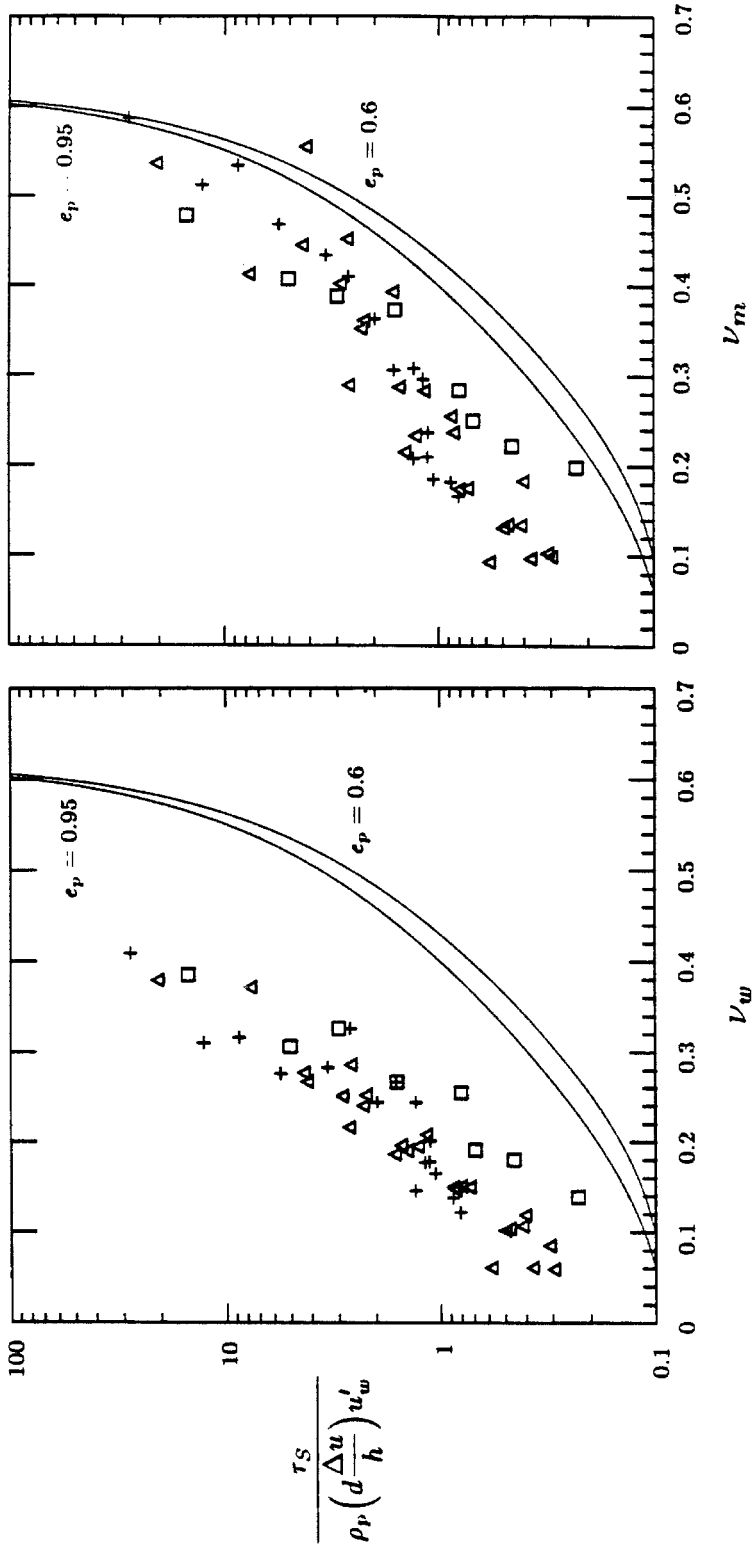

Figure 3.17. The normalized shear stress, $\tau_S/\rho_p d(\Delta u/h)u'_w$, against (a) wall solid fraction, ν_w, and (b) mean solid fraction, ν_m. □, the smooth surface; +, the moderately smooth surface; △, the rubberized surface. The solid lines, the results of Lun et al. [1984].

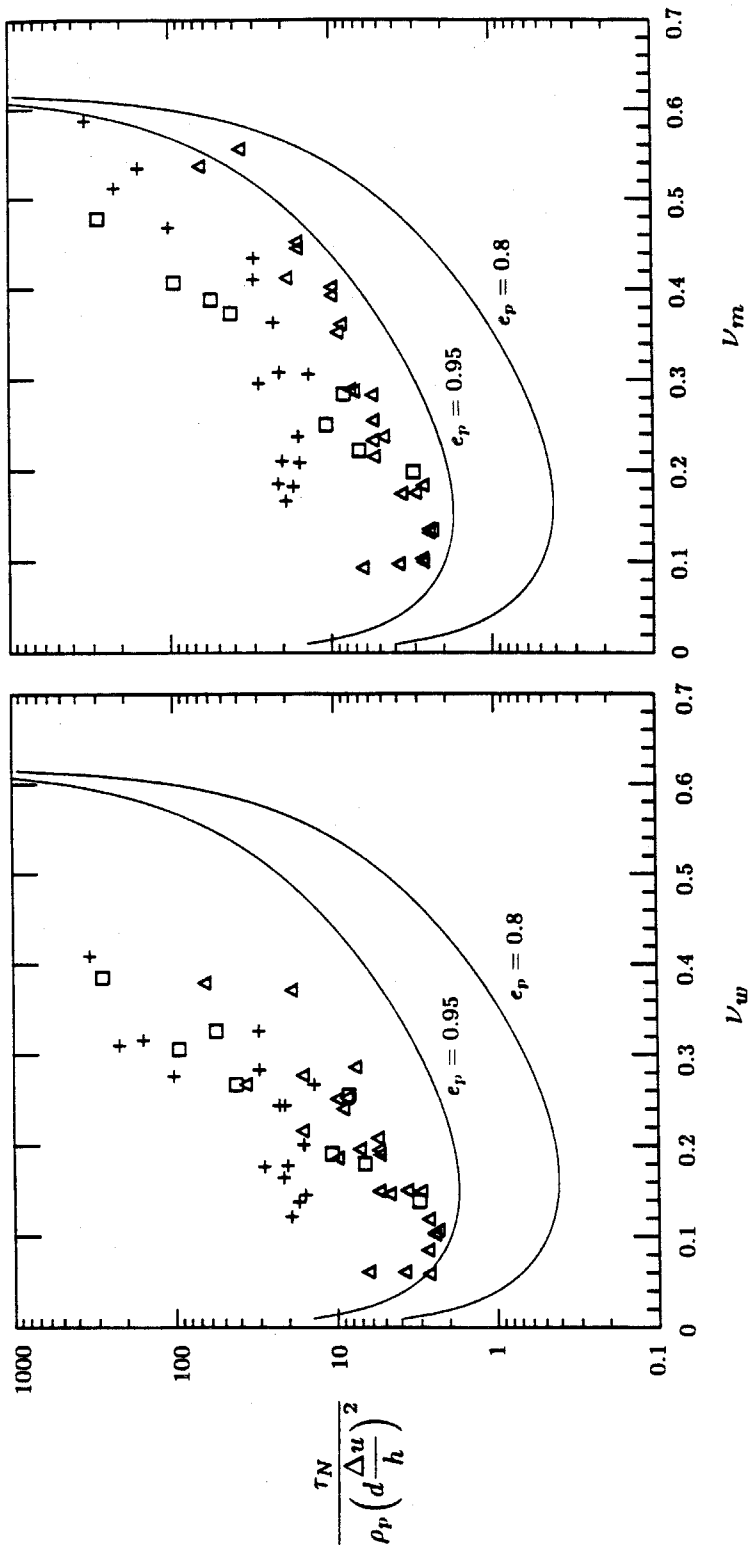

Figure 3.18. The normalized normal stress, $\tau_N/\rho_p(d\Delta u/h)^2$, against (a) wall solid fraction, ν_w, and (b) mean solid fraction, ν_m. □, the smooth surface; +, the moderately smooth surface; △, the rubberized surface. The solid lines, the results of Lun et al. [1984].

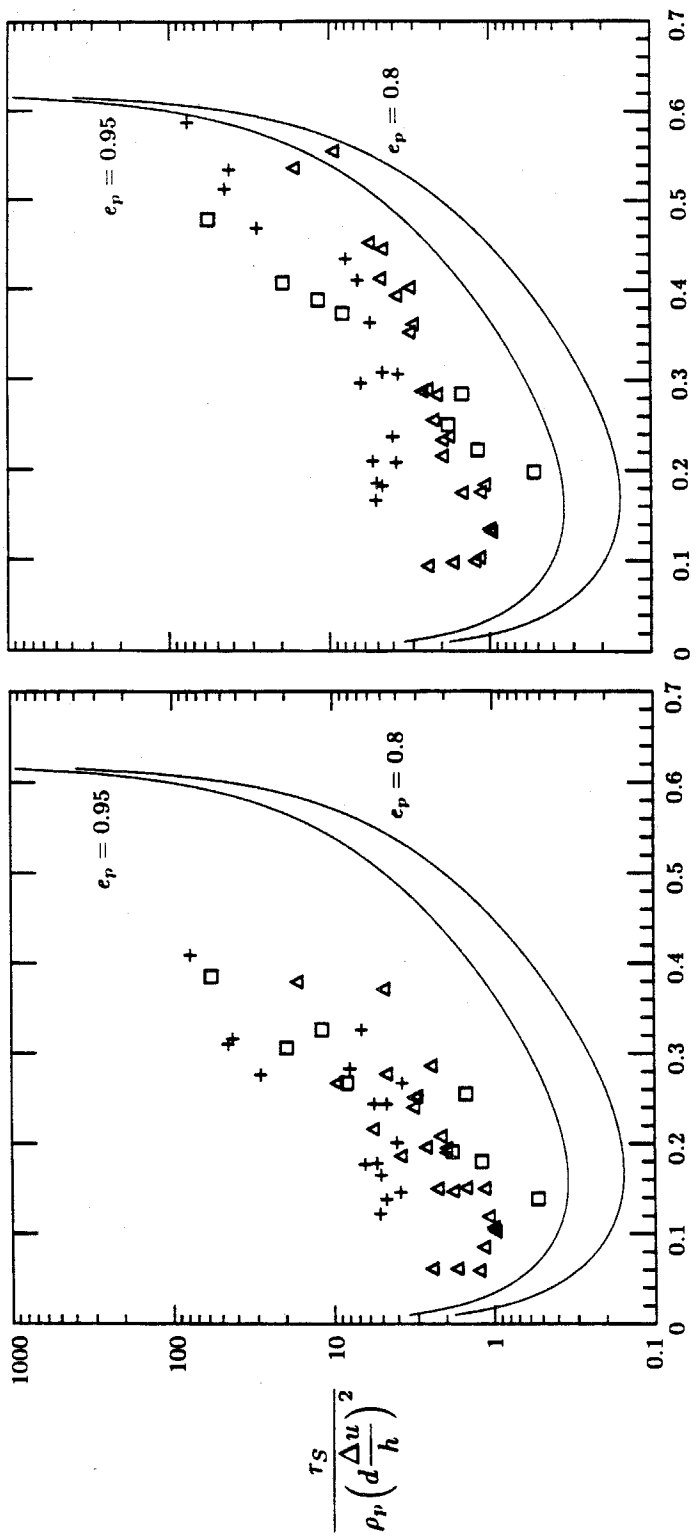

Figure 3.19. The normalized shear stress, $\tau_S/\rho_p(d\Delta u/h)^2$, against (a) wall solid fraction, ν_w, and (b) mean solid fraction, ν_m. □, the smooth surface; +, the moderately smooth surface; △, the rubberized surface. The solid lines, the results of Lun et al. [1984].

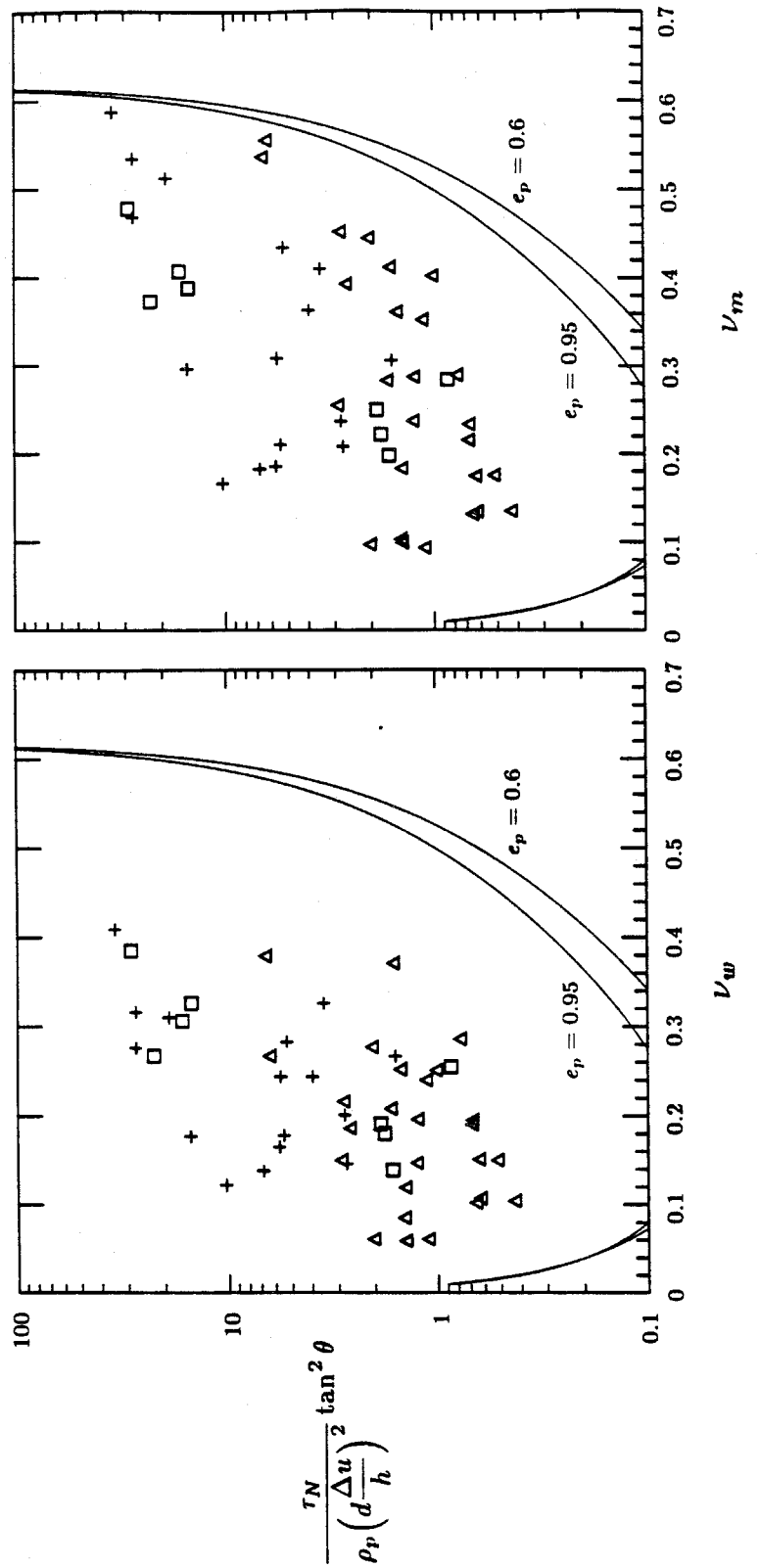

Figure 3.20. The normalized normal stress, $\tau_N \tan^2\theta/\rho_p(d\Delta u/h)^2$, against (a) wall solid fraction, ν_w, and (b) mean solid fraction, ν_m. □, the smooth surface; +, the moderately smooth surface; △, the rubberized surface. The solid lines, the results of Lun et al. [1984].

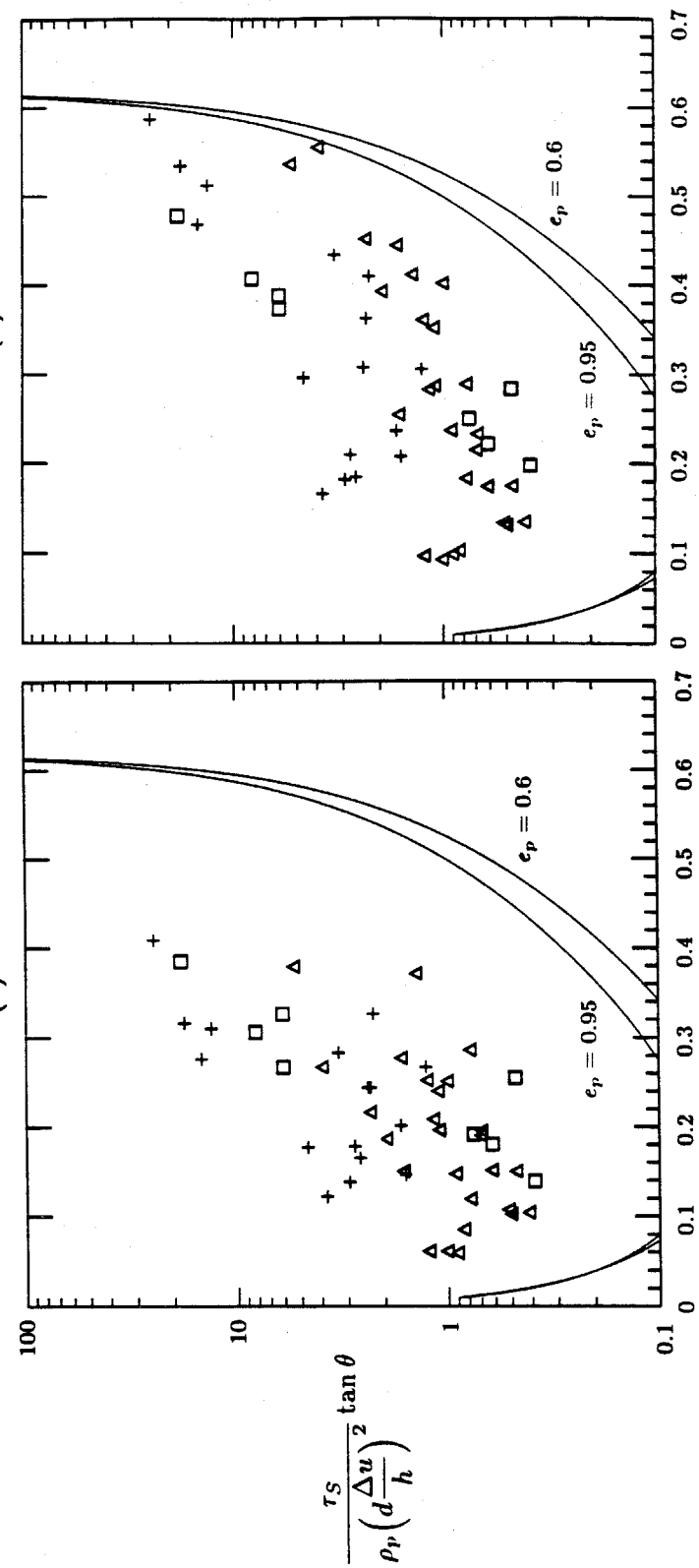

Figure 3.21. The normalized shear stress, $\tau_S \tan\theta/\rho_p(d\Delta u/h)^2$, against (a) wall solid fraction, ν_w, and (b) mean solid fraction, ν_m. □, the smooth surface; +, the moderately smooth surface; △, the rubberized surface. The solid lines, the results of Lun et al. [1984].

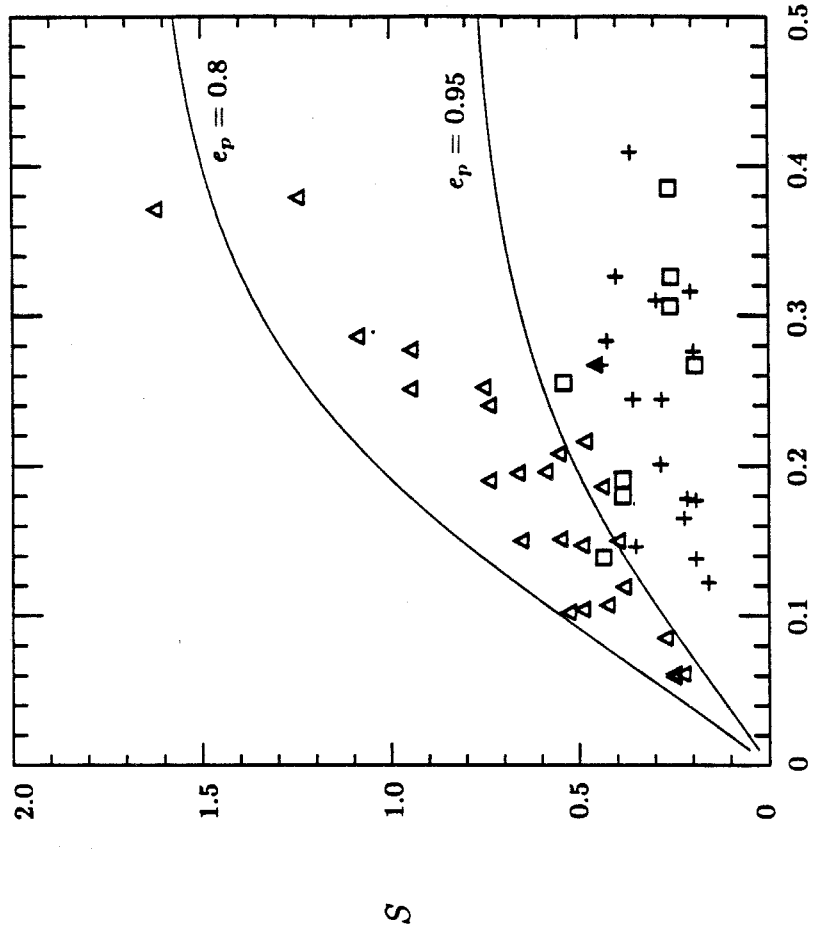

Figure 3.22. The parameter, $S = d(\Delta u/h)/u'_w$, against wall solid fraction, ν_w. □, the smooth surface; +, the moderately smooth surface; △, the rubberized surface. The solid lines, the results of Lun et al. [1984].

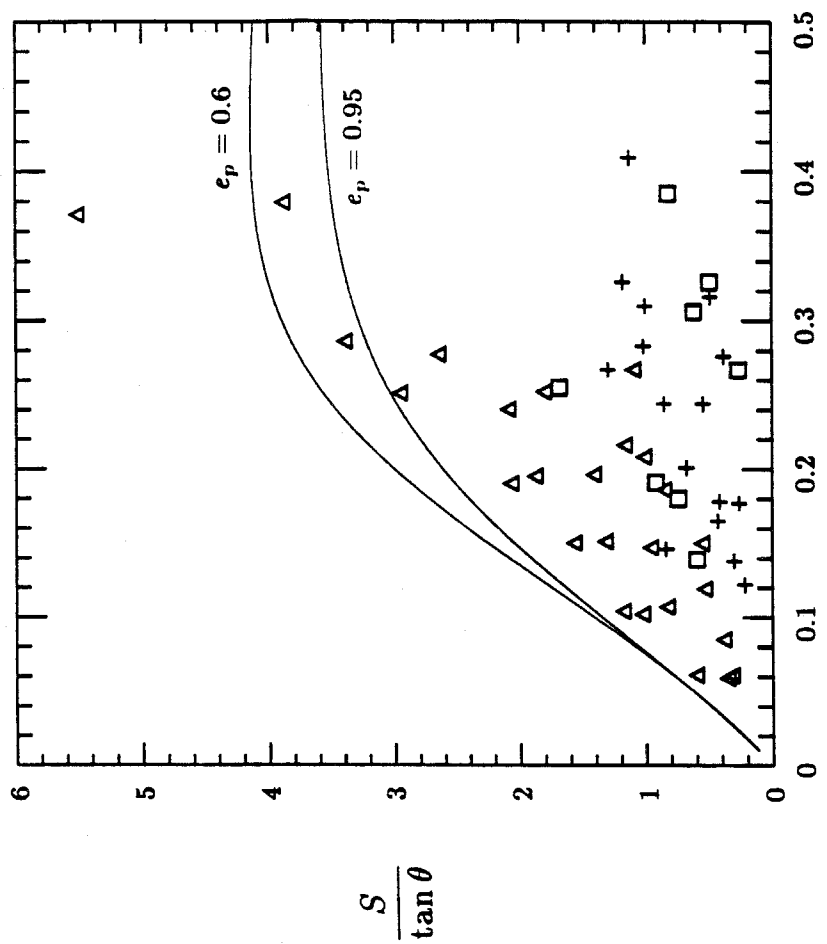

Figure 3.23. The parameter, $S/\tan\theta = d(\Delta u/h)/u'_w \tan\theta$, against wall solid fraction, ν_w. □, the smooth surface; +, the moderately smooth surface; △, the rubberized surface. The solid lines, the results of Lun et al. [1984].

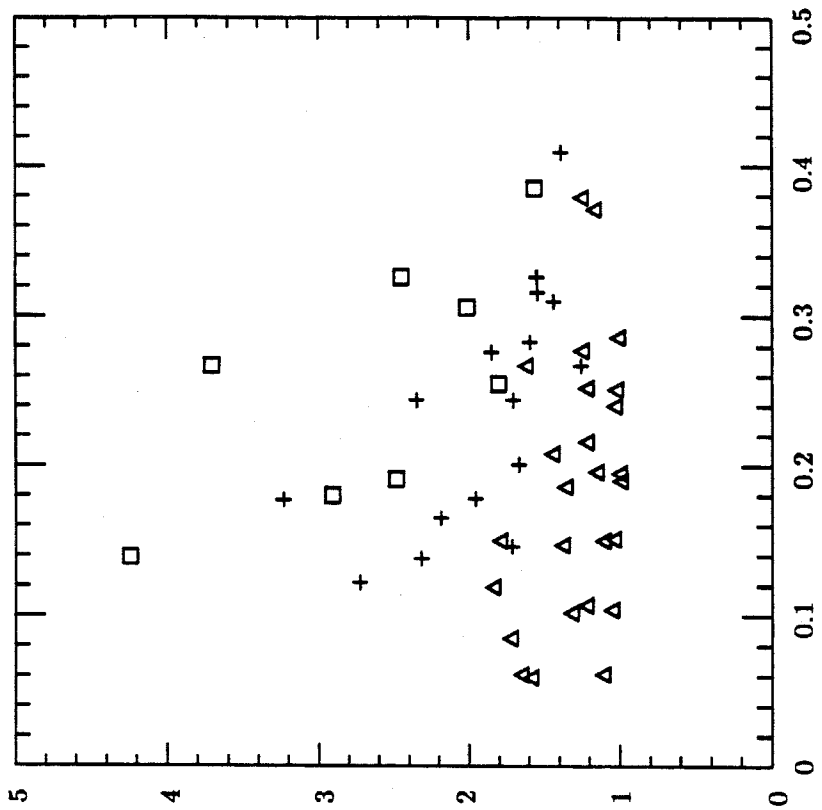

Figure 3.24. The ratio of $\tan\theta$ to f against wall solid fraction, ν_w. □, the smooth surface; +, the moderately smooth surface; △, the rubberized surface.

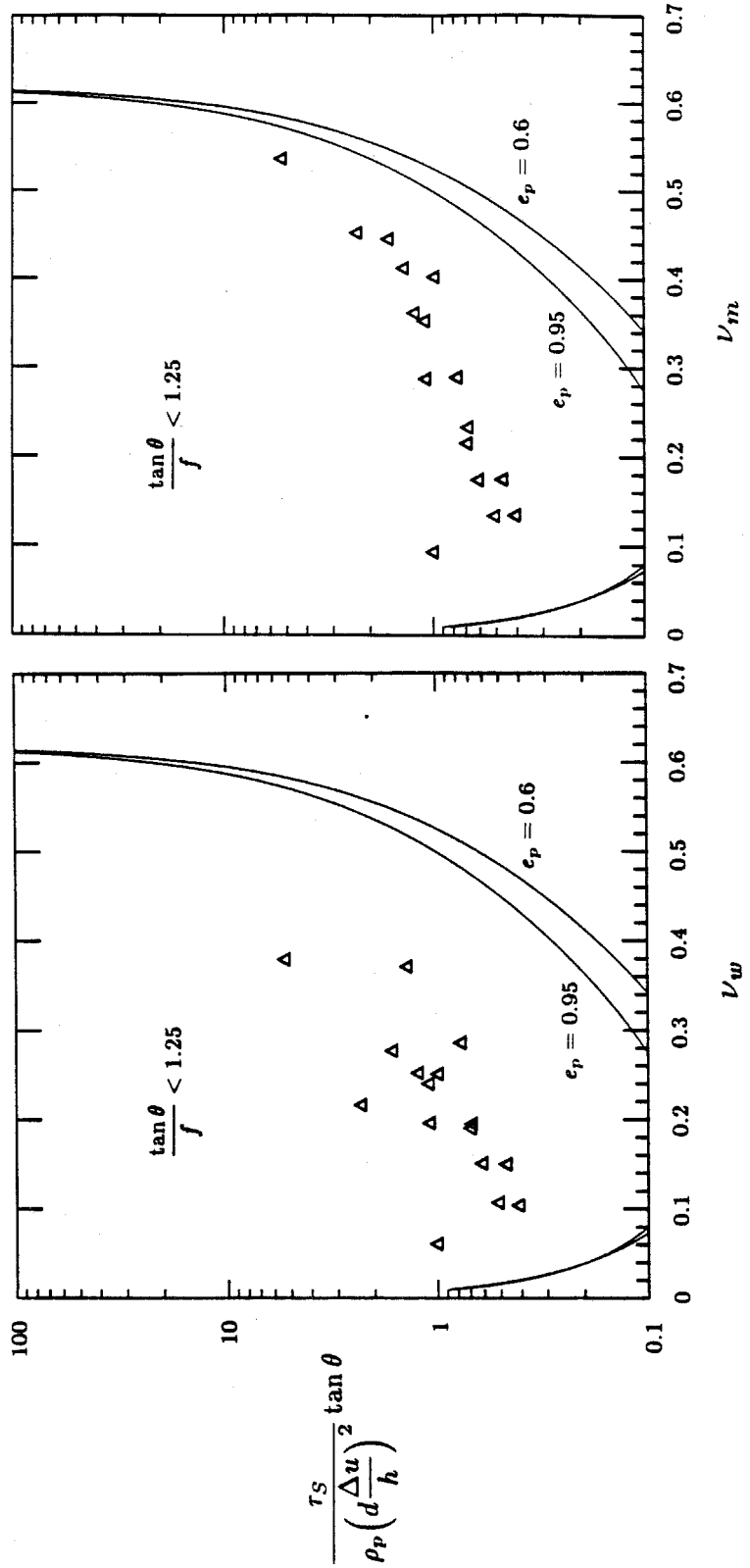

Figure 3.25. The normalized shear stress, $\tau_S \tan\theta/\rho_p(d\Delta u/h)^2$, against (a) wall solid fraction, ν_w, and (b) mean solid fraction, ν_m. Data only with $\tan\theta/f < 1.25$. The solid lines, the results of Lun et al. [1984].

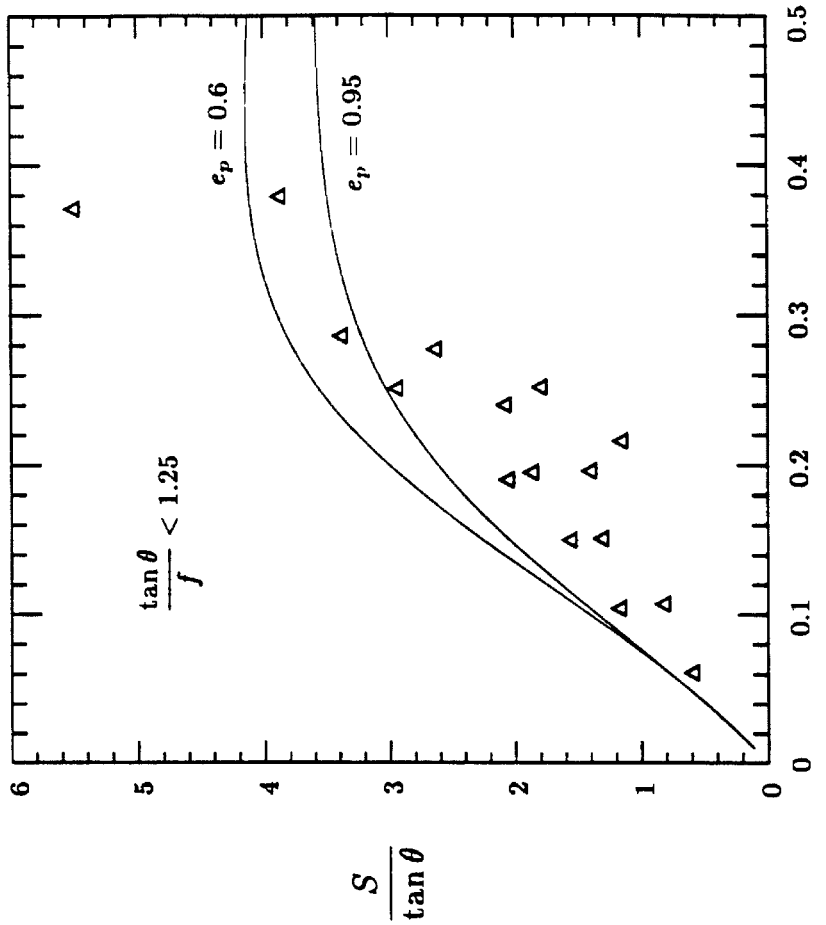

Figure 3.26. The parameter, $S/\tan\theta = d(\Delta u/h)/u'_w \tan\theta$, against wall solid fraction, ν_w. Data only with $\tan\theta/f < 1.25$. The solid lines, the results of Lun et al. [1984].

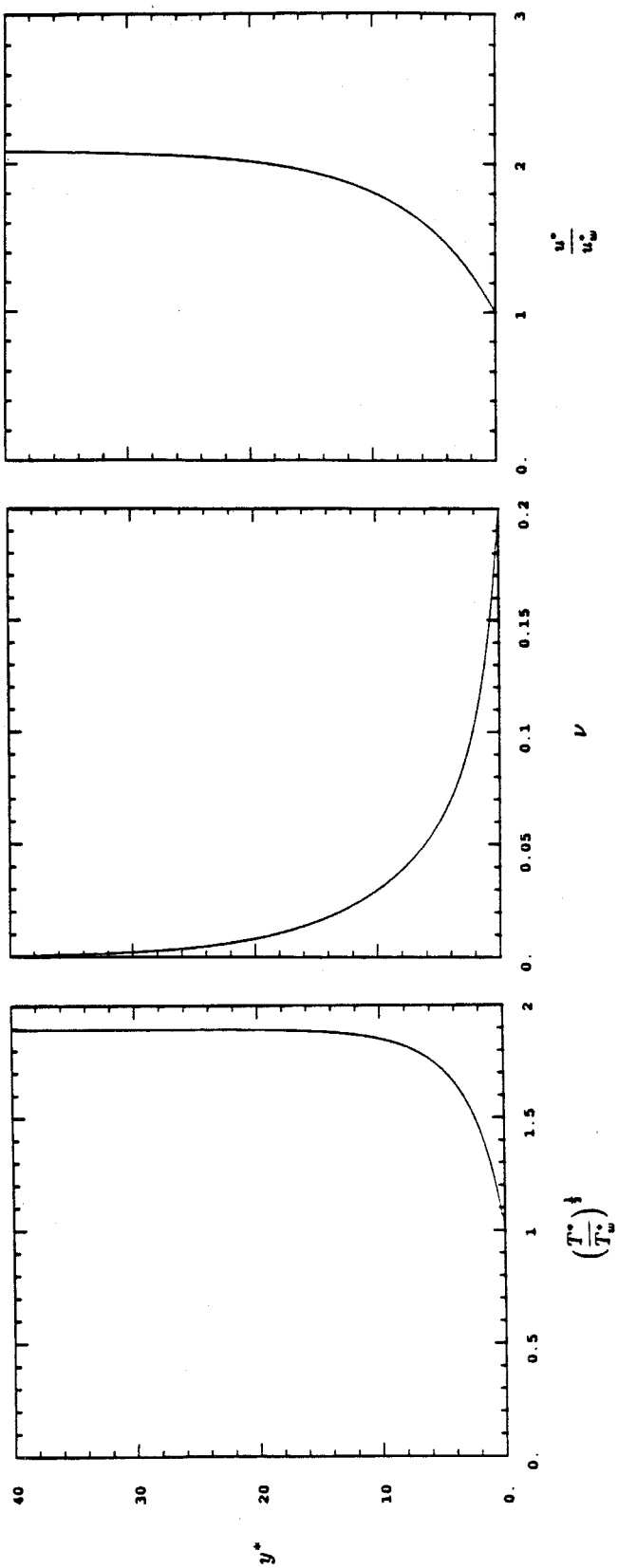

Figure 4.1. (a) Nondimensionalized square root of granular temperature, $(T^*/T_w^*)^{\frac{1}{2}}$, (b) solid fraction, ν, and (c) nondimensionalized mean velocity, u^*/u_w^*, against nondimensionalized distance from the chute base, y^*. Parameters; $e_p = 0.95$ and $\tan\theta = 0.4$. Boundary values at the wall; $T_w^* = 2$, $\nu_w = 0.2$, and $u_w^* = 10$.

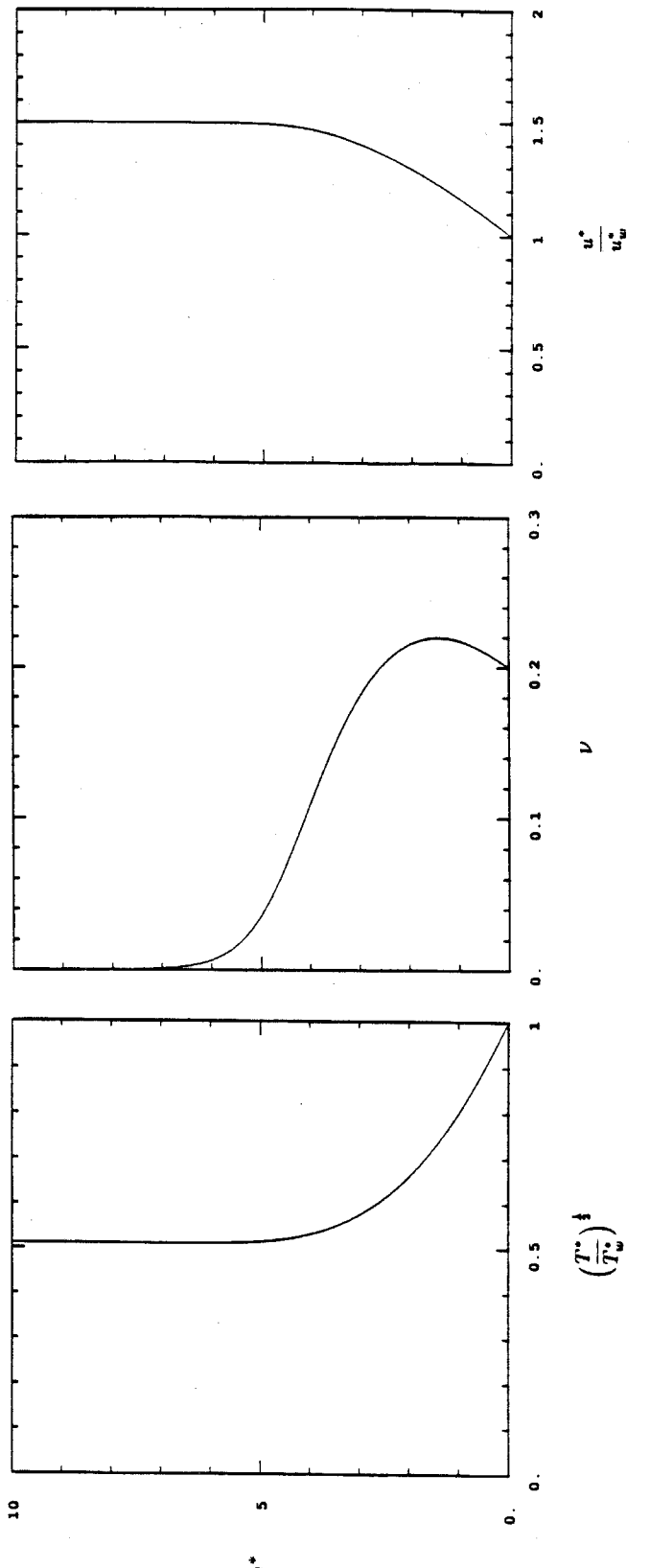

Figure 4.2. (a) Nondimensionalized square root of granular temperature, $(T^*/T_w^*)^{\frac{1}{2}}$, (b) solid fraction, ν, and (c) nondimensionalized mean velocity, u^*/u_w^*, against nondimensionalized distance from the chute base, y^*. Parameters; $e_p = 0.6$ and $\tan\theta = 0.4$. Boundary values at the wall; $T_w^* = 2$, $\nu_w = 0.2$, and $u_w^* = 10$.

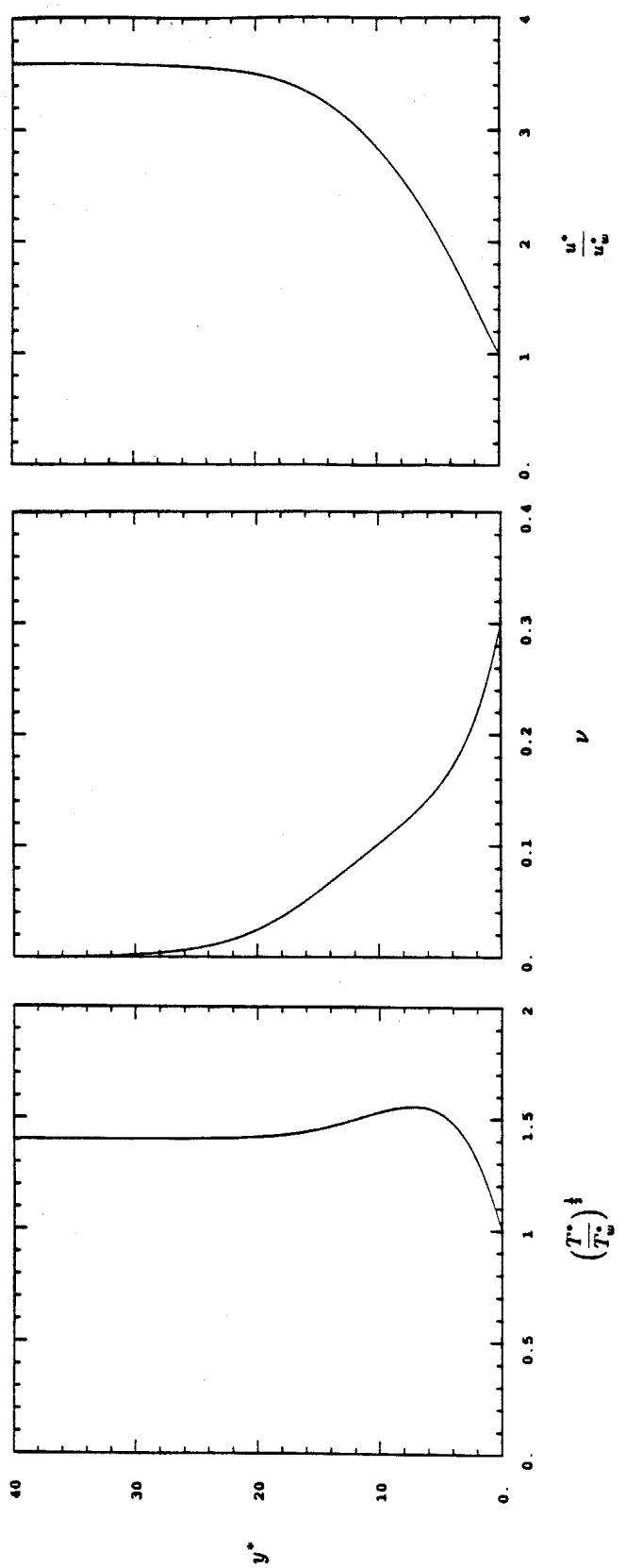

Figure 4.3. (a) Nondimensionalized square root of granular temperature, $(T^*/T_w^*)^{\frac{1}{2}}$, (b) solid fraction, ν, and (c) nondimensionalized mean velocity, u^*/u_w^*, against nondimensionalized distance from the chute base, y^*. Parameters; $e_p = 0.9$ and $\tan\theta = 0.4$. Boundary values at the wall; $T_w^* = 2$, $\nu_w = 0.3$, and $u_w^* = 10$.

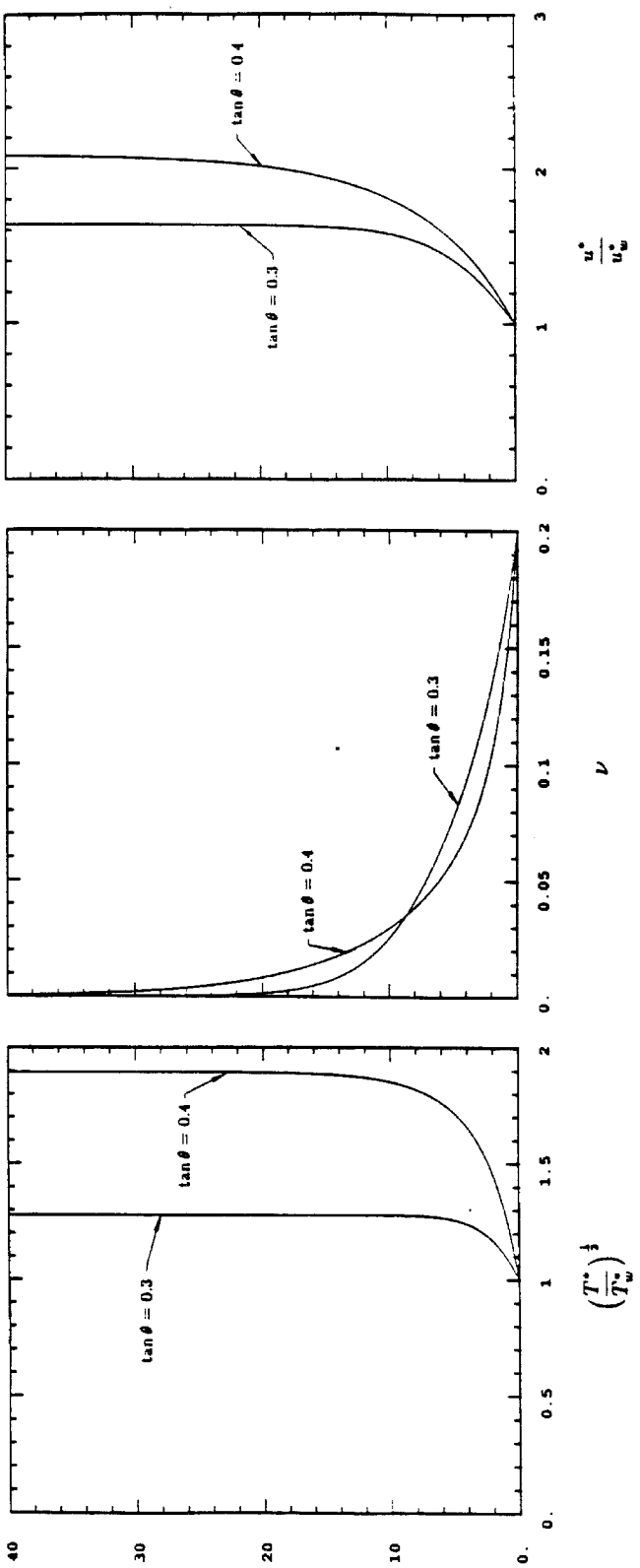

Figure 4.4. The effect of the variation of the chute inclination angle. (a) Nondimensionalized square root of granular temperature, $(T^*/T_w^*)^{\frac{1}{2}}$, (b) solid fraction, ν, and (c) nondimensionalized mean velocity, u^*/u_w^*, against nondimensionalized distance from the chute base, y^*. Parameters; $e_p = 0.95$, $\tan\theta = 0.3$ and 0.4. Boundary values at the wall; $T_w^* = 2$, $\nu_w = 0.2$, and $u_w^* = 10$.

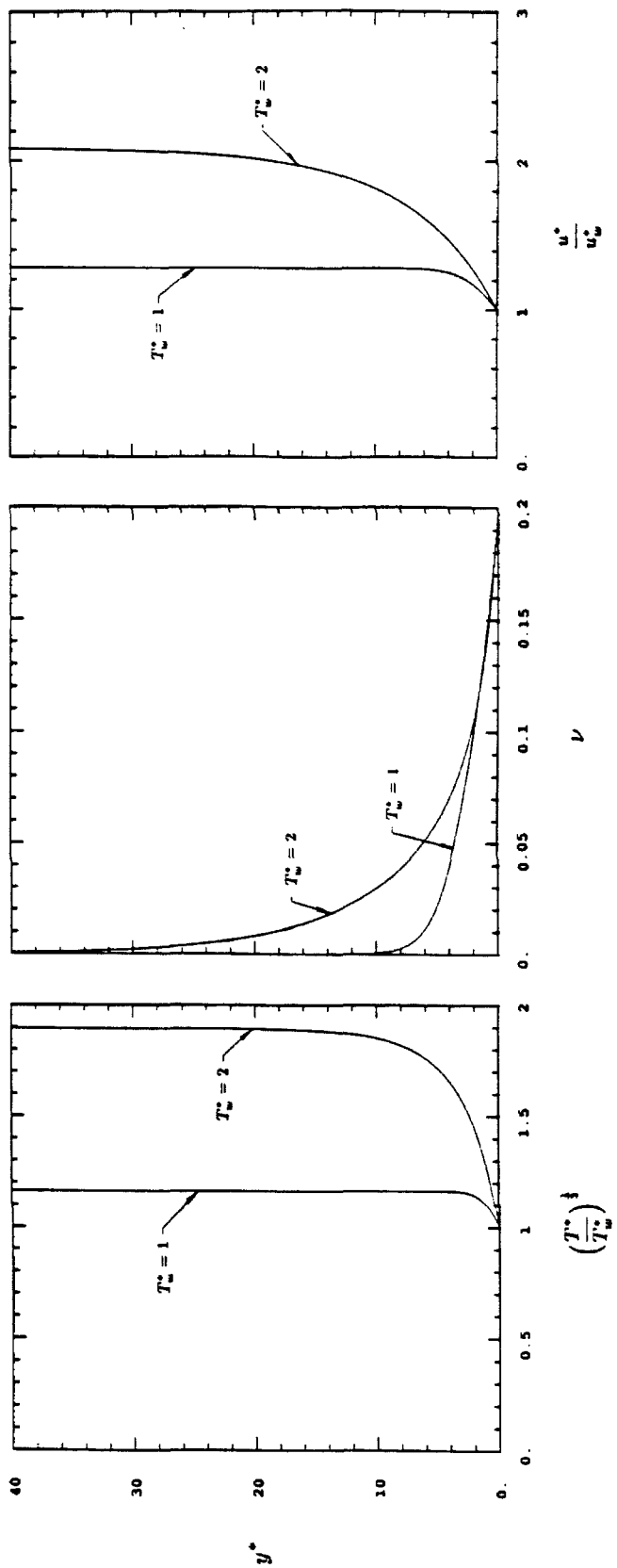

Figure 4.5. The effect of the variation of granular temperature at the wall. (a) Nondimensionalized square root of granular temperature, $(T^*/T_w^*)^{\frac{1}{2}}$, (b) solid fraction, ν, and (c) nondimensionalized mean velocity, u^*/u_w^*, against nondimensionalized distance from the chute base, y^*. Parameters; $e_p = 0.95$ and $\tan\theta = 0.4$. Boundary values at the wall; $T_w^* = 1$ and 2, $\nu_w = 0.2$, and $u_w^* = 10$.

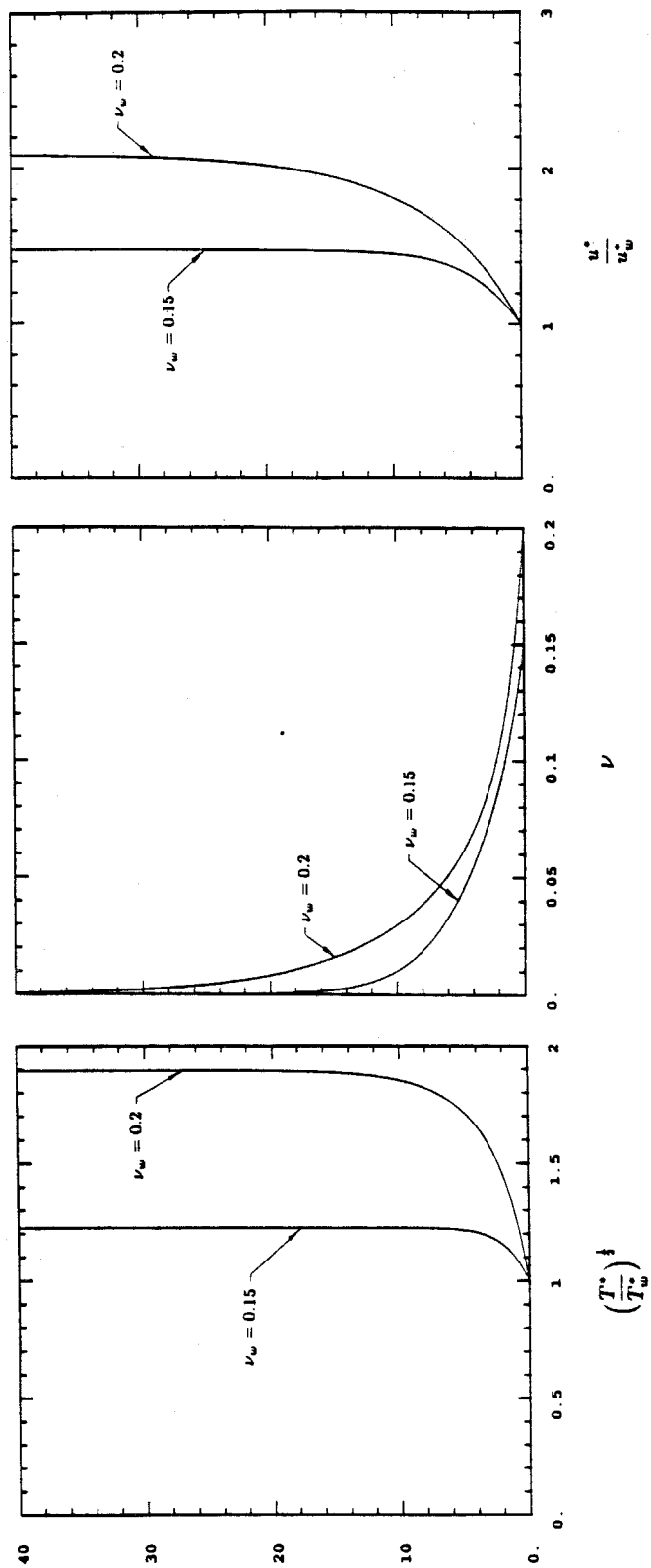

Figure 4.6. The effect of the variation of solid fraction at the wall. (a) Nondimensionalized square root of granular temperature, $(T^*/T_w^*)^{\frac{1}{2}}$, (b) solid fraction, ν, and (c) nondimensionalized mean velocity, u^*/u_w^*, against nondimensionalized distance from the chute base, y^*. Parameters; $e_p = 0.95$ and $\tan\theta = 0.4$. Boundary values at the wall; $T_w^* = 2$, $\nu_w = 0.15$ and 0.2, and $u_w^* = 10$.

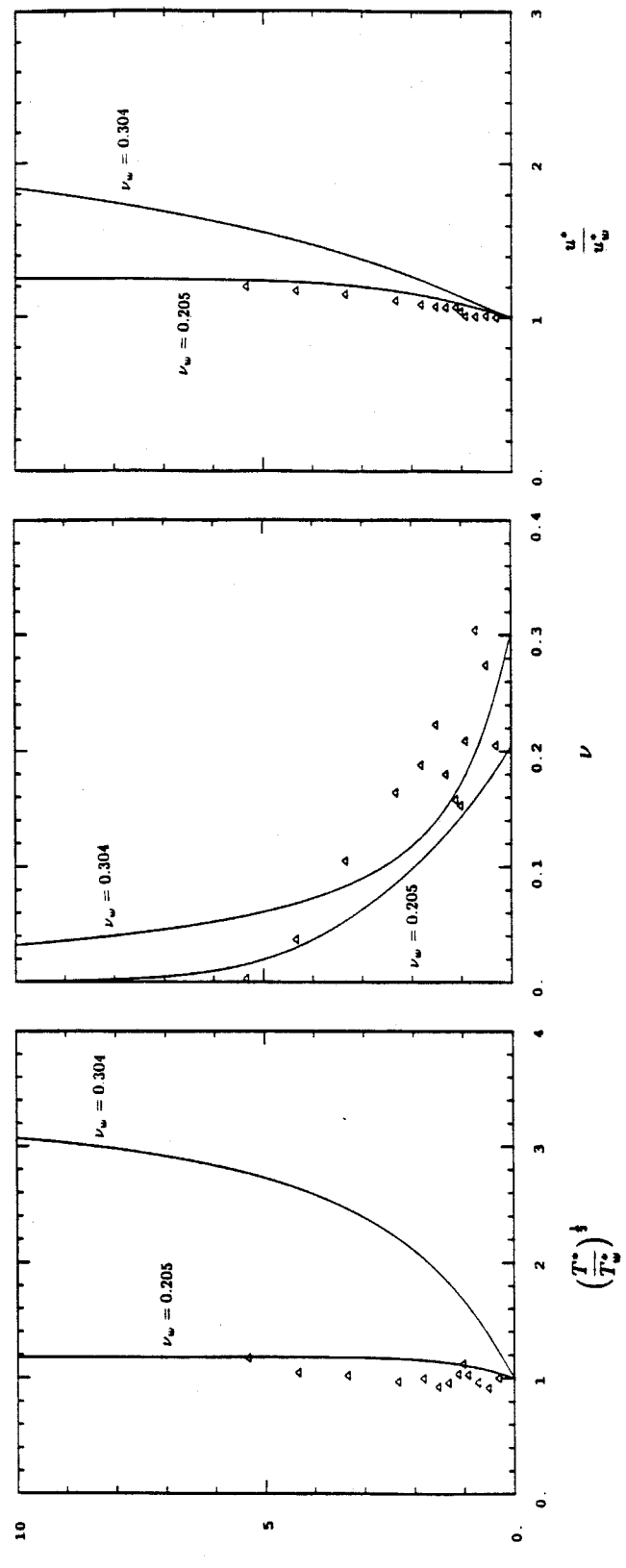

Figure 4.7. Comparison with the experimental data of Ahn et al. [1989a]. The smooth aluminum surface used for the chute base, and $d = 1.26$ mm. $\triangle$, data from the experiment. Solid line, results of the present analysis. (a) Nondimensionalized square root of granular temperature, $(T^*/T_w^*)^{\frac{1}{2}}$, (b) solid fraction, ν, and (c) nondimensionalized mean velocity, u^*/u_w^*, against nondimensionalized distance from the chute base, y^*. Parameters; $e_p = 0.95$ and $\tan\theta = 0.418$. Boundary values at the wall; $T_w^* = 0.935$, $\nu_w = 0.205$ and 0.304, and $u_w^* = 11.3$.

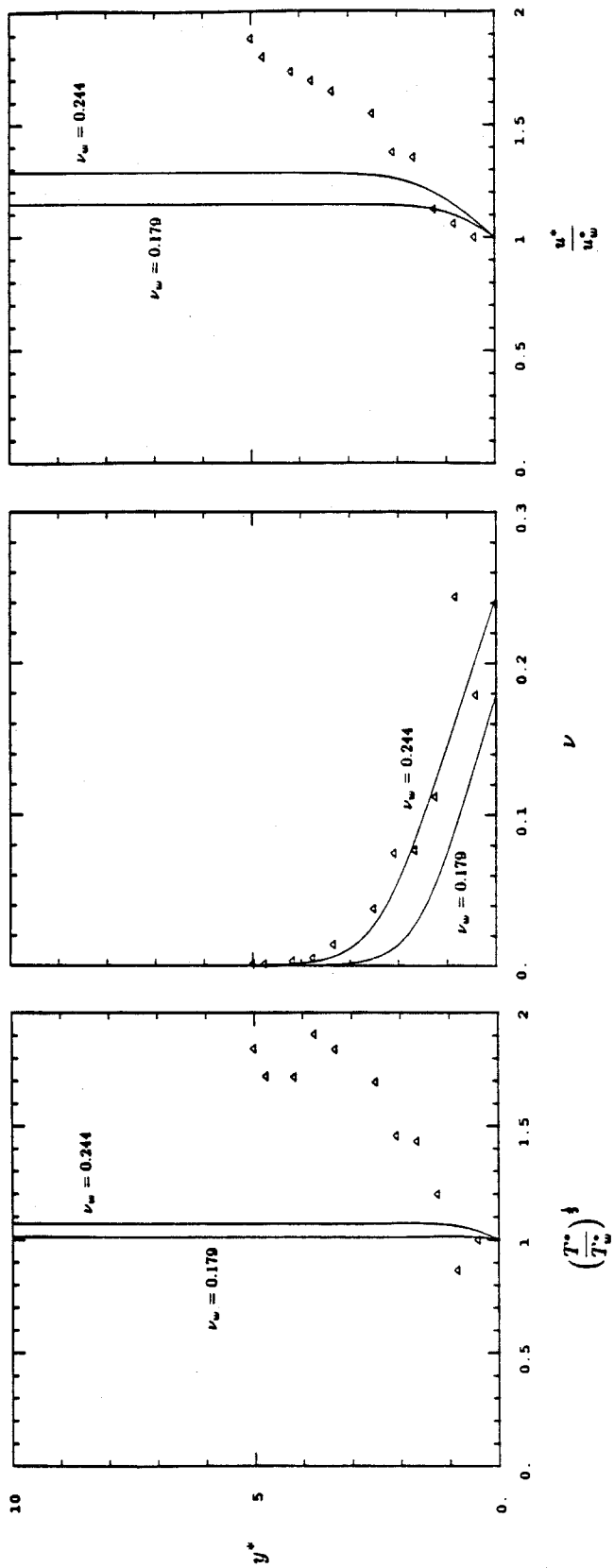

Figure 4.8. Comparison with the experimental data of Ahn et al. [1989a]. The rubber-coated surface used for the chute base, and $d = 3.04$ mm. $\triangle$, data from the experiment. Solid line, results of the present analysis. (a) Nondimensionalized square root of granular temperature, $(T^*/T_w^*)^{\frac{1}{2}}$, (b) solid fraction, ν, and (c) nondimensionalized mean velocity, u^*/u_w^*, against nondimensionalized distance from the chute base, y^*. Parameters; $e_p = 0.95$ and $\tan\theta = 0.418$. Boundary values at the wall; $T_w^* = 0.440$, $\nu_w = 0.179$ and 0.244, and $u_w^* = 4.39$.

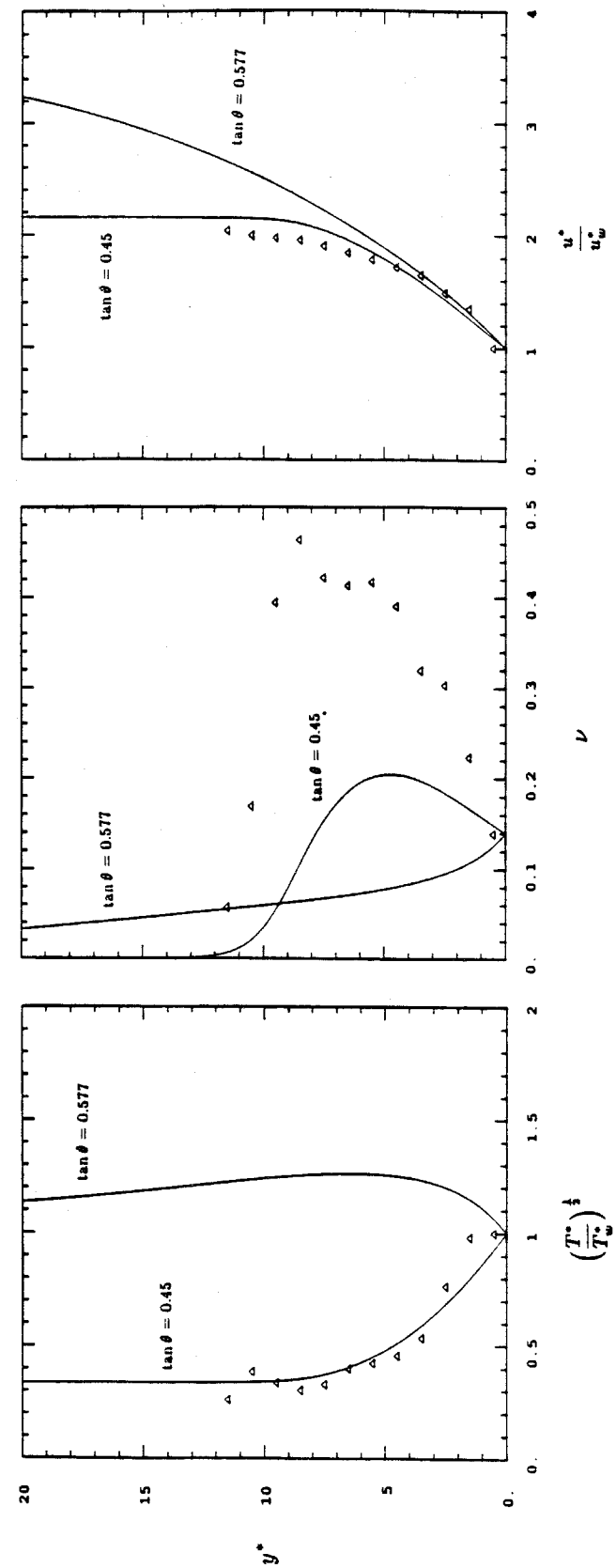

Figure 4.9. Comparison with the computer simulations by Campbell and Brennen [1985b]. △, data from the computer simulations. Type A simulation with $\theta = 30°$, $e_p = 0.6$, and $e_w = 0.8$. Solid line, results of the present analysis. Parameters; $e_p = 0.6$, and $\tan\theta = 0.577$ and 0.45. Boundary values at the wall; $T_w^* = 7.00$, $\nu_w = 0.140$, and $u_w^* = 14.0$. (a) Nondimensionalized square root of granular temperature, $(T^*/T_w^*)^{\frac{1}{2}}$, (b) solid fraction, ν, and (c) nondimensionalized mean velocity, u^*/u_w^*, against nondimensionalized distance from the chute base, y^*.

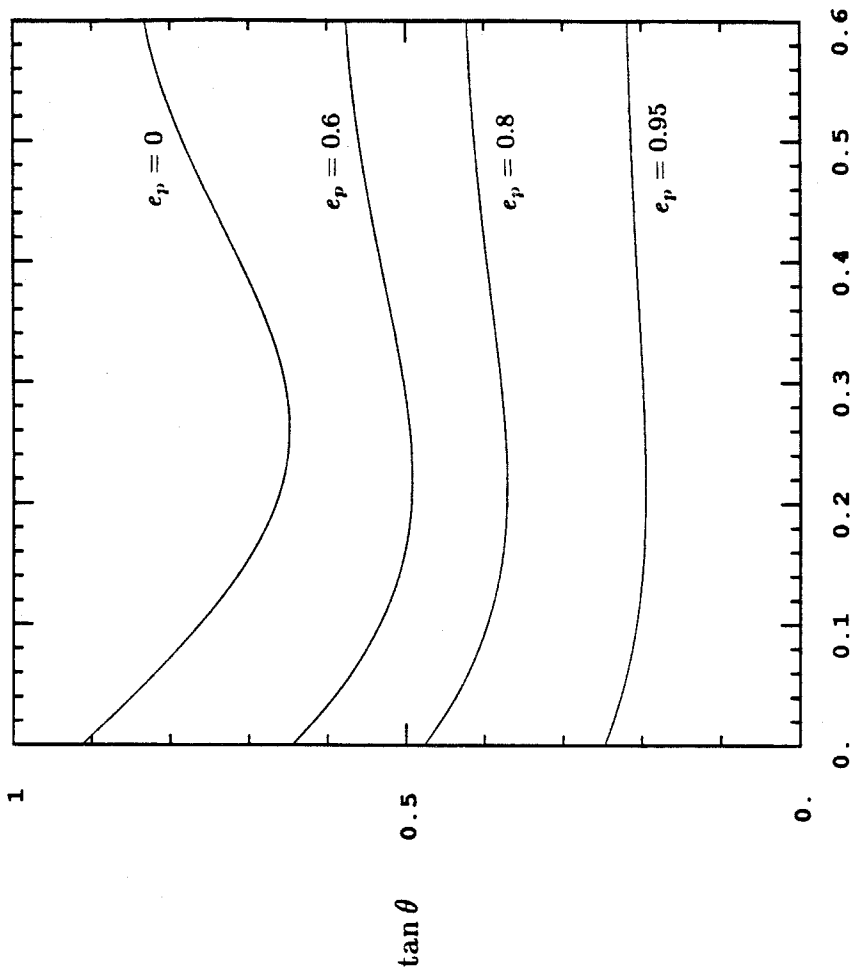

Figure 4.10. Zeros of the granular conduction term for various e_p.

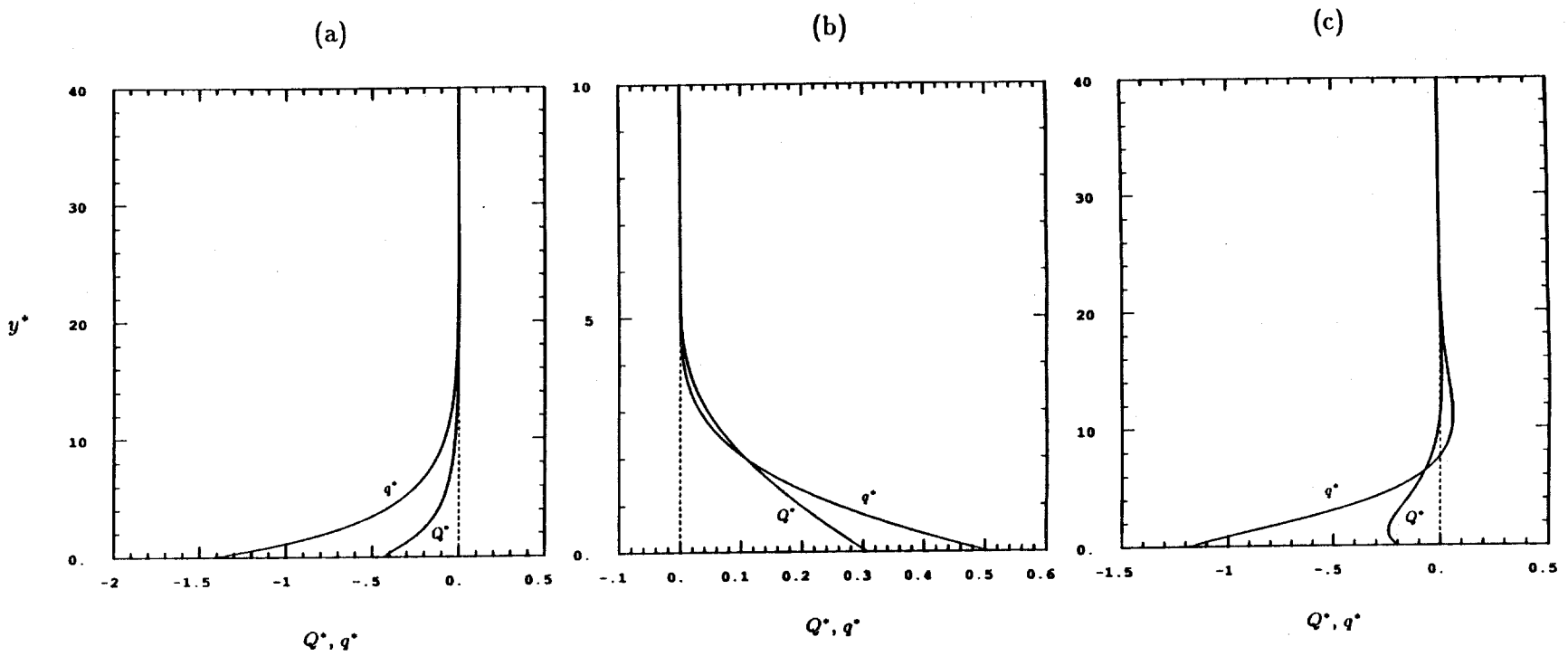

Figure 4.11. Nondimensionalized granular conduction, Q^*, and fluctuation energy flux, q^*, against nondimensionalized distance from the chute base, y^*. Parameters and boundary values at the wall; (a) as in Figure 4.1, (b) as in Figure 4.2, and (c) as in Figure 4.3.

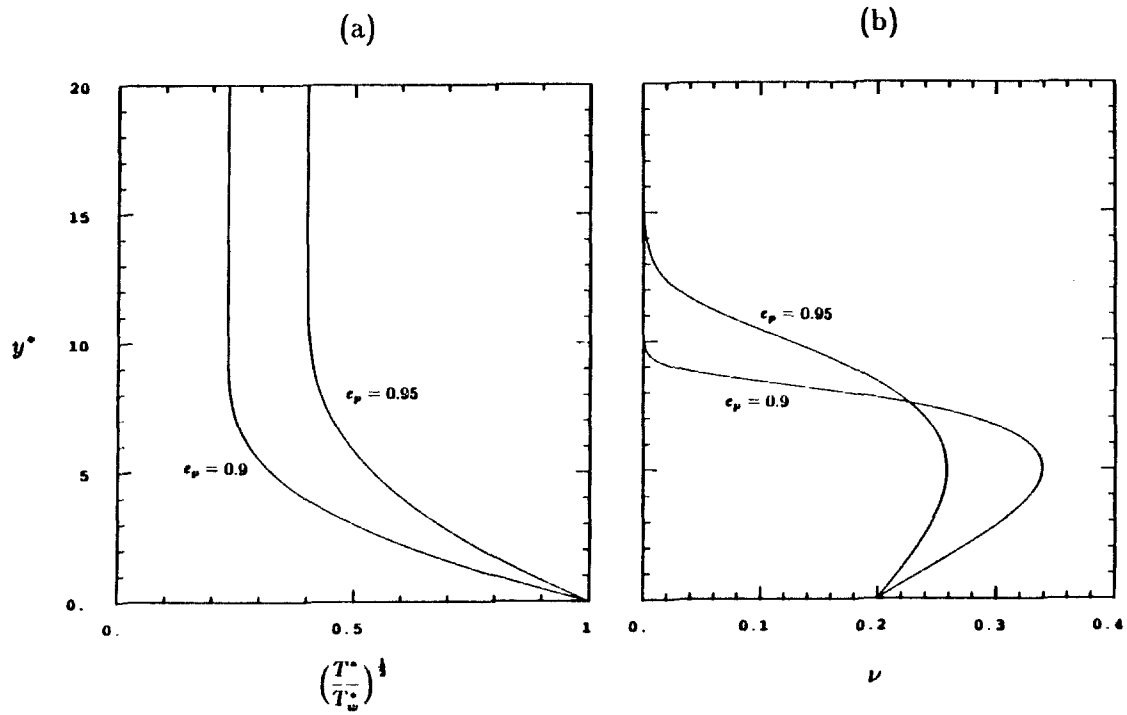

Figure 4.12. The study of the case in which no shear motion and mean velocity exist. (a) Nondimensionalized square root of granular temperature, $(T^*/T_w^*)^{\frac{1}{2}}$, and (b) solid fraction, ν, against nondimensionalized distance from the chute base, y^*. Parameters; $e_p = 0.9$ and 0.95, and $\tan\theta = 0$. Boundary values at the wall; $T_w^* = 5$ and $\nu_w = 0.2$.

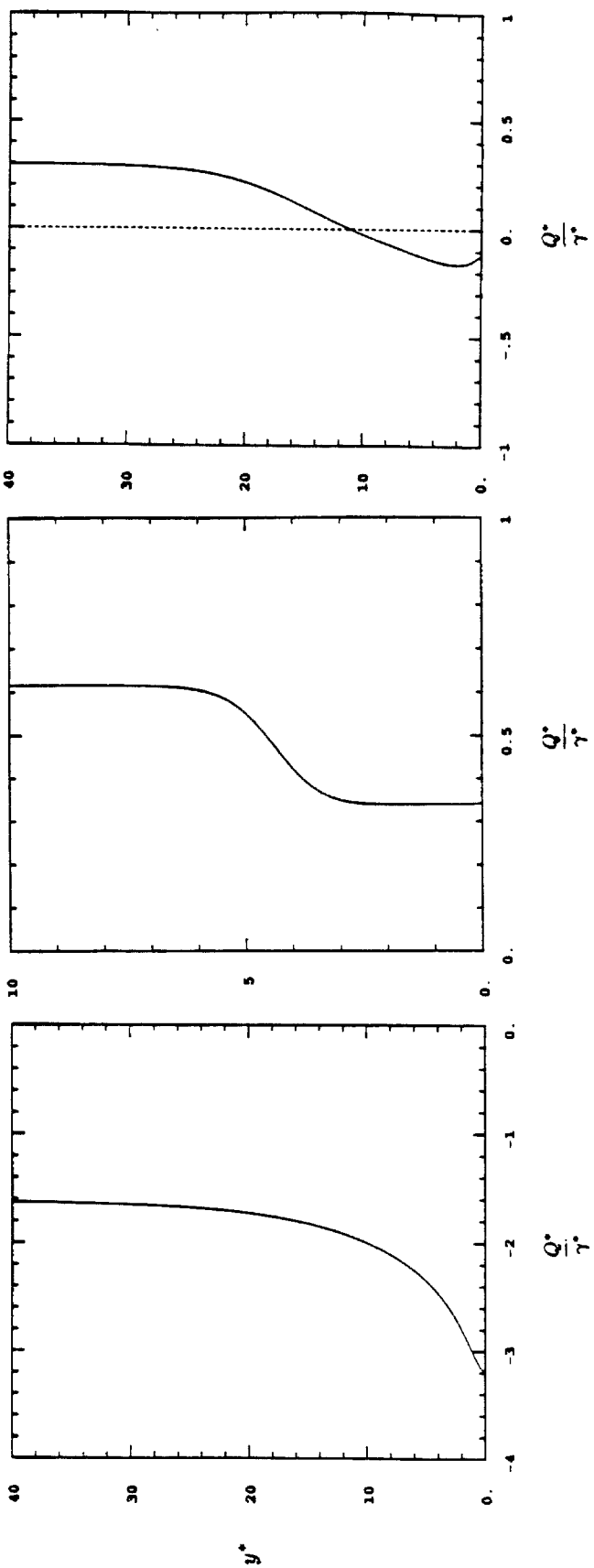

Figure 4.13. The ratio of granular conduction to dissipation, Q^*/γ^*, against nondimensionalized distance from the chute base, y^*. Parameters and boundary values at the wall; (a) as in Figure 4.1, (b) as in Figure 4.2, and (c) as in Figure 4.3.

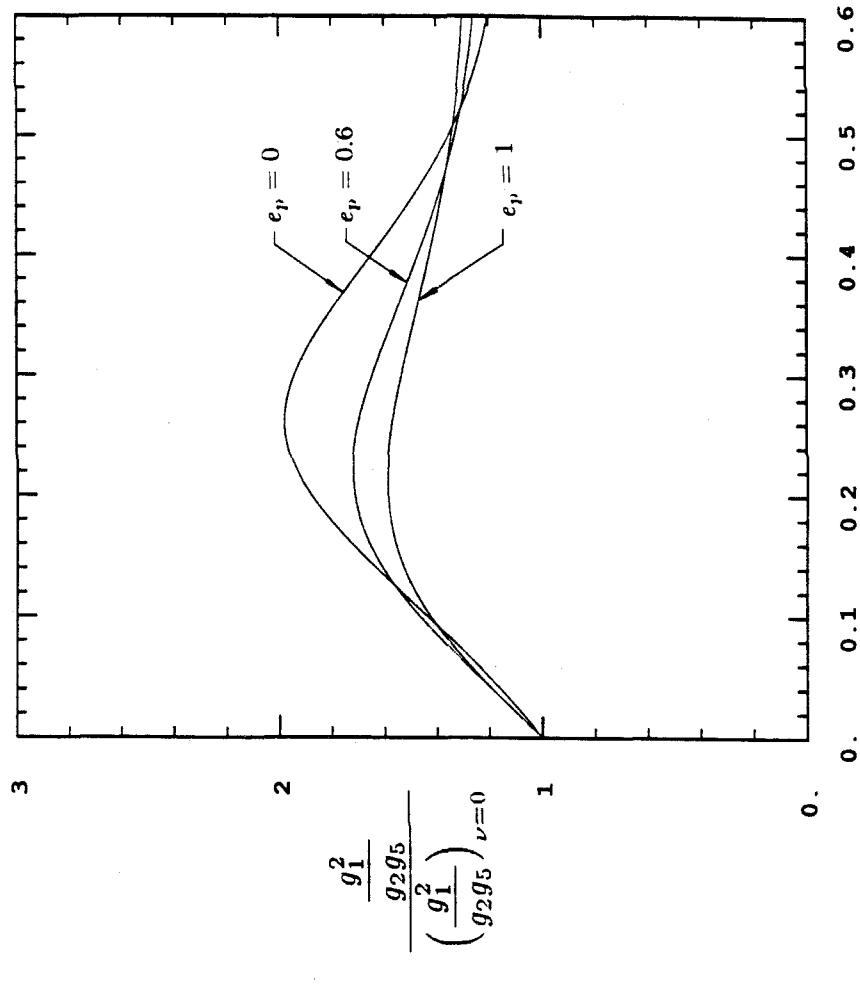

Figure 4.14. The function g_1^2/g_2g_5 for various e_p, normalized by g_1^2/g_2g_5 at $\nu = 0$.

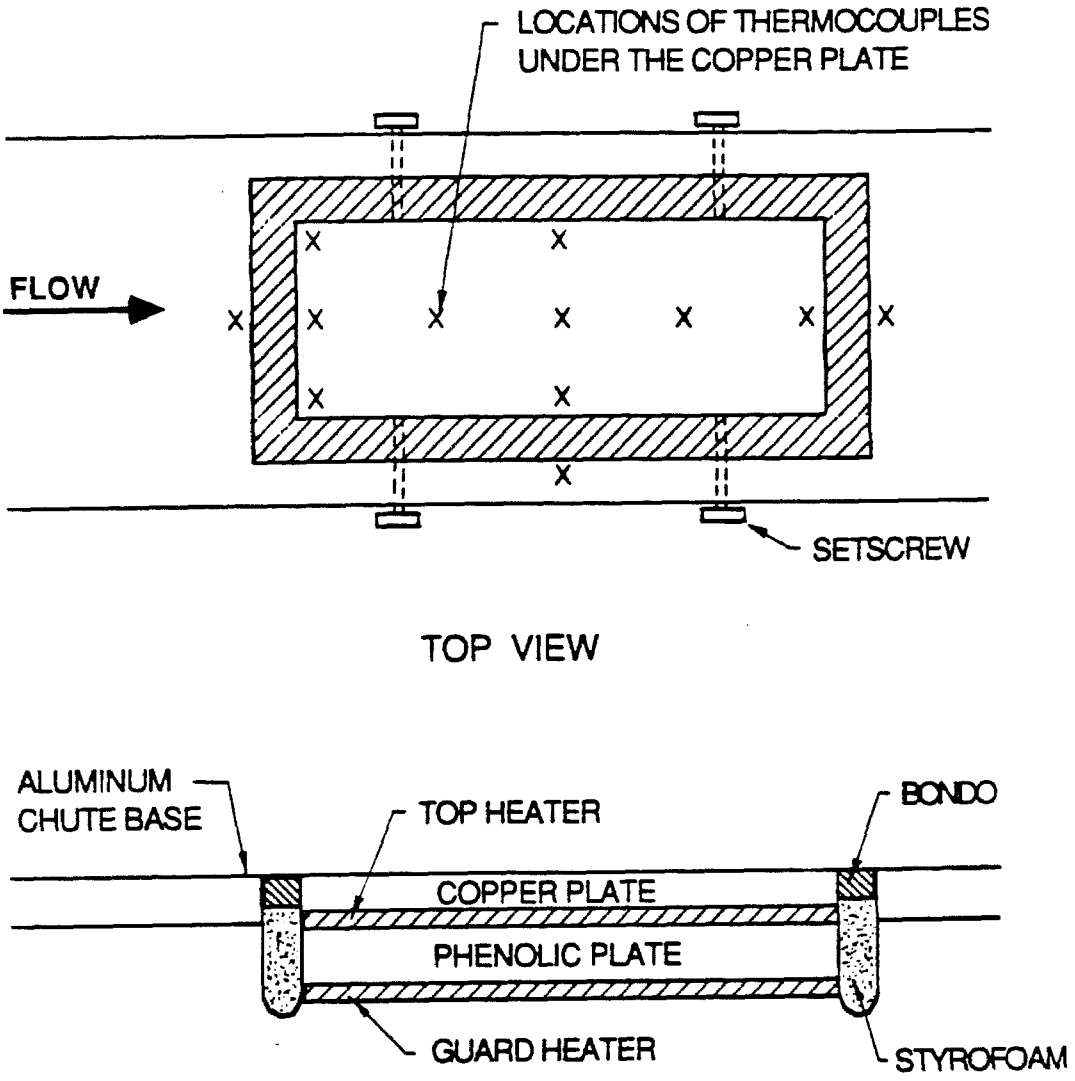

Figure 5.1. Schematic of the heating plate.

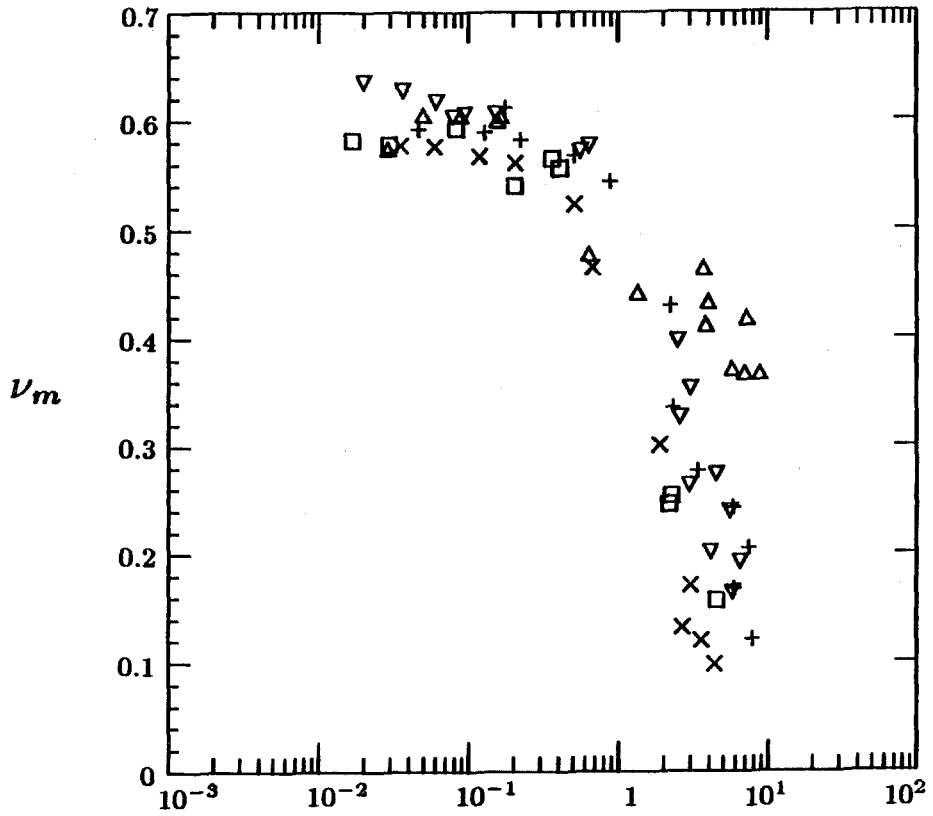

Figure 5.2. The mean solid fraction, ν_m, against the Froude number, Fr. □, 3.04 mm glass beads; +, 1.26 mm glass beads; △, 0.50 mm glass beads; ×, 3.15 mm polystyrene beads; ▽, 2.22 mm mustard seeds.

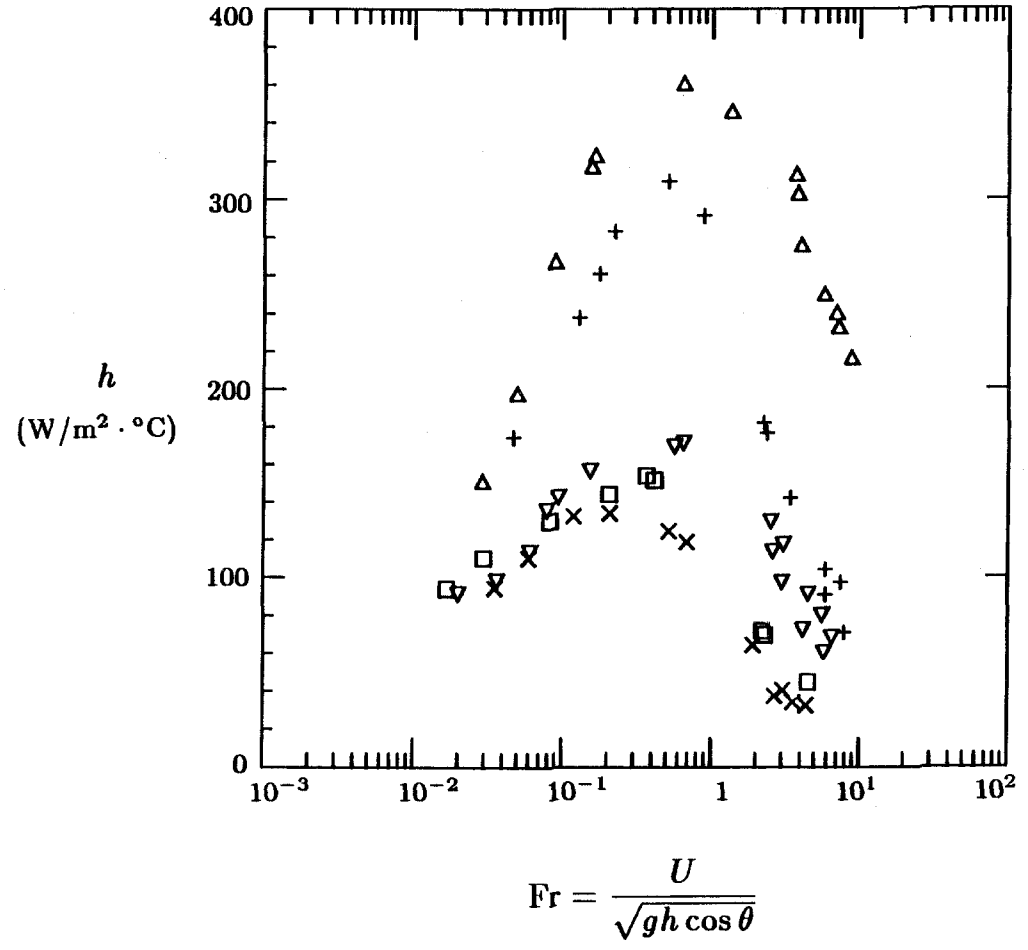

Figure 5.3. The heat transfer coefficient, h, against the Froude number, Fr. □, 3.04 mm glass beads; +, 1.26 mm glass beads; △, 0.50 mm glass beads; ×, 3.15 mm polystyrene beads; ▽, 2.22 mm mustard seeds.

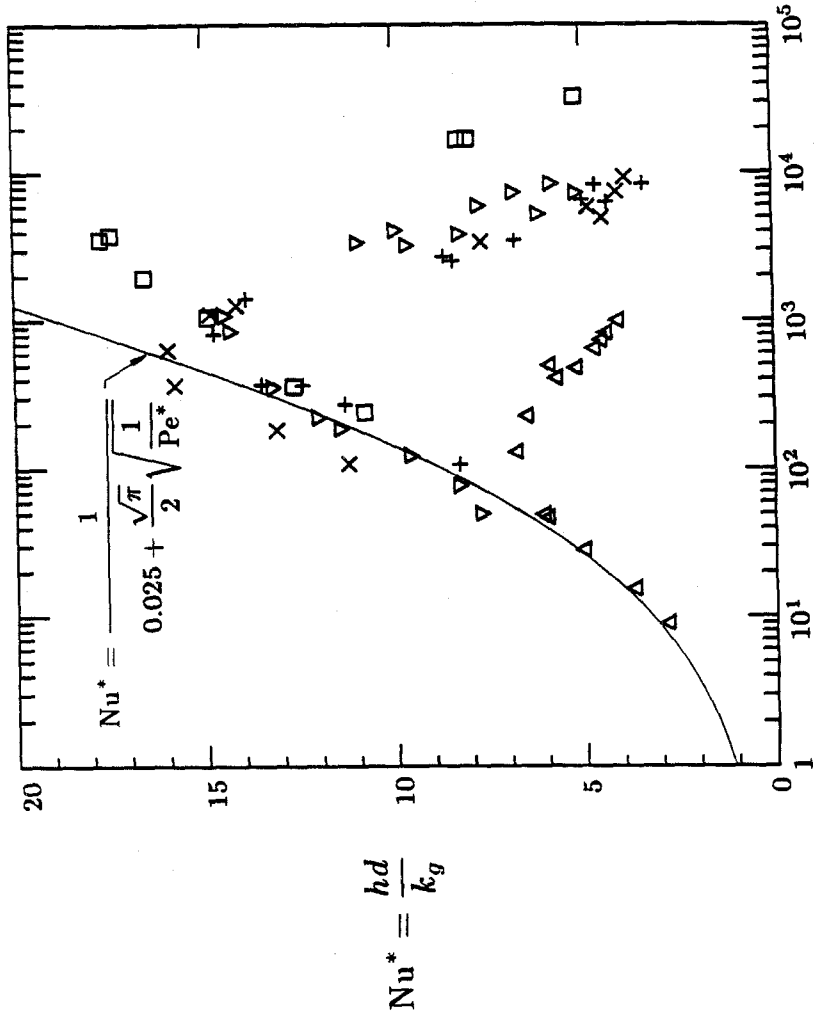

Figure 5.4. The modified Nusselt number, Nu^*, against the modified Peclet number, Pe^*. The curve is from equation (5.3). □, 3.04 mm glass beads; +, 1.26 mm glass beads; △, 0.50 mm glass beads; ×, 3.15 mm polystyrene beads; ▽, 2.22 mm mustard seeds.

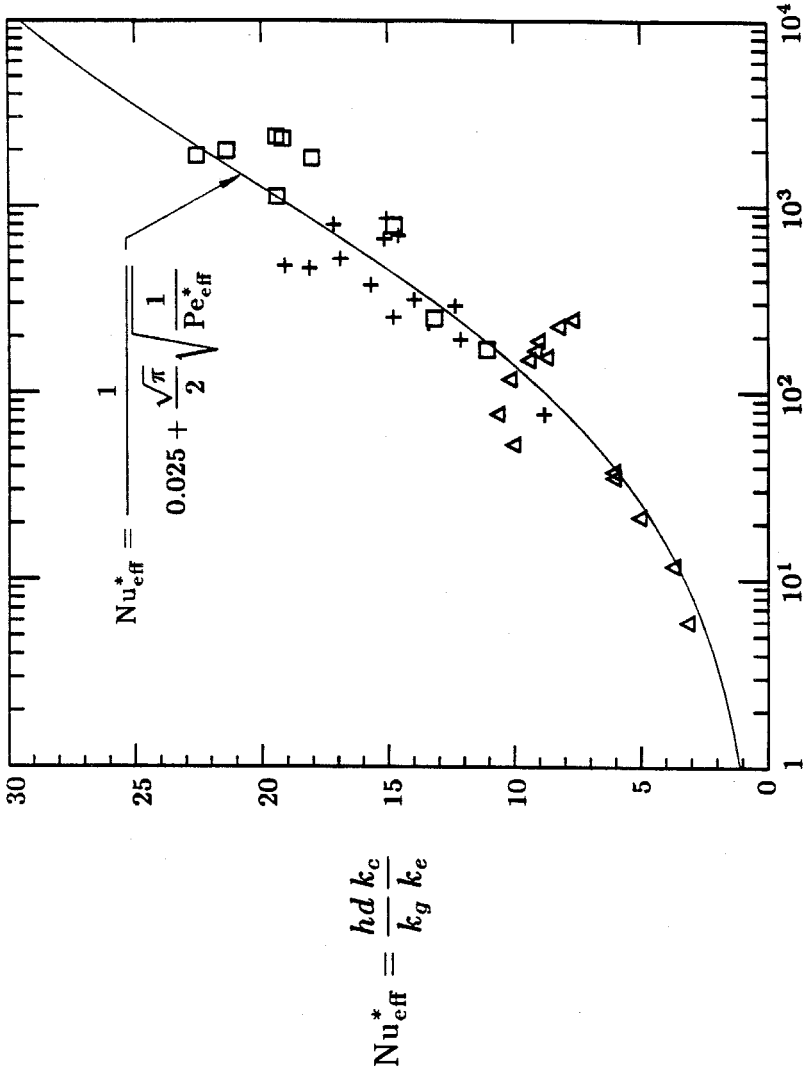

$$\mathrm{Pe}^*_{\mathrm{eff}} = \frac{UL}{\alpha_e}\left(\frac{d}{L}\right)^2\left(\frac{k_e}{k_g}\right)$$

Figure 5.5. The effective Nusselt number, $\mathrm{Nu}^*_{\mathrm{eff}}$, against the effective Peclet number, $\mathrm{Pe}^*_{\mathrm{eff}}$. The curve is from equation (5.7). □, 3.04 mm glass beads; +, 1.26 mm glass beads; △, 0.50 mm glass beads;

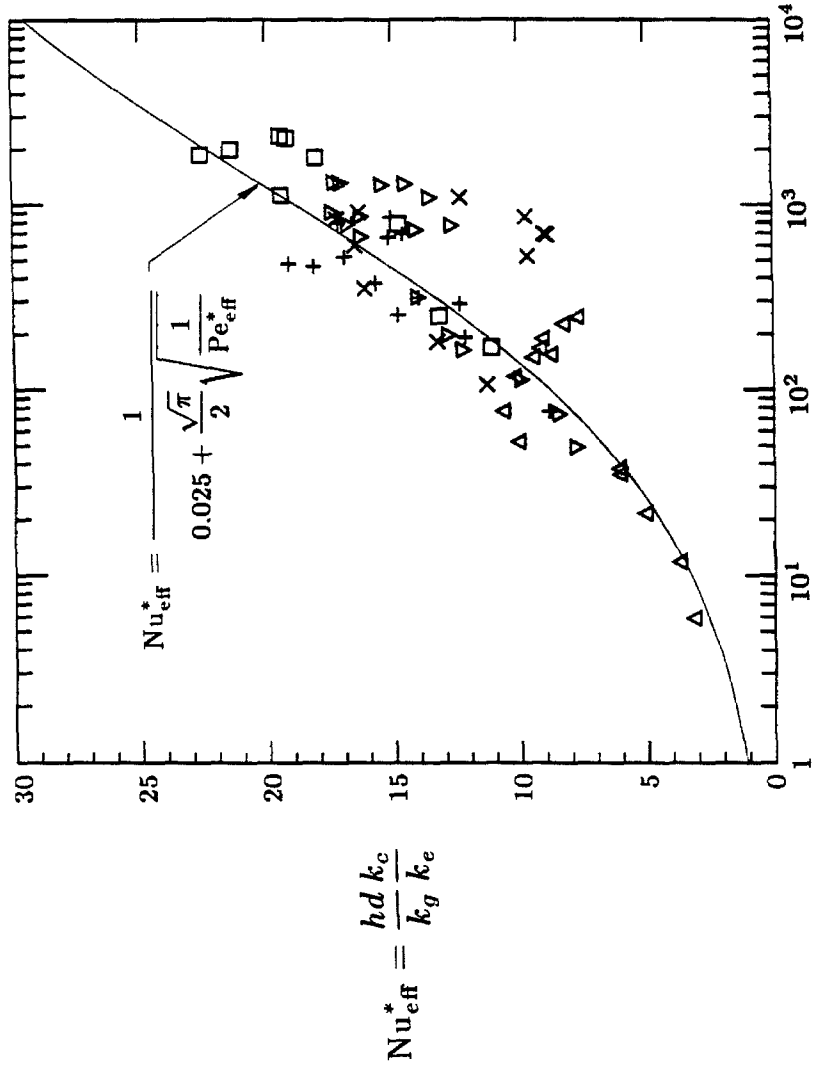

$$\mathrm{Pe}^*_{\mathrm{eff}} = \frac{UL}{\alpha_e}\left(\frac{d}{L}\right)^2\left(\frac{k_e}{k_g}\right)$$

Figure 5.6. The effective Nusselt number, $\mathrm{Nu}^*_{\mathrm{eff}}$, against the effective Peclet number, $\mathrm{Pe}^*_{\mathrm{eff}}$. The curve is from equation (5.7). □, 3.04 mm glass beads; +, 1.26 mm glass beads; △, 0.50 mm glass beads; ×, 3.15 mm polystyrene beads; ▽, 2.22 mm mustard seeds.

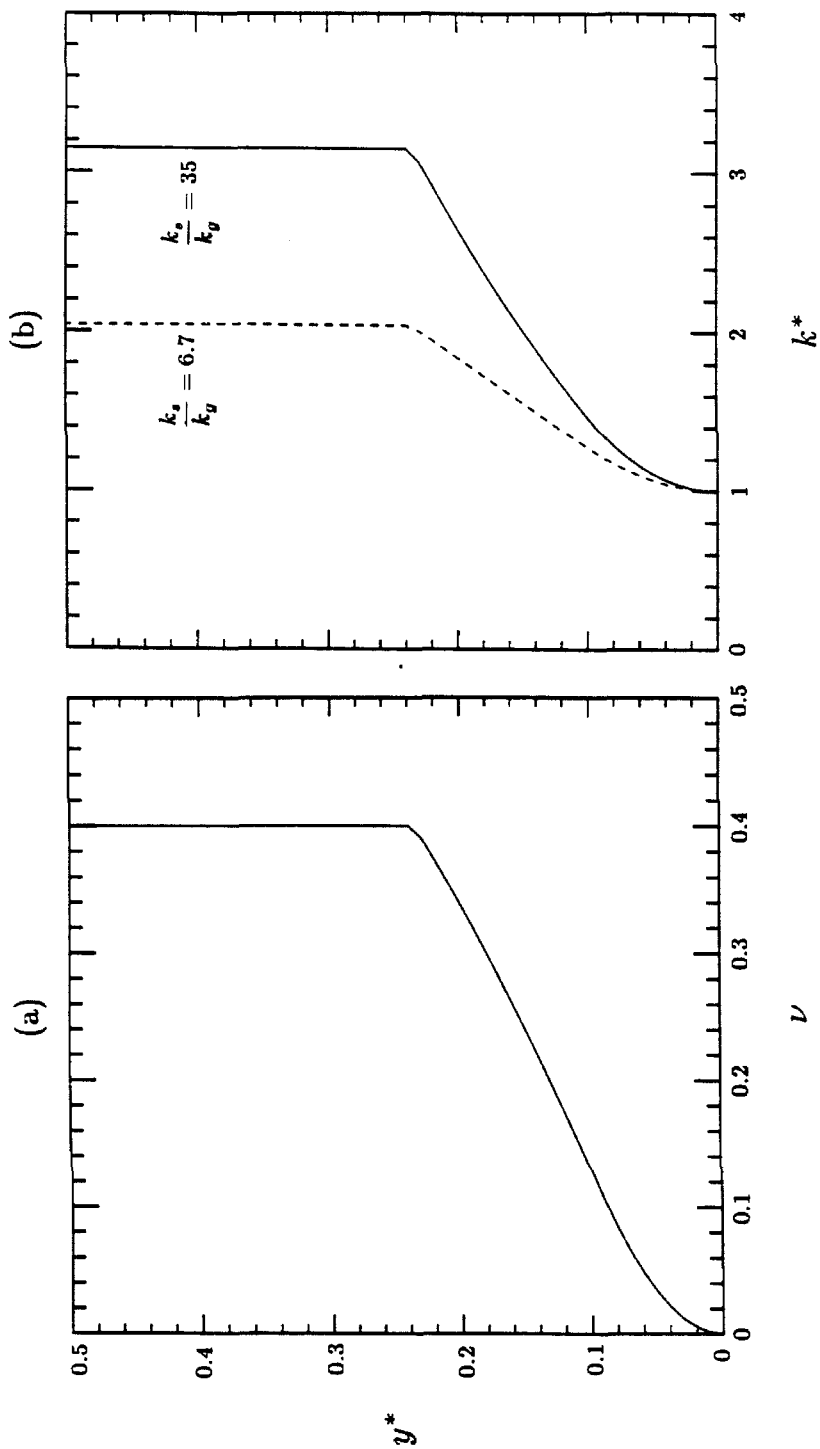

Figure 6.1. The profiles of (a) the solid fraction and (b) the nondimensionalized thermal conductivity against the nondimensionalized distance from the flat plate for the case of $\nu_m = 0.4$.

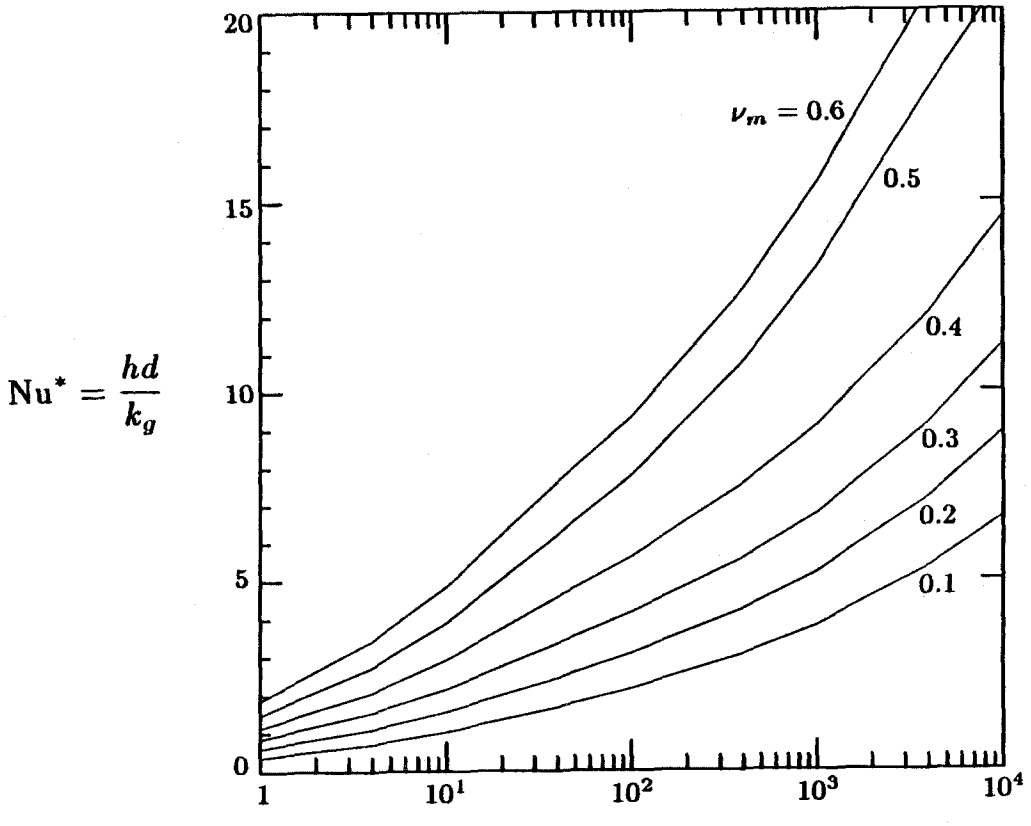

Figure 6.2. The results from the numerical analysis: The modified Nusselt number, Nu^*, against the Peclet number, Pe^{**}, with the variation of the mean solid fraction, ν_m; $k_s/k_g = 35$.

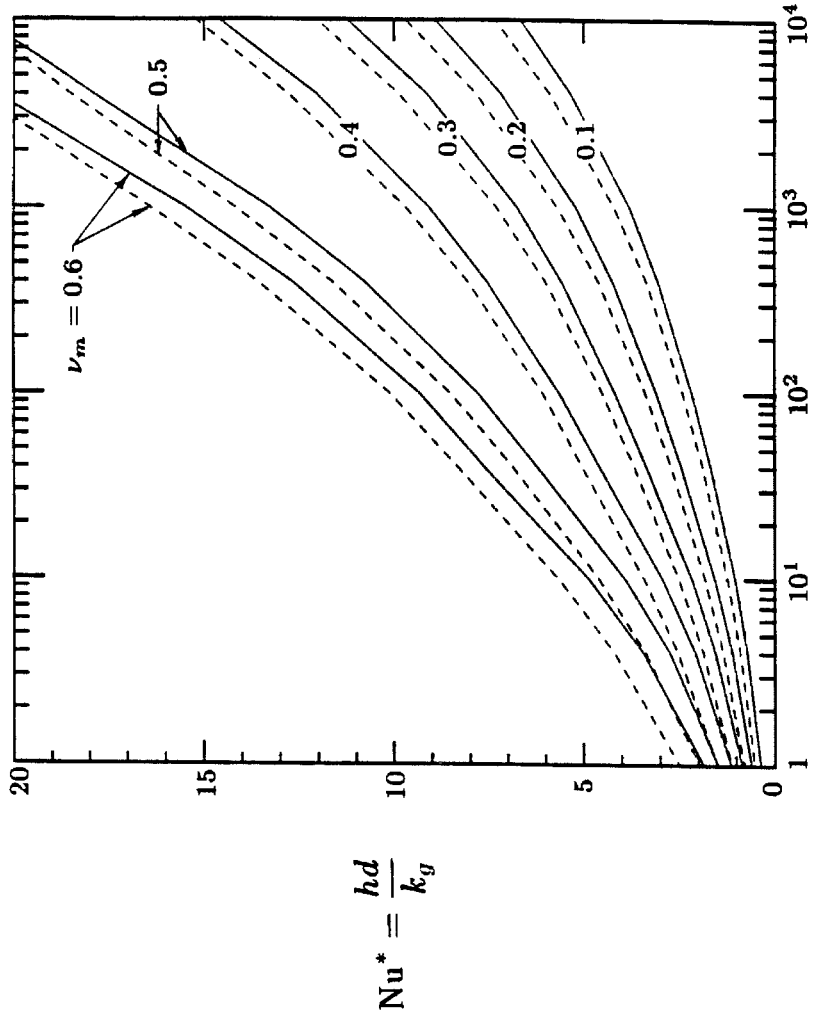

Figure 6.3. Comparison with the constant wall heat flux boundary condition for the case of $k_s/k_g = 35$: Solid line, the constant wall temperature boundary condition; dotted line, the constant wall heat flux boundary condition.

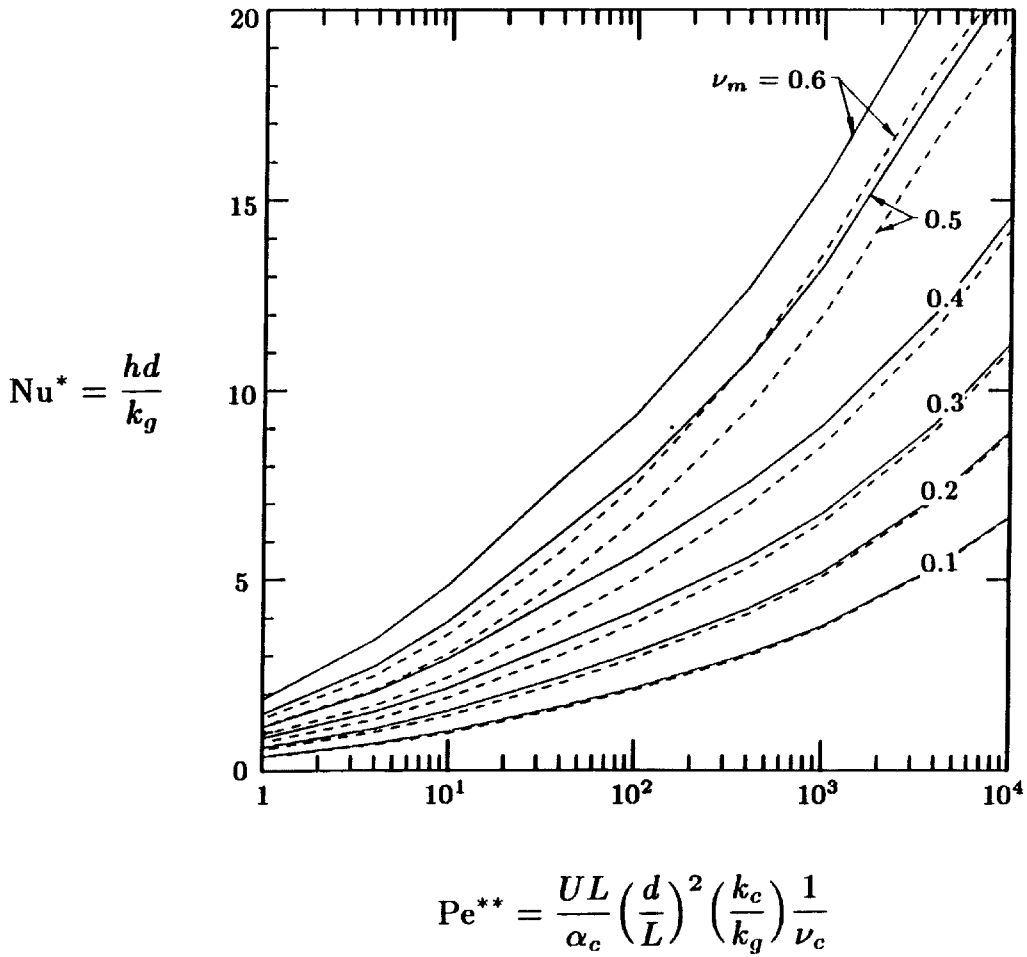

Figure 6.4. The effect of k_s/k_g, the ratio of the thermal conductivity of solid particle to that of gas phase: Solid line, $k_s/k_g = 35$; dotted line, $k_s/k_g = 6.7$.

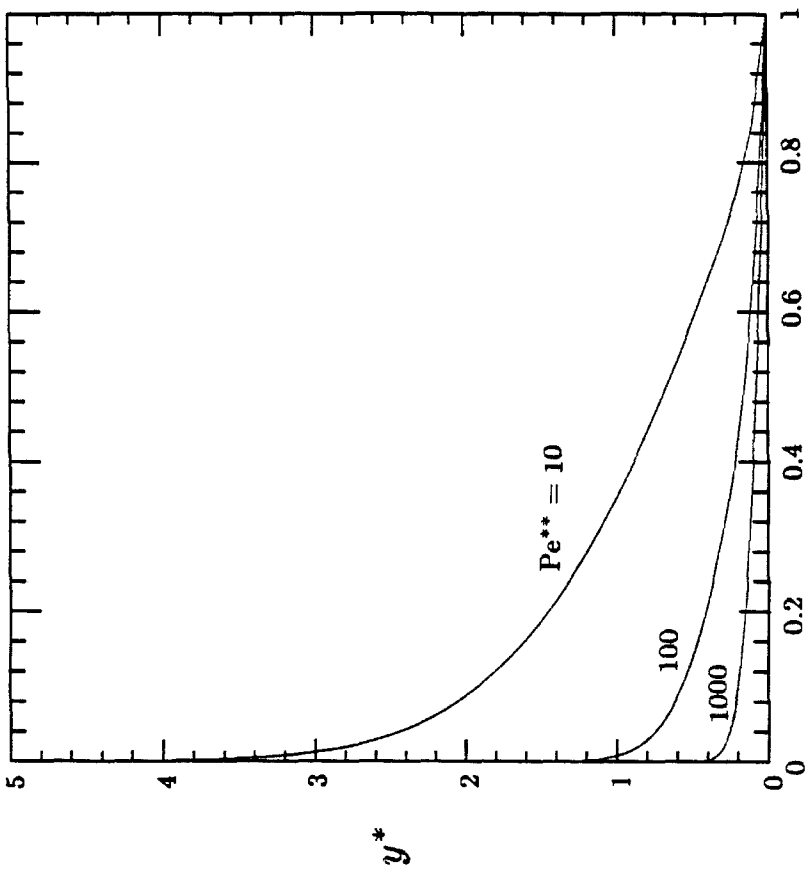

Figure 6.5. The profile of the nondimensionalized temperature, Θ^*, at the trailing edge against the nondimensionalized distance from the flat plate, y^*, with the variation of the Peclet number, Pe^{**}; $\nu_m = 0.4$.

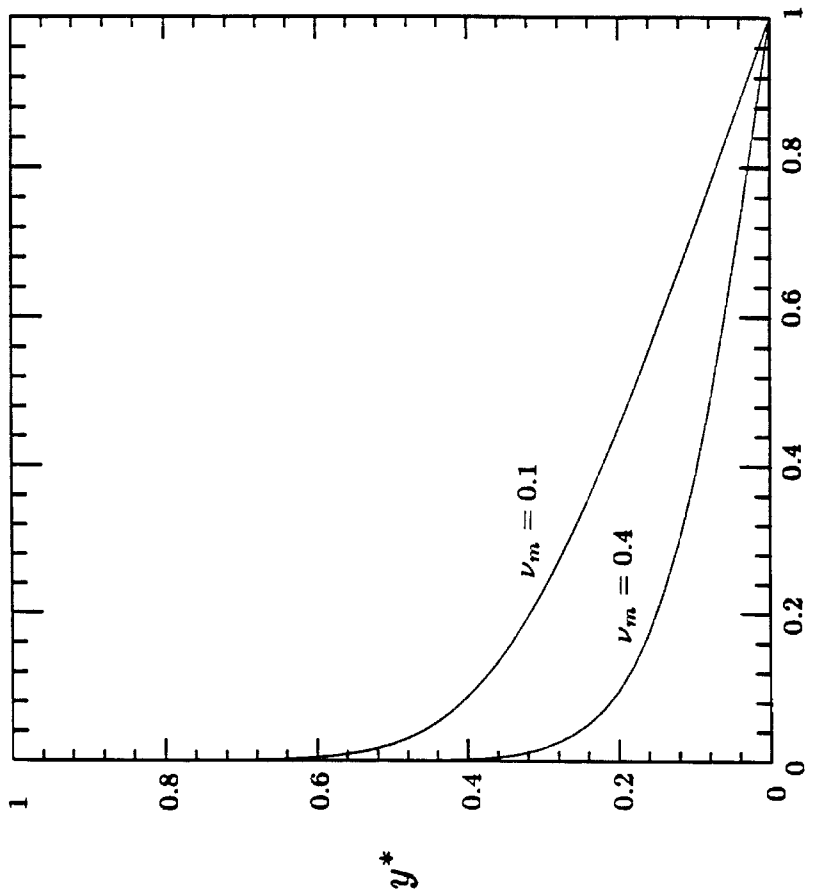

Figure 6.6. The profile of the nondimensionalized temperature, Θ^*, at the trailing edge against the nondimensionalized distance from the flat plate, y^*, with the variation of the mean solid fraction, ν_m; $\mathrm{Pe}^{**} = 1000$.

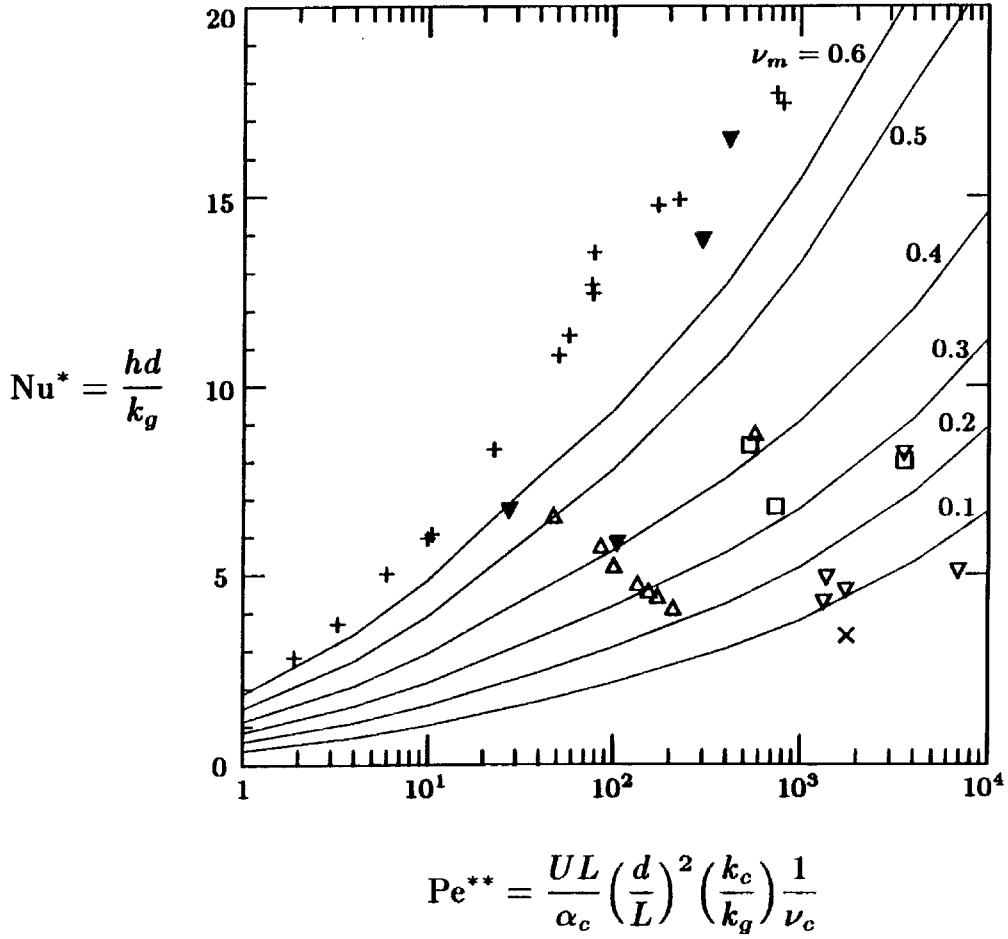

Figure 6.7. Comparison of the numerical results for $k_s/k_g = 35$ with the experimental data for glass beads. $\times$, $\nu_m < 0.15$; $\triangledown$, $0.15 < \nu_m < 0.25$; $\square$, $0.25 < \nu_m < 0.35$; $\triangle$, $0.35 < \nu_m < 0.45$; $\blacktriangledown$, $0.45 < \nu_m < 0.55$; $+$, $0.55 < \nu_m$.

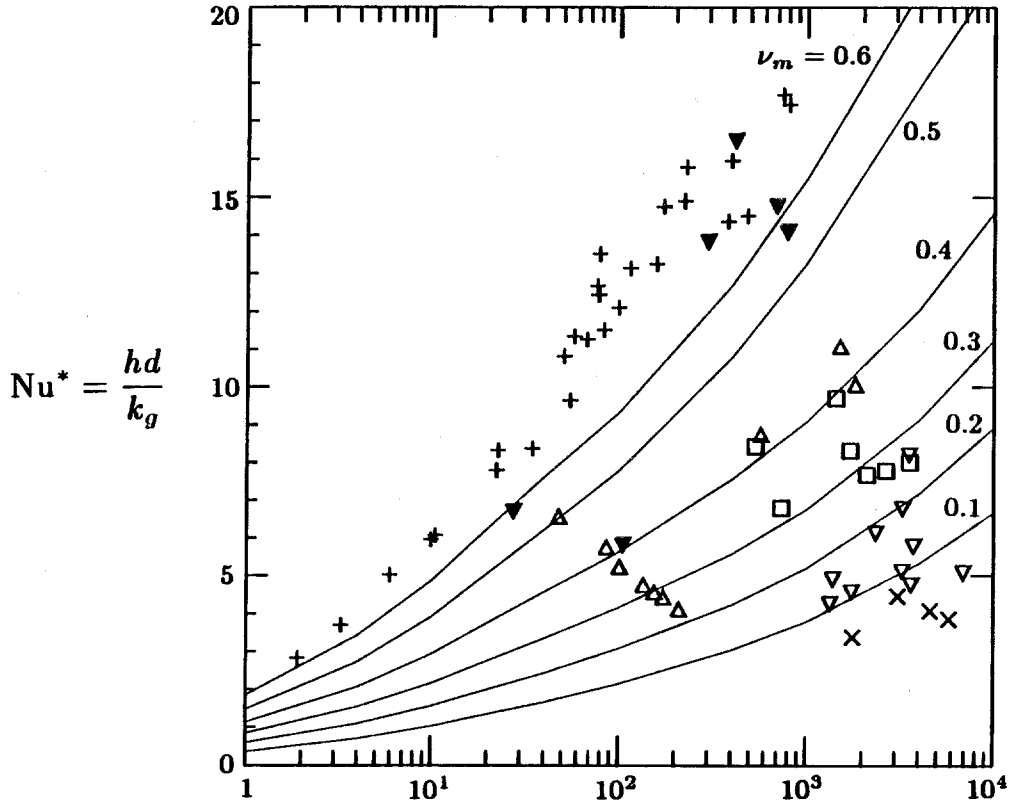

Figure 6.8. Comparison of the numerical results for $k_s/k_g = 35$ with the experimental data for glass beads, polystyrene beads, and mustard seeds. $\times$, $\nu_m < 0.15$; $\triangledown$, $0.15 < \nu_m < 0.25$; $\square$, $0.25 < \nu_m < 0.35$; $\triangle$, $0.35 < \nu_m < 0.45$; $\blacktriangledown$, $0.45 < \nu_m < 0.55$; $+$, $0.55 < \nu_m$.

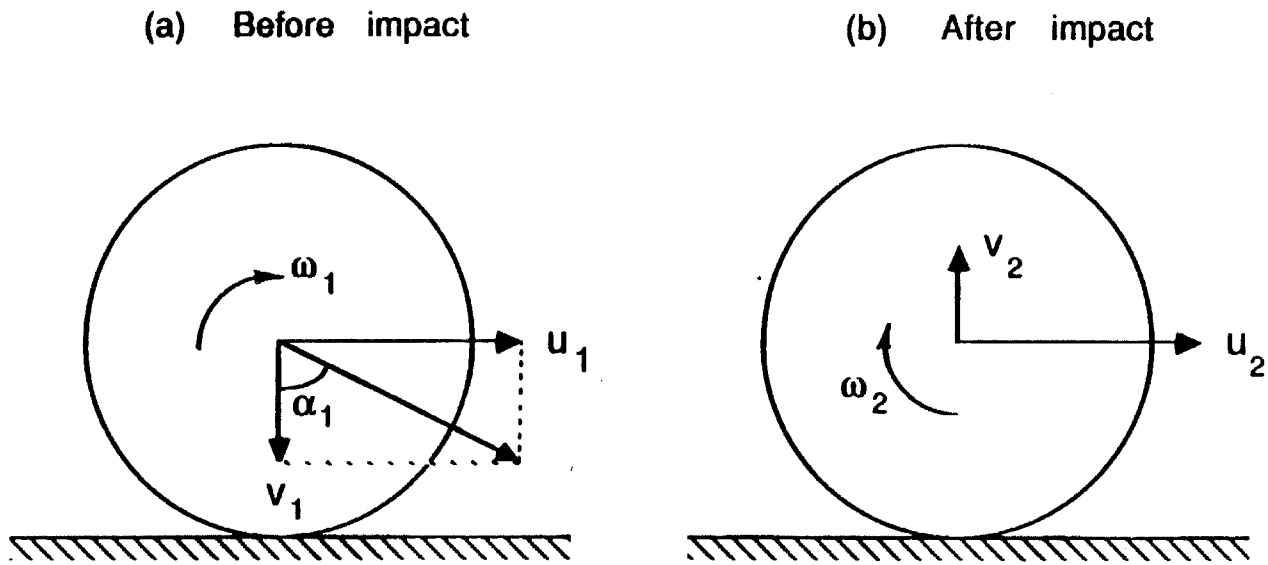

Figure A.1 Diagram of the oblique impact of an inelastic sphere; (a) before impact and (b) after impact.